

# Perturbative aspects of the electroweak phase transition with a complex singlet and implications for gravitational wave predictions

---

Thomas Biekötter,<sup>a</sup> Andrii Dashko,<sup>b,c</sup> Maximilian Löschner,<sup>b</sup> Georg Weiglein<sup>b,d</sup>

<sup>a</sup>*Instituto de Física Teórica UAM/CSIC,  
Calle Nicolás Cabrera 13-15, Cantoblanco, 28049, Madrid, Spain*

<sup>b</sup>*Deutsches Elektronen-Synchrotron DESY,  
Notkestr. 85, 22607 Hamburg, Germany*

<sup>c</sup>*Departamento de Física Teórica y del Cosmos,  
Universidad de Granada, E-18071 Granada, Spain*

<sup>d</sup>*II. Institut für Theoretische Physik,  
Universität Hamburg, Luruper Chaussee 149, 22761 Hamburg, Germany*  
E-mail: [thomas.biekoetter@desy.de](mailto:thomas.biekoetter@desy.de), [andrii.dashko@desy.de](mailto:andrii.dashko@desy.de),  
[maximilian.loeschner@desy.de](mailto:maximilian.loeschner@desy.de), [georg.weiglein@desy.de](mailto:georg.weiglein@desy.de)

**ABSTRACT:** We present a detailed analysis of strong first-order electroweak phase transitions within the extension of the Standard Model by a complex scalar singlet (cxSM). Focusing on the impact of renormalization scale and gauge dependence, we systematically compare commonly used perturbative frameworks for predicting thermodynamic observables that characterize the phase transition and the associated gravitational-wave (GW) spectrum. These include both the four-dimensional (4D) formalism and the dimensionally reduced three-dimensional effective field theory (3D EFT) approach in different renormalization schemes. Within the 3D EFT, we compute the effective potential up to two-loop order in a general  $R_\xi$  gauge, and demonstrate that applying the  $\hbar$ -expansion yields gauge-independent results in excellent agreement with those obtained from a direct minimization of the loop-corrected potential. In contrast, large discrepancies between the two methods persist in the 4D approaches. We find that, across most of the parameter space, the 3D EFT approach provides the most robust predictions for phase-transition parameters and GW spectra, reducing theoretical uncertainties in the GW peak amplitude by more than an order of magnitude compared to the 4D calculations. We point out, however, that the 3D EFT approach is subject to an additional theory uncertainty from truncating the EFT at finite operator dimension and show that higher-dimensional operators within the 3D EFT approach can substantially modify the predicted transition strength and GW signals. This indicates a potential breakdown of the high-temperature expansion precisely in the region with the lowest transition temperatures, where the strongest GW signals are expected and the detection prospects with LISA are most promising.

---

## Contents

<b>1</b>	<b>Introduction</b>	<b>1</b>
<b>2</b>	<b>The model: cxSM</b>	<b>5</b>
<b>3</b>	<b>Effective action and effective potential</b>	<b>8</b>
3.1	Gauge dependence	10
3.2	Renormalization scale dependence	13
3.3	Temperature corrections	14
3.4	High-temperature EFT	16
<b>4</b>	<b>Thermodynamics of the First Order Phase Transition</b>	<b>19</b>
4.1	Critical temperature and latent heat	19
4.1.1	Scale dependence	21
4.1.2	Gauge dependence	26
4.2	Nucleation thermodynamics	32
<b>5</b>	<b>Gravitational wave signals</b>	<b>37</b>
5.1	Spectral density	38
5.2	Peak signal strengths in the $(m_s, \lambda_{hs})$ -plane	41
5.3	LISA SNR	45
<b>6</b>	<b>Impact of higher-dimensional operators within the 3D approach</b>	<b>47</b>
<b>7</b>	<b>Summary and conclusions</b>	<b>49</b>
<b>A</b>	<b>Lagrange parameter input scheme and renormalization</b>	<b>52</b>
A.1	Input parameters	52
A.2	$\beta$ -functions for the cxSM	57
<b>B</b>	<b>Mass eigenstates in <math>R_\xi</math> and Fermi gauges</b>	<b>58</b>

---

## 1 Introduction

The possibility of a First Order Electroweak Phase Transition (FOEWPT) in the early universe has intrigued physicists for decades, as it might play a fundamental role in solving pressing open issues, such as providing an explanation for the origin of the observed baryon asymmetry of the universe (BAU) [1]. Recently, with the first direct detection of gravitational waves (GW) by the LIGO and VIRGO collaborations in 2015 [2], the interest in a

cosmological FOEWPT has further increased since it produces a primordial GW background that might be detectable at current and future (space-based) GW experiments [3–5].

Moreover, a cosmological phase transition can serve, for instance, as a mechanism to generate cosmological topological defects (e.g. domain walls) [6, 7], primordial black holes [8, 9] that potentially contribute to the observed dark-matter relic abundance (see Refs. [10–12] for recent studies), cosmic magnetic fields [13–15] and for the production of heavy particles [16, 17].

In the Standard Model (SM), with the mass of the detected Higgs boson measured at about 125 GeV [18, 19], electroweak (EW) symmetry breaking is predicted to proceed via a smooth crossover instead of a strong FOEWPT (SFOEWPT) [20]. As a consequence, the presence of a SFOEWPT would be a clear indication of physics beyond the Standard Model (BSM). A SFOEWPT can occur even in simple extensions of the SM. For instance, models with additional scalar singlets [21–23], SU(2) doublets [24–29] and/or triplets [30, 31], effective theories incorporating higher dimensional operators [32–34], classically conformal models [35, 36], or models with extra dimensions [37] can all exhibit a SFOEWPT. As mentioned above, a sufficiently strong FOEWPT can be probed by future space-based GW observatories. The observation of a GW signal would be very helpful in this context to pinpoint the underlying scalar sector responsible for the FOEWPT.

A reliable and precise way to study phase transitions is via non-perturbative methods and lattice field theory computations. However, due to their high computational cost, it is not feasible to apply such methods in scans over large parameter spaces of BSM theories with several free parameters that can have an impact on the transition. This necessitates the development of reliable perturbative methods for detailed studies of phase transition dynamics and their phenomenological consequences within the allowed regions of the parameter space of the considered model. A variety of perturbative methods for this purpose have been developed and applied in the literature. They can be divided into two main approaches:

The traditional four-dimensional ( $4D$ ) approach relies on the inclusion of temperature and quantum corrections to the effective potential in the UV theory, typically incorporating thermal resummation techniques such as daisy resummation to improve the infrared behavior (see e.g. Ref. [38] for a review). The simplest and most-often applied resummation prescriptions are the Arnold–Espinosa resummation approach [39], where only the Matsubara zero modes are resummed, and the Parwani resummation approach [40], where masses of all bosonic modes receive thermal corrections. An alternative thermal resummation prescription called “partial dressing” or “tadpole resummation” has been developed, which systematically accounts for daisy and superdaisy diagrams by computing thermal masses from the gap equation and inserting them into the first derivative of the effective potential with respect to the fields [41–44]. Moreover, a method for constructing a resummed effective potential without resorting to the high-temperature expansion has recently been proposed [45], based on the separation of contributions from different scales. There are also recent efforts to reduce the renormalization scale dependence by reorganizing the perturbation theory, employing the so-called Optimized Perturbation Theory [46].

Irrespective of the specific thermal resummation prescription, the main advantage of the

4D approach is that the form of the effective potential at one-loop level is relatively simple to implement, while capturing the leading thermal corrections and providing a qualitatively correct picture of the phase transitions in many extensions of the SM. Recent studies using the 4D approach have, for instance, been carried out for the singlet-extended SM [47–54], the Two Higgs doublet model [26–28] and the triplet-extended SM [55], taking into account current experimental constraints. In some studies also two-loop contributions have been considered in the 4D approach [39, 43, 56–58]. A key drawback of the 4D approach is that it is often affected by the poor behavior of the perturbative expansion at finite temperature, leading to sizable renormalization scale and residual gauge dependencies in predictions for physical observables characterizing the phase transitions. In addition, it suffers from infrared divergences and an unsystematic treatment of thermal fluctuations in the evaluation of transition rates [59, 60]. This leads to large theoretical uncertainties in the predictions for these parameters and quantities that are derived from them, such as GW signals produced during the transitions [61–63].

A more refined alternative to the traditional 4D approaches is the dimensionally reduced three-dimensional (3D) approach [64, 65], which systematically integrates out heavy modes to obtain a low-energy effective field theory (EFT) in three spatial dimensions that captures the relevant infrared dynamics of the phase transition. This method is well-defined in the high-temperature limit and provides more accurate predictions compared to the 4D approach for the case in which the temperature of the phase transition is of the order or larger than the masses of the particles contained in the dimensionally reduced EFT. Since the EFT only contains bosonic degrees of freedom, it also facilitates a more direct comparison with lattice simulations [66–68] than the 4D approach. In perturbation theory, the 3D approach, which exploits the separation of thermal scales, allows the inclusion of thermal next-to-leading order (NLO) two-loop contributions in a simpler and more systematic way [69]. A drawback of the 3D approach compared to the traditional 4D approach is that one has to perform a non-trivial matching procedure between the underlying UV theory and the EFT describing the infrared dynamics. In particular, this matching has to be derived not only in a model-dependent way, but it also depends on the specific realization of the particle spectrum within a model, and thus in general has to be carried out differently for different choices of the free parameters of the model. This makes the application of the 3D approach more involved in the context of BSM theories, whereas the 4D approach can be applied with less additional effort in comparison to the case of the SM. Despite these difficulties, there has been significant development in recent years regarding tools that can be used to construct 3D EFTs in an automated way for various classes of BSM theories. This development has led to the public computer program DRalgo [70] that can be used to perform the matching between the UV theory and the high- $T$  EFT in order to construct a dimensionally reduced, high-temperature EFT. This can be applied to generic models in which an appropriate hierarchy of scales can be exploited. DRalgo provides two-loop thermal corrections to scalar and Debye masses as well as one-loop thermal corrections to couplings. Dimensional reduction has nowadays become a widely used tool for the study of the EW phase transition in scalar extensions of the SM where the high-temperature expansion is applicable, see for instance Refs. [31, 71, 72] for recent analyses.

Another problem occurring both in the  $4D$  and the  $3D$  approaches is the presence of residual gauge dependence in predictions for physical observables related to the phase transition. A proposed solution to this issue is the so-called  $\hbar$ -expansion [73], which systematically expands physical quantities in powers of a loop-counting parameter  $\hbar$ . This ensures that one obtains gauge-independent results for physical observables order by order in perturbation theory. At the one-loop level in the  $4D$  approach, applying the  $\hbar$ -expansion removes gauge dependence, but leads to results that, in many models, are not sufficiently precise, deviating substantially from more accurate predictions [73]. Additionally, the  $\hbar$ -expansion must be implemented consistently with the thermal resummation procedure to obtain a gauge-independent formulation at finite temperature [60, 74].

In this work, we point out that in the  $4D$  approach, the  $\hbar$ -expansion is difficult to pursue up to a sufficiently high order that yields the desired level of accuracy. In the  $3D$  approach, we show that it is possible to achieve a gauge-independent formulation with higher numerical precision for the predicted quantities than in the  $4D$  approach. By systematically including thermal effects via dimensional reduction, we obtain results for physical observables and predictions for GW signals that are both gauge-independent and numerically accurate. We compare gauge-independent results obtained via  $\hbar$ -expansion for the thermodynamic observables with the gauge-dependent ones, obtained by the direct minimization of the effective potential. For the latter, we evaluate the effective potential at the two-loop order in  $R_\xi$ -gauge, cross-checking the two-loop potential in the Landau gauge, which is implemented in `DRalgo`. Moreover, we compare the residual gauge dependence in  $R_\xi$ - and Fermi gauges at the one-loop level.

We furthermore compare the uncertainty in the predictions of observables describing the FOEWPT arising from the gauge dependence with the uncertainties related to the variation of renormalization and matching scales in both  $4D$  and  $3D$  approaches. For instance, we show how various matching orders of dimensional reduction affect the matching scale uncertainty.

Specifically, we investigate the EW phase transition in the SM extended by a complex gauge singlet scalar field (cxSM). The cxSM provides an interesting framework in view of the fact that no clear sign of new physics has been detected at the LHC up to now, as the cxSM can accommodate a SFOEWPT without predicting detectable traces at current and future runs of the LHC [75]. Consequently, the possibility of probing a SFOEWPT in the cxSM via GWs becomes particularly important. It is therefore crucial to make precise and accurate predictions for the parameters characterizing the transition and to ensure theoretical control over GW predictions. The model has been studied previously using the  $4D$  approach in Refs. [47, 50, 53, 76] and the  $3D$  approach in Ref. [77]. However, a comprehensive analysis of the parameter space facilitating a SFOEWPT and of the prospects for future GW detection comparing different perturbative methods has not yet been carried out. In this paper, we study thermodynamic observables of FOEWPTs and determine the parameter space regions

that can potentially be probed with the LISA GW observatory<sup>1</sup>, focusing especially on the theoretical uncertainties in the predictions and the impact of residual gauge dependence and renormalization- and matching-scale dependence. We compare and contrast the  $4D$  and the  $3D$  approaches, assessing their respective limitations in capturing the dynamics of the transition. Moreover, we test the validity of the  $3D$  approach — which relies on the high-temperature expansion — by including higher-dimensional operators in the EFT Lagrangian.

The outline of the paper is as follows: in Section 2 we introduce the cxSM and specify our notation. In Section 3 we discuss the construction of the finite-temperature effective potential in  $4D$  and  $3D$ , focusing in particular on the gauge dependence and scale dependence. In Section 4 we discuss the related theoretical uncertainties on thermodynamic parameters. Section 5 is devoted to the predictions for the stochastic GW backgrounds produced during a SFOEWPT, and we determine the parameter space that can potentially be probed with future GW experiments. In Section 6, we analyze the range of validity for the  $3D$  approach by studying the impact of higher-dimensional operators of the EFT. We summarize our results and conclude in Section 7. In addition, the relations between physical input and Lagrange parameters in different schemes are discussed in Appendix A; mass eigenstates of the cxSM in  $R_\xi$  and Fermi gauges are presented in Appendix B.

## 2 The model: cxSM

The model used for studying the phase transition dynamics in this work is the Standard Model with an additional complex scalar singlet (cxSM). The cxSM is one of the simplest SM extensions that can realize a (strong) FOEWPT. This leads to a variety of phenomenologically interesting signatures, such as GW signals produced in the early universe which would potentially be accessible at near-future space-based GW observatories. Moreover, the cxSM can include a stable neutral particle that could serve as a viable dark matter candidate. However, we will not discuss this feature in our analysis below.

The scalar sector of the cxSM consists of the doublet  $\Phi$  with hypercharge  $Y = 1$  and a complex gauge singlet  $S$ ,

$$\Phi = \begin{pmatrix} G^+ \\ \frac{1}{\sqrt{2}}(\phi_h + h + iG^0) \end{pmatrix}, \quad S = \frac{1}{\sqrt{2}}(\phi_s + s + iA), \quad (2.1)$$

where we expanded the real part of the neutral component of  $\Phi$  and the real part of the singlet field  $S$  around the background field configurations  $\phi_h$  and  $\phi_s$ , respectively. The Lagrangian density of the model in Minkowski space can be written as

$$\mathcal{L}_{\text{cxSM}} = \mathcal{L}_{\text{YM}} + \mathcal{L}_{\text{F}} + \mathcal{L}_{\Phi S}, \quad (2.2)$$

---

<sup>1</sup>The question whether a predicted GW signal is detectable or not at a particular experiment can ultimately only be answered if the theoretical uncertainties from the hydrodynamic modeling of GW production during the FOEWPT and experimental uncertainties, e.g. from unknown (astrophysical or cosmological) GW foregrounds are taken into account. These considerations lie beyond the scope of this work, where we focus on the theoretical uncertainties in the perturbative description of the EW phase transition.

where  $\mathcal{L}_{\text{YM}}$ ,  $\mathcal{L}_{\text{F}}$  and  $\mathcal{L}_{\Phi S}$  are the Yang-Mills, fermionic and scalar parts of the Lagrangian, respectively. Since only the doublet  $\Phi$  is charged under the  $\text{SU}(2)_L \times \text{U}(1)_Y$  gauge groups, the gauge and fermionic sectors of the cxSM are identical to the SM. The electroweak part of the Yang-Mills Lagrangian is given by

$$\mathcal{L}_{\text{YM}} \supset -\frac{1}{4} \left( \partial_\mu W_\nu^a - \partial_\nu W_\mu^a + g\varepsilon^{abc} W_\mu^b W_\nu^c \right)^2 - \frac{1}{4} (\partial_\mu B_\nu - \partial_\nu B_\mu)^2, \quad (2.3)$$

where  $W_\mu^a$  and  $B_\mu$  are the corresponding gauge fields,  $\tau^a$  the generators of the  $\text{SU}(2)_L$  gauge group, and  $g$  is the  $\text{SU}(2)_L$  gauge coupling. The fermionic part is identical to the SM (for instance, see [78]); however, since only the top quark is relevant for the phase transition dynamics due to its large mass, we only take into account its Yukawa coupling to the Higgs doublet,

$$\mathcal{L}_{\text{F}} \supset -y_t \bar{Q}_L^3 (i\sigma_2 \Phi^*) t_R + \text{h.c.}, \quad (2.4)$$

where  $y_t$  denotes the Yukawa coupling of the top quark,  $Q_L^3 = (t_L, b_L)^T$  is the third generation quark doublet, and  $t_R$  is the right-handed top quark singlet state. In this paper, we focus on a specific subclass of the cxSM in which a global  $\text{U}(1)$  symmetry is imposed on the gauge singlet  $S$  [79]. Then, the scalar part of the Lagrangian is given by

$$\mathcal{L}_{\Phi S} = D_\mu \Phi^\dagger D^\mu \Phi - \mu_h^2 \Phi^\dagger \Phi - \lambda_h (\Phi^\dagger \Phi)^2 + |\partial^\mu S|^2 - \frac{1}{2} \mu_s^2 |S|^2 - \frac{1}{4} \lambda_s |S|^4 - \frac{1}{2} \lambda_{hs} |S|^2 \Phi^\dagger \Phi, \quad (2.5)$$

with the covariant derivative

$$D_\mu = \partial_\mu - \frac{i}{2} g \tau^a W_\mu^a + i \frac{Y}{2} g' B_\mu, \quad (2.6)$$

and  $g'$  and  $g$  are the couplings of the  $\text{U}(1)_Y$  and  $\text{SU}(2)_L$  gauge groups, respectively. If  $S$  does not have a vev, the global  $\text{U}(1)$  symmetry is conserved.

The tree-level scalar potential as a function of the background fields  $\phi_h$  and  $\phi_s$  reads

$$V_0(\phi_h, \phi_s) = \frac{\mu_h^2}{2} \phi_h^2 + \frac{\mu_s^2}{4} \phi_s^2 + \frac{\lambda_h}{4} \phi_h^4 + \frac{\lambda_{hs}}{8} \phi_h^2 \phi_s^2 + \frac{\lambda_s}{16} \phi_s^4. \quad (2.7)$$

This also serves as the lowest-order version of the effective potential at zero temperature. In Section 3, we will describe how the effective potential is modified by zero-temperature and thermal loop corrections, leading to a temperature dependence of the vacuum structure. It is known that, unlike in the SM, as a consequence of the additional singlet the phase evolution of the cxSM can exhibit a SFOEWPT in certain regions of parameter space. In our study, we ensure that the tree-level potential is bounded from below by choosing  $\lambda_h > 0$ ,  $\lambda_s > 0$  and  $\lambda_{hs} > -2\sqrt{\lambda_h \lambda_s}$ . In order to accommodate a SFOEWPT, we concentrate on positive values for the portal coupling,  $\lambda_{hs} > 0$  [47]. Moreover, we demand that only the Higgs field  $h$  has a non-zero vacuum expectation value at zero temperature:

$$v_h(T=0) = v_{\text{EW}} \approx 246.2 \text{ GeV}, \quad v_s(T=0) = 0. \quad (2.8)$$

Allowing for a non-zero singlet vev  $\phi_s^{\text{min}} = v_s(T)$  at finite temperature, the cxSM exhibits a FOEWPT of the form  $(0, v_s(T)) \rightarrow (v_h(T), 0)$ , where  $\phi_h^{\text{min}} = v_h(T)$  is the vev of the Higgs field (visualized in Fig. 1).<sup>2</sup>

<sup>2</sup>We find that direct minimization of the loop-improved effective potential can result in a small unphysical non-zero Higgs vev in the high-temperature phase. This is further discussed in Section 4.

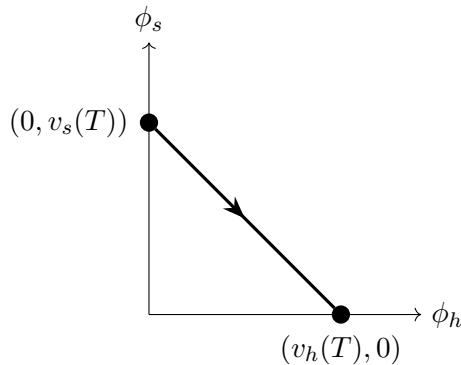


**Figure 1:** The pattern of a possible strong FOEWPT in the cxSM model explored in this work. The arrow points in the direction of decreasing temperature.

In total, the cxSM has six scalar degrees of freedom: a CP-even scalar  $h$  from the real part of the neutral component of  $\Phi$  that can be identified with the detected Higgs boson at 125 GeV, three would-be Goldstone bosons  $G_{0,\pm}$  from the CP-odd and the charged components of  $\Phi$ , and two scalar degrees of freedom  $s$  and  $A$  from the real and imaginary parts of the singlet field  $S$ , respectively. As indicated above, we consider the case where at zero temperature only the Higgs field  $h$  has a vev, whereas the vev of the singlet field vanishes. At finite temperature we study FOEWPTs from a U(1)-symmetry breaking phase in which the singlet field has a non-zero vev  $v_s$ , into an EW symmetry breaking phase with a non-zero Higgs vev  $v_h$ . We therefore consider the two background fields  $\phi_h$  and  $\phi_s$ : if both  $\phi_h \neq 0$  and  $\phi_s \neq 0$ , the two CP-even fields  $h$  and  $s$  mix with each other, whereas the would-be Goldstone fields  $G_0$  and  $G^\pm$  and the other component of the singlet field  $A$  are mass eigenstates. The field-dependent mass matrix of the CP-even states  $h$  and  $s$  is given by

$$M_{hs}^2 = \begin{pmatrix} \mu_h^2 + 3\lambda_h\phi_h^2 + \frac{\lambda_{hs}\phi_s^2}{4} & \frac{\lambda_{hs}\phi_h\phi_s}{2} \\ \frac{\lambda_{hs}\phi_h\phi_s}{2} & \frac{\mu_s^2}{2} + \frac{3\lambda_s\phi_s^2}{4} + \frac{\lambda_{hs}\phi_h^2}{4} \end{pmatrix}. \quad (2.9)$$

The field-dependent mass of  $A$  is given by

$$M_A^2 = \frac{\mu_s^2}{2} + \frac{\lambda_s\phi_s^2}{4} + \frac{\lambda_{hs}\phi_h^2}{4}, \quad (2.10)$$

and for the would-be Goldstone bosons in the Landau gauge, we have

$$M_{G_{0,\pm}}^2 = \mu_h^2 + \lambda_h\phi_h^2 + \frac{\lambda_{hs}\phi_s^2}{4}. \quad (2.11)$$

Here, it should be noted that the Goldstone boson masses also receive contributions from the gauge-fixing, which we do not display here. We discuss the mass eigenstates of the would-be Goldstone and gauge bosons in different gauges in detail in Appendix B.

The cxSM has three free parameters in addition to the SM ones. We choose to treat the singlet mass  $m_s$ , the singlet quartic coupling  $\lambda_s$  and the portal coupling  $\lambda_{hs}$  as free parameters. For the SM sector, we use the Higgs boson mass  $m_h$ , the top quark mass  $m_t$ ,

the gauge boson masses  $m_W$  and  $m_Z$ , and the Fermi constant  $G_F$  as input parameters. Their numerical values are given in Section A.1, where we also show the tree-level relations between those input parameters and the Lagrangian parameters. We note that in our notation, a lowercase  $m_p$  refers to the physical mass of the particle  $p$ , whereas an uppercase  $M_p$  refers to the field-dependent tree-level mass parameter.

The phenomenology of the cxSM at zero temperature differs from the SM by the presence of the degenerate states  $s$  and  $A$ , which are stable due to the unbroken  $U(1)$  symmetry at zero temperature. In principle, they can be dark matter candidates, but dark matter direct detection experiments and searches for the invisible decay of the 125 GeV Higgs boson (which are possible in the cxSM if the decays  $h \rightarrow ss$  and  $h \rightarrow AA$  are kinematically allowed) exclude this possibility except for the  $s$ -channel resonance region with dark matter masses of  $m_s \approx 62.5 \text{ GeV}$  [47, 80] or for heavy masses of  $m_s \gtrsim 2 \text{ TeV}$  [81].<sup>3</sup> In our discussion, focusing on the description of a strong FOEWPT in the early universe, we do not treat the singlet states as possible dark matter candidates. Consequently, we do not limit the discussion to the parameter regions that would be consistent with experimental limits from (among others) direct detection experiments. We thus assume that the states  $s$  and  $A$  are not stable on cosmological timescales, either due to tiny  $\mathbb{Z}_2$ -breaking couplings facilitating the decays of  $s$  and  $A$  into SM particles, or due to the presence of an extended dark sector with particles lighter than  $s$  and  $A$  into which the latter can decay.

In such a situation, and assuming  $m_s > 62.5 \text{ GeV}$  such that the presence of  $s$  and  $A$  does not give rise to exotic or invisible decays of the 125 GeV Higgs boson  $h$ , the cxSM is very challenging to experimentally distinguish from the SM. The possibility of realizing a strong FOEWPT in this model has consequently been called a *nightmare scenario* [84], especially since the modifications of the Higgs sector giving rise to the phase transition would not lead to detectable traces at the LHC [75]. However, in the upcoming decade, the LISA experiment is expected to be launched. LISA is sensitive to GWs in the frequency band that coincides with the peak frequencies of primordial GW backgrounds produced during an EW phase transition. Hence, LISA will offer a new and potentially unique window to test the EW phase transition in the  $U(1)$ -symmetric cxSM. It is therefore vital to provide accurate predictions for the parameters characterizing the transition with a precision that makes it possible to determine the parameter space regions that predict potentially detectable GW signals.

### 3 Effective action and effective potential

For the study of the vacuum structure and possible phase transitions we use the one-particle-irreducible (1PI) effective action formalism [85] which we will briefly describe here. We define the effective action  $\Gamma[\phi]$  as the Legendre transform of the generating functional of connected Green's functions,  $W[J]$ , with respect to the source  $J(x)$  that couples to the

---

<sup>3</sup>The constraints from direct detection experiments can be avoided by considering a softly-broken  $U(1)$ -symmetry in which the state  $A$  acts as pseudo-Nambu-Goldstone dark matter candidate in the presence of a non-zero vev  $v_s$  [82]. However, this version of the cxSM is not able to realize a strong FOEWPT [83].

background field  $\phi(x)$

$$\Gamma[\phi] = W[J] - \int d^4x J(x)\phi(x). \quad (3.1)$$

In this section  $\phi$  represents all the fields within the theory. The effective action as defined in Eq. (3.1) is the generating functional for 1PI correlation functions.

Importantly, the true vacuum of the theory (with  $J = 0$ ) satisfies

$$\frac{\delta\Gamma[\phi(x)]}{\delta\phi(x)} = 0, \quad (3.2)$$

allowing us to determine the vacuum structure by simply extremizing the effective action.  $\Gamma[\phi]$  can be expanded in powers of derivatives of  $\phi(x)$  as

$$\Gamma[\phi] = \int d^4x \left[ -V(\phi) + \frac{1}{2}Z(\phi)(\partial_\mu\phi\partial^\mu\phi) + \dots \right], \quad (3.3)$$

where  $V(\phi)$  is the effective potential and  $Z(\phi)$  is a field renormalization constant. Under the assumption of homogeneity of the background field  $\phi$ , the effective potential becomes a density of the effective action; simply put, the effective potential encodes the quantum corrections to the classical potential (as defined in Eq. (2.7) for the cxSM).

We evaluate the effective potential and the effective action in a perturbative expansion  $V(\phi) = V_0(\phi) + V_1(\phi) + V_2(\phi) + \dots$  within the so-called background field method [86]. The tree-level effective potential  $V_0$  coincides with the classical scalar potential of the theory. The one loop effective potential  $V_1(\phi)$  reads [87]

$$V_1(\phi) = -\frac{i}{2} \sum_{i \in \text{fields}} \eta_i \int_p \log \det iG_i^{-1}(p, \phi), \quad (3.4)$$

where  $G_i^{-1}(p, \phi)$  are the  $\phi$ -dependent inverse propagators of the quantum fields in the theory, and  $p$  denotes their momentum. The normalization factors are  $\eta_i = 1$  for bosons and  $\eta_i = -2$  for fermions and ghosts. This expression can be written as

$$V_1 = \sum_{i \in V, S, f, c} n_i I(M_i^2), \quad (3.5)$$

in which we sum over the index  $i$  labeling the background-field-dependent mass eigenstates  $M_i$  contained in the theory, arising from the determinant of the inverse propagator. The factors  $n_i$  are  $n_i = d - 1$  for gauge fields (V),  $n_i = -4N_c$  for Dirac fermions (f),  $n_i = -2$  for ghosts (c), and  $n_i = 1$  for scalar fields (S);<sup>4</sup> here,  $d$  is the number of space-time dimensions. The loop integrals  $I(M_i^2)$  are divergent in  $d = 4$ , but can be renormalized in the  $\overline{\text{MS}}$ -scheme. Then, the integral takes the form

$$I^{4D}(M_i) = \frac{1}{2} \int_p \log(p^2 + M_i^2) \Big|_{\overline{\text{MS}}} = \frac{1}{64\pi^2} M_i^4 \left( \log \frac{M_i^2}{\mu^2} - c_i \right), \quad (3.6)$$

---

<sup>4</sup>We note that (depending on the gauge) the factors  $n_i$  do not generally correspond to the number of physical degrees of freedom.

where the superscript  $4D$  refers to the four-dimensional approach used here. The constants  $c_i$  are  $c_i = 5/6$  for transverse and longitudinal polarizations of vector bosons and  $c_i = 3/2$  for all other degrees of freedom [86]. In  $d = 4$  dimensions, the  $\overline{\text{MS}}$  renormalized one-loop (bubble) integral  $I^{4D}$  explicitly depends on the renormalization scale  $\mu$ . The one-loop part  $V_1$  of the effective potential expressed in terms of  $I^{4D}$  given in Eq. (3.6) is known as the Coleman-Weinberg potential.

The one-loop effective potential in the dimensionally reduced EFT, in  $d = 3$  Euclidean space, reduces to the same form as in Eq. (3.5), with

$$I^{3D}(M_i) = -\frac{M_i^{3/2}}{12\pi}. \quad (3.7)$$

Accordingly, the effective potential in  $3D$  does not explicitly depend on the renormalization scale at the one-loop level. However, it does show an explicit  $\mu_{3D}$ -dependence starting from two loops [69], see the discussion in Section 3.4. The benefit of evaluating the effective potential in  $3D$  compared to the effective potential in  $4D$  will become apparent when considering temperature corrections to the effective potential in Section 3.3 and the related scale uncertainties.

The higher-loop effective potential requires the evaluation of vacuum diagrams with dressed propagators (*prototype* graphs [86]). For instance, at two-loop order, the effective potential receives contributions both from factorizable figure-8 (double-bubble) diagrams and genuine two-loop irreducible diagrams, as shown in Fig. 2. The resulting two-loop piece of the potential can schematically be written as:

$$V_2 = V_{VVV} + V_{VVS} + V_{VSS} + V_{SSS} + V_{ffV} + V_{ffS} + V_{ccV} + V_{ccS} + V_{VV} + V_{SS} + V_{VS}. \quad (3.8)$$

Here, the terms with three indices represent contributions from genuine two-loop diagrams, whereas the terms with two indices represent contributions from figure-8 diagrams, and the indices ( $V, S, f, c$ ) denote the particle type inserted into the propagators of the diagrams. The explicit form of the two- and three-loop effective potential in terms of master integrals has been computed in  $4D$  in Refs. [88, 89] using the background field method. We follow this method to evaluate the two-loop effective potential in the dimensionally reduced  $3D$  theory in  $R_\xi$ -gauge, see Section 3.4 for details. In three dimensions, the evaluation of the two-loop potential is more straightforward compared to four dimensions since the two-loop integrals evaluate to simple logarithmic expressions.

In the following, we investigate the dependence on a gauge choice and the renormalization scale dependence of the effective potential in more detail. It is worth noting that many of these results can be generalized to the effective action, which plays a crucial role in the study of non-equilibrium thermodynamics.

### 3.1 Gauge dependence

The effective action shown in Eq. (3.1) is defined for a non-zero source term, which violates the Ward-Takahashi identities [90]. As a consequence, the effective action and thus also the effective potential are intrinsically gauge-dependent quantities.

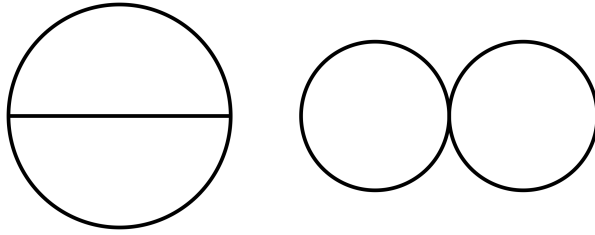


**Figure 2:** Topologies of prototype diagrams with background field dependent propagators entering the effective potential calculation at the two-loop level.

The gauge dependence of the effective potential is governed by the Nielsen identity [91],

$$\xi \frac{\partial}{\partial \xi} V(\phi, \xi) = C(\phi, \xi) \frac{\partial}{\partial \phi} V(\phi, \xi), \quad (3.9)$$

where  $\xi$  represents a set of gauge-fixing parameters. This equation follows from Ward identities with a non-zero background current [90, 91]. The functions  $C(\phi, \xi)$  can be determined order-by-order in perturbation theory independently of  $V$  (see, for instance, Refs. [92, 93]).

The Nielsen identity shows that the effective potential is gauge-independent at its extremal points  $v$ ,

$$\xi \frac{\partial}{\partial \xi} V(v, \xi) = 0. \quad (3.10)$$

The extremizing field value itself, however, is gauge-dependent (which is not a problem, as it is not a physical observable, and occurs as a consequence of the spontaneous breaking of the gauge symmetry),

$$\frac{\partial v}{\partial \xi} = C(v, \xi). \quad (3.11)$$

Away from the extrema, Eq. (3.9) shows that the gauge dependence can be expressed in terms of field redefinitions governed by the functions  $C(\phi, \xi)$ .

Since the values of the effective potential at its stationary points are gauge-independent, the physical observables that depend solely on these values are gauge-independent as well. For instance, the critical temperature  $T_c$ , which is defined as the temperature at which two local minima are degenerate (see Section 4.1 for a detailed discussion), is gauge-independent. Therefore, it follows from Eq. (3.11) that the ratio  $\Delta v_h(T_c)/T_c$ , where  $\Delta v_h(T_c)$  denotes the difference of  $v_h$  between two phases (local minima) at  $T_c$ , used in the context of EW baryogenesis in the baryon number preservation condition  $\Delta v_h(T_c)/T_c > 1$ , is gauge-dependent [73].

Equation (3.9) incorporates contributions to all orders and thus needs careful treatment when truncating a calculation at finite loop-order. Schematically, at one-loop order, we have

$$\xi \frac{\partial}{\partial \xi} V_1 = C_1(\phi, \xi) \frac{\partial}{\partial \phi} V_0, \quad (3.12)$$

where we indicate the respective loop orders by the subscripts. Notice that different extremizing field values  $v$  are relevant for the l.h.s. and r.h.s. of Eq. (3.12). This lies at the heart of the so-called  $\hbar$ -expansion [73, 90] which we will briefly discuss here.

In order to ensure gauge-independence of physical observables, a loop expansion of both the effective potential and its extremizing field is crucial. We write both  $V(\phi)$  and  $v$  as a formal expansion<sup>5</sup> in the loop-counting parameter  $\hbar$ ,

$$V(\phi) = V_0(\phi) + \hbar V_1(\phi) + \hbar^2 V_2(\phi) + \mathcal{O}(\hbar^3), \quad (3.13)$$

$$v = v_0 + \hbar v_1 + \hbar^2 v_2 + \mathcal{O}(\hbar^3). \quad (3.14)$$

Extremizing the potential and collecting contributions in terms of powers of  $\hbar$  result in

$$\begin{aligned} 0 = & \left. \partial_\phi V_0 \right|_{v_0} + \hbar \left[ \partial_\phi V_1 + v_1 \partial_\phi^2 V_0 \right] \Big|_{v_0} \\ & + \hbar^2 \left[ \partial_\phi V_2 + v_2 \partial_\phi^2 V_0 + v_1 \partial_\phi^2 V_1 + \frac{1}{2} v_1^2 \partial_\phi^3 V_0 \right] \Big|_{v_0} + \mathcal{O}(\hbar^3). \end{aligned} \quad (3.15)$$

This defines the tree-level extremum

$$\left. \partial_\phi V_0 \right|_{v_0} = 0, \quad (3.16)$$

the one-loop extremum

$$v_1 = - \left. \frac{\partial_\phi V_1}{\partial_\phi^2 V_0} \right|_{v_0}, \quad (3.17)$$

and the two-loop extremum

$$v_2 = \left. \frac{-2\partial_\phi V_2 (\partial_\phi^2 V_0)^2 + 2\partial_\phi V_1 \partial_\phi^2 V_0 \partial_\phi^2 V_1 - (\partial_\phi V_1)^2 \partial_\phi^3 V_0}{2(\partial_\phi^2 V_0)^3} \right|_{v_0}. \quad (3.18)$$

The potential at the extremum is then given by

$$V(v) = V_0(v_0) + \hbar V_1(v_0) + \hbar^2 \left( V_2(v_0) - \frac{1}{2} \left. \frac{(\partial_\phi V_1)^2}{\partial_\phi^2 V_0} \right|_{v_0} \right) + \mathcal{O}(\hbar^3), \quad (3.19)$$

where each term is evaluated at the tree-level extremum  $v_0$ . In this expansion, the dependence on the gauge-fixing parameters cancels order by order according to Eq. (3.9), whereas the naive (numerical) minimization of the  $n^{\text{th}}$ -loop improved potential would lead to an uncancelled gauge-dependence in  $V(v)$ . However, in the presence of parametric enhancement of loop contributions — for instance, in the high-temperature regime (see Section 3.3) or for radiatively generated potential barriers [92] — the  $\hbar$ -expansion could lead to results that significantly deviate from the direct minimization method [73]. The fact that the potential at its extremum given in Eq. (3.19) is gauge-independent order by order (unlike the minimizing field value) has the noteworthy consequence that problematic behaviors of specific gauges—for instance, IR-divergences caused by massless Goldstone bosons in the Landau gauge—have to cancel out term by term in Eq. (3.19) [94].

---

<sup>5</sup>We only keep the powers of  $\hbar$  explicitly in this section for clarity and leave them implicitly in the rest of the paper.

For the cxSM, we have to minimize along two field directions  $\phi_h$  and  $\phi_s$ . The corresponding  $\hbar$ -expansion of the potential values at the extremum then reads

$$V(v_h, v_s) = V_0(v_{h,0}, v_{s,0}) + \hbar V_1(v_{h,0}, v_{s,0}) + \hbar^2 \left( V_2(v_{h,0}, v_{s,0}) - \frac{1}{2} \frac{(\partial_{\phi_s}^2 V_0) (\partial_{\phi_h} V_1)^2 + (\partial_{\phi_h}^2 V_0) (\partial_{\phi_s} V_1)^2 - 2(\partial_{\phi_h} \partial_{\phi_s} V_0) (\partial_{\phi_h} V_1) (\partial_{\phi_s} V_1)}{(\partial_{\phi_h}^2 V_0)(\partial_{\phi_s}^2 V_0) - (\partial_{\phi_h} \partial_{\phi_s} V_0)^2} \Big|_{v_{h,0}, v_{s,0}} \right) + \mathcal{O}(\hbar^3), \quad (3.20)$$

where all quantities are evaluated at the tree-level minimum  $\phi_h = v_{h,0}$  and  $\phi_s = v_{s,0}$ .<sup>6</sup>

### 3.2 Renormalization scale dependence

When working in a perturbative expansion, due to the truncation of the perturbative series at some loop order, one inevitably introduces a dependence of the effective potential on either the choices made for on-shell-type renormalizations or on the renormalization scale  $\mu$ . Focusing here on the latter case, there is both an explicit (logarithmic) dependence on the scale  $\mu$  and an implicit scale dependence of the couplings and the fields. The full  $\mu$ -dependence of the perturbatively evaluated effective potential is governed by the renormalization group equation<sup>7</sup>

$$\left( \mu \frac{\partial}{\partial \mu} - \gamma \phi \frac{\partial}{\partial \phi} + \beta_i \frac{\partial}{\partial g_i} \right) V = 0. \quad (3.21)$$

This equation shows that the explicit scale dependence of the effective potential cancels against the respective contributions from the scale dependence of the couplings  $g_i$  and the field  $\phi$ , expressed in terms of the  $\beta$ -functions  $\beta_i$  and the anomalous dimension  $\gamma$ .<sup>8</sup>

Equation (3.21) holds order by order in perturbation theory. For instance, the explicit scale dependence of the one-loop potential is canceled by the running of parameters and fields (which appears starting from one loop, i.e. at  $\mathcal{O}(\hbar)$ ) in the tree-level potential:

$$\mu \frac{\partial}{\partial \mu} V_1 = \left( \gamma_1 \phi \frac{\partial}{\partial \phi} - \beta_{i,1} \frac{\partial}{\partial g_i} \right) V_0, \quad (3.22)$$

where  $\gamma_1$  and  $\beta_{i,1}$  are the one-loop anomalous dimension and beta functions, respectively. The inclusion of the running of couplings and fields can therefore serve as a consistency check for the loop-improved potential. If one includes the running of parameters also in the

<sup>6</sup>However, it is not necessary to use the  $\hbar$ -expansion along the singlet field direction, because it is not charged under any gauge group and is therefore not affected by the gauge fixing.

<sup>7</sup>Note that this is just expressing the fact that  $dV/d\mu = 0$  if all loop orders are taken into account.

<sup>8</sup>There is an additional scale dependence of the effective potential: it depends on the initial scale  $\mu_{\text{in}}$  at which it is first determined before evolving it to another scale  $\mu$ . In our case, we have  $\mu_{\text{in}} = m_Z$  (see Appendix A). This additional scale dependence is governed by the RGE-like equation [95]

$$\mu_{\text{in}} \frac{\partial}{\partial \mu_{\text{in}}} V(\phi; \mu_{\text{in}}, \mu) = \gamma \phi \frac{\partial}{\partial \phi} V(\phi; \mu_{\text{in}}, \mu).$$

A complete study of this effect goes beyond the scope of our current work and we leave it for future studies.

*one-loop* effective potential, the residual, uncanceled scale dependence will be of two-loop order, *i.e.*

$$\left( \mu \frac{\partial}{\partial \mu} - \hbar \gamma_1 \phi \frac{\partial}{\partial \phi} + \hbar \beta_{i,1} \frac{\partial}{\partial g_i} \right) (V_0 + \hbar V_1) = \mathcal{O}(\hbar^2), \quad (3.23)$$

where we explicitly write out the powers of  $\hbar$  to indicate the respective loop orders for each term. This residual scale dependence propagates to the predictions for physical observables derived from the loop-improved potential, providing an estimate for the size of missing  $\mu$ -dependent higher-loop terms. Comparing the  $\mu$ -dependence of the prediction for an observable at increasing loop orders can be used to study the behavior of the perturbative expansion, and therefore serves as an important indicator of its validity when truncated at a certain loop order.

As an aside, we note that the potential may contain scale-dependent, but field-independent terms (*cosmological constant* or *vacuum energy* terms) whose running is not canceled by using loop-improved couplings. Such scale dependencies can be dealt with by including the running of a vacuum energy term in Eq. (3.21) (see Ref. [96]). Since field-independent terms in the potential are not relevant for the vacuum structure of the theory, we do not include the running of the vacuum energy in our numerical analysis.

### 3.3 Temperature corrections

In thermal field theory, the effective potential at non-zero temperature can be evaluated using the imaginary time formalism. For instance, at one-loop order, the integral in Eq. (3.6) is modified to

$$I^{4D}(M_i, T) = \frac{1}{2} \sum_p \log(p^2 + M_i^2) = I^{4D}(M_i)^{T=0} \mp T \int_{\vec{p}} \log(1 + n_{B/F}(E_{i,\vec{p}}, T)), \quad (3.24)$$

where we split the one-loop contributions into vacuum and temperature-dependent parts, while  $E_{i,\vec{p}} = \sqrt{M_i^2 + \vec{p}^2}$  and  $n_{B/F}$  refers to Bose-Einstein and Fermi-Dirac distributions for bosons and fermions, respectively. The sum-integral is taken over Matsubara modes  $\sum_p \equiv T \sum_n \int_{\vec{p}}$ , and the four-momenta become  $p = (\omega_n, \vec{p})$ . For bosons, we have  $\omega_n = 2n\pi T$  and for fermions  $\omega_n = 2(n + 1/2)\pi T$ . In the second term on the right-hand side of the equation, the integral is evaluated in  $d = 3$  momentum space, and it is commonly written in terms of thermal functions  $J_{B/F}$ ,

$$\begin{aligned} \mp T \int_{\vec{p}} \log(1 + n_{B/F}(E_{\vec{p}}, T)) &= \mp \frac{T^4}{2\pi^2} \int_0^\infty dx x^2 \log \left( 1 \pm \exp \left( -\sqrt{x^2 + \frac{M_i^2}{T^2}} \right) \right) \\ &\equiv \frac{T^4}{2\pi^2} J_{B/F} \left( \frac{M_i^2}{T^2} \right). \end{aligned} \quad (3.25)$$

For a phase transition to occur, the temperature-induced corrections to the effective potential must be large enough to qualitatively alter its structure. Therefore, the leading-order thermal corrections should be parametrically of the same order as the tree-level potential. This, in turn, implies that the usual loop expansion in general is not applicable, and a careful power counting is required.

For instance, in Ref. [97] it was shown that due to the differences between loop and coupling expansions for thermal phase transitions, in order to cancel the leading order (one-loop thermal) renormalization scale dependence at high temperatures, one has to add two-loop thermal mass contributions, so that the residual dependence is sub-leading.<sup>9</sup> This is in contrast to the zero temperature case, where the leading renormalization scale dependence of the couplings is canceled by the one-loop effective potential. Similarly, ensuring the cancellation of gauge-dependent contributions poses additional challenges at finite temperature, as the standard  $\hbar$ -expansion is no longer sufficient and must be replaced by a perturbative expansion formulated in terms of a (thermal) coupling.

In theories with gauge interactions, leading thermal corrections arise from one-loop self-energy diagrams and scale as  $\mathcal{O}(g^2 T^2)$ , where  $g$  is a generic gauge coupling in the theory. Under the assumption of perturbativity, these corrections can still be significant at sufficiently high temperatures due to the quadratic dependence on  $T$ . In this case, non-zero Matsubara modes are special; their effective thermal masses are of order  $\sim \pi T$  (*hard* modes), while zero modes, which could acquire a thermal screening mass  $m_D$ , are at most  $\sim gT$  (*soft* modes). This hierarchy of scales has important implications for perturbative calculations, since the vacuum diagrams of soft modes with additional petals of hard modes will all contribute at the same order, *i.e.*  $\mathcal{O}(g^3 T^2)$ . Accordingly, one must resum these diagrams in order to go beyond the leading order of  $\mathcal{O}(g^2 T^2)$ .

To this end, we can write the one-loop thermal effective potential integral for bosons as a sum of contributions from zero and non-zero Matsubara modes in the imaginary time formalism

$$I^{4D}(M_i, T) = \frac{1}{2}T \int_{\vec{p}} \log(\vec{p}^2 + M_i^2) + \frac{1}{2} \sum'_p \log(p^2 + M_i^2), \quad (3.26)$$

where the sum goes over all but zero Matsubara modes  $\sum'_p \equiv T \sum_{n \neq 0} \int_{\vec{p}}$ . The soft modes then can be resummed as  $M_i^2 \rightarrow M_i^2 + \Sigma_i^T$ , where  $\Sigma_i^T \sim g^2 T^2$  are the thermal self-energies of the soft modes that are summed. This leads to

$$\begin{aligned} I_{\text{resummed}}^{4D}(M_i, T) &= \frac{1}{2}T \int_{\vec{p}} \log(\vec{p}^2 + M_i^2 + \Sigma_i^T) + \frac{1}{2} \sum'_p \log(p^2 + M_i^2) \\ &= I^{4D}(M_i, T) - \frac{T}{12\pi} \left( (M_i^2 + \Sigma_i^T)^{3/2} - (M_i^2)^{3/2} \right). \end{aligned} \quad (3.27)$$

The last term is an additional contribution from the resummation, called a *daisy* term. The resummation of soft modes only, as in Eq. (3.27), is usually coined Arnold-Espinosa (AE) resummation [39]. An alternative method where one resums both, hard and soft modes, is the Parwani-type resummation [40].<sup>10</sup> Similar resummations can also be performed at

<sup>9</sup>Similar issues can be present at zero temperature for a radiatively generated barrier, where the two-loop contribution is required [95].

<sup>10</sup>Compared to AE resummation, Parwani resummation leads to a stronger temperature dependence of the scalar potential [27, 43] and potentially significantly larger predictions for the strength of the transition [25, 44, 71]. By inserting the thermally corrected masses also into the radiative corrections from non-zero Matsubara modes, the Parwani method mixes IR and UV dynamics. We checked that in the cxSM, the differences between AE and Parwani resummation are much below the theoretical uncertainties from residual gauge and renormalization scale dependence. We will therefore only consider the AE method in our paper.

higher-loop order [43, 98]. An alternative to the diagrammatic resummations is to solve the gap equation [41]. In our work, we determine the temperature-dependent potential at one-loop order with AE-type diagrammatic daisy resummation in various gauges (see Section 3.1) and compare those predictions with the ones from a high-temperature EFT.

### 3.4 High-temperature EFT

The deficiency of the usual loop expansion at high temperature is not surprising—it simply indicates a large separation of the scales at play. At high temperatures, those are: *hard* ( $\sim \pi T$ ), *soft* ( $\sim m_D \sim gT$ ) and *ultrasoft* ( $\sim g^2 T$ ) contributions.<sup>11</sup> These originate from non-zero Matsubara modes, temporal components of gauge fields and spatial gauge modes together with scalar fields, respectively.

Instead of performing a power counting and resummations by hand, the large separation between scales of the relevant physics can be taken into account using methods of effective field theories (EFTs). The dynamics of thermally driven phase transitions can be described via the so-called High-Temperature EFT [69, 100]. It allows to systematically integrate out hard and soft modes, leaving us with the field theory for the nucleating field, where large logarithms are resummed into effective couplings of the theory. This matching is often called *dimensional reduction*, as the effective theory is three-dimensional after integrating out the hard modes.

Schematically, the matching of mass parameters ( $\mu_\phi$ ), scalar self-couplings ( $\lambda_\phi$ ) and gauge ( $g$ ) couplings at the *hard* scale can be represented as

$$\begin{aligned}
\mu_{\phi,3D}^2 &= \overbrace{\underbrace{\mu_\phi^2}_{\text{tree}} + \underbrace{\#g^2 T^2}_{\text{1-loop}}}_{\mathcal{O}(g^2)} + \overbrace{\underbrace{\#g^2 \mu_\phi^2}_{\text{1-loop}} + \underbrace{\#g^4 T^2}_{\text{2-loop}}}_{\mathcal{O}(g^4)} + \mathcal{O}(g^6), \\
\lambda_{\phi,3D} &= \overbrace{\underbrace{\lambda_\phi T}_{\text{tree}}}_{\mathcal{O}(g^2)} + \overbrace{\underbrace{\#g^4 T}_{\text{1-loop}}}_{\mathcal{O}(g^4)} + \mathcal{O}(g^6), \\
g_{3D}^2 &= \overbrace{\underbrace{g^2 T}_{\text{tree}}}_{\mathcal{O}(g^2)} + \overbrace{\underbrace{\#g^4 T}_{\text{1-loop}}}_{\mathcal{O}(g^4)} + \mathcal{O}(g^6),
\end{aligned} \tag{3.28}$$

where  $\mu_{\phi,3D}$ ,  $\lambda_{\phi,3D}$  and  $g_{\phi,3D}$  are the corresponding parameters in the dimensionally reduced 3D EFT. Here, with underbraces we indicate which loop order contributes to the matching while overbraces show the respective coupling order when assuming the scaling  $\mu_\phi^2 \sim g^2 T^2$ ,  $\lambda_\phi \sim g^2$ , as is customary for strong thermal phase transitions [97]. Expressions of the form  $\#g^n$  denote dimensionless factors at  $\mathcal{O}(g^n)$ , which generally depend on the scalar self-couplings and gauge charges.

The truncation of the matching at a given loop order introduces a residual dependence on the *hard* matching scale  $\mu = \pi T$ . The relations in Eq. (3.28) are modified when inte-

<sup>11</sup>For radiatively generated potential barriers, an additional *softer* (also called *supersoft*) scale ( $\sim g^{3/2} T$ ) appears, which characterizes the nucleation scale [99]. In the cxSM, the barrier is not radiatively induced, such that the *softer* scale is not relevant.

grating out the *soft* scale  $\mu_{3D}^{\text{soft}} = m_D$ . This gives rise to contributions with odd powers of  $g$ , starting with  $\mathcal{O}(g^3)$ . The high-temperature EFT matching procedure has been automated in DRalgo [70] up to  $\mathcal{O}(g^4)$  for generic models. In Fig. 3 we present a schematic depiction of the matchings and subsequent running of parameters within the dimensional reduction approach as applied here to study the EW phase transition in the cxSM. Within the dimensionally reduced 3D theory, only the mass parameters  $\mu_{\phi,3D}$  run, starting at two-loop order [101].

For the cxSM, the mass parameters are  $\mu_\phi = \{\mu_h, \mu_s\}$ , and the quartic couplings  $\lambda_\phi = \{\lambda_h, \lambda_s, \lambda_{hs}\}$ . Dimensional reduction for the SM with an additional singlet was studied extensively in the past [101–103], and the matching relations that are relevant in this work can be found in [77]. For illustration, here we explicitly give the leading one-loop matching conditions for the mass parameters,

$$\begin{aligned}\mu_{h,3D}^2 &= \mu_h^2 + \frac{1}{48}T^2 (3g'^2 + 9g^2 + 12y_t^2 + 2\lambda_{hs} + 24\lambda_s), \\ \mu_{s,3D}^2 &= \mu_s^2 + \frac{1}{6}T^2 (\lambda_s + \lambda_{hs}),\end{aligned}\tag{3.29}$$

where the  $\mathcal{O}(T^2)$  terms coincide with the leading finite-temperature corrections to the classical scalar potential in the high-temperature expansion. We explore the impact of the matching accuracy on thermodynamic observables and the description of the EW phase transition in the cxSM in detail in Section 4.

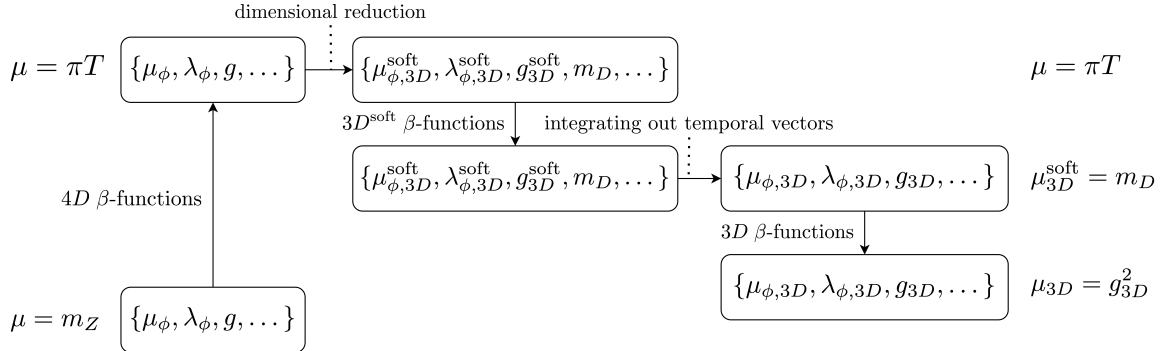


**Figure 3:** Illustration of the procedure for systematically integrating out relevant thermal scales within the dimensional reduction approach. Starting from the initial scale ( $\mu \sim m_Z$ ), Lagrangian parameters—determined from physical input parameters (see Section A.1)—are evolved to the *hard* scale ( $\mu \sim \pi T$ ), where the full theory is matched to the dimensionally reduced EFT. The effective couplings are then evolved to the *soft* scale ( $\mu_{3D}^{\text{soft}} \sim m_D$ ), where temporal vector modes are subsequently integrated out, yielding the final EFT used to compute thermodynamic observables at the *ultrasoft* scale, characterized by the gauge coupling ( $\mu_{3D} \sim g_{3D}^2$ ).

The validity of the high-temperature EFT, which formally breaks down if  $m_{h,s}/(\pi T) \gtrsim 1$ , can be investigated through the impact of including higher-dimensional operators in the EFT on the obtained results. To assess the validity of truncating the EFT expansion at dimension-four operators, we perform the matching of dimension-six scalar operators in the

cxSM in the Landau gauge with the help of DRalgo [70]. Parametrically appearing at  $\mathcal{O}(g^6)$  in the matching, they appear in the EFT tree-level potential as:

$$V_0^{3D} \supset c_{h^6}(\Phi^\dagger\Phi)^3 + c_{h^4s^2}(\Phi^\dagger\Phi)^2|S|^2 + c_{h^2s^4}\Phi^\dagger\Phi|S|^4 + c_{s^6}|S|^6, \quad (3.30)$$

and the Wilson coefficients read:

$$\begin{aligned} c_{h^6} &= \frac{\zeta(3)}{6144\pi^4} (3g'^6 + 9g'^4g^2 + 9g'^2g^4 + 9g^6 + 2(-336y_t^6 + \lambda_{hs}^3 + 960\lambda_h^3)), \\ c_{h^4s^2} &= \frac{\zeta(3)}{512\pi^4} \lambda_{hs} (\lambda_{hs}(\lambda_s + \lambda_{hs}) + 12\lambda_{hs}\lambda_h + 48\lambda_h^2), \\ c_{h^2s^4} &= \frac{\zeta(3)}{1024\pi^4} \lambda_{hs} (5\lambda_s^2 + 6\lambda_s\lambda_{hs} + 2\lambda_{hs}(\lambda_{hs} + 6\lambda_h)), \\ c_{s^6} &= \frac{\zeta(3)}{1536\pi^4} (7\lambda_s^3 + \lambda_{hs}^3). \end{aligned} \quad (3.31)$$

We use this subset of dimension-six operators to assess the validity of the EFT expansion. For this purpose, we do not take into account the gauge-dependence of these matching relations [104], further operators at this order which include derivatives [105] or corrections to the RGE running from the higher-dimensional operators [106]. The impact of the operators in Eq. (3.30) on thermodynamic observables is discussed in Section 6. It should be noted that in the dimensionally reduced theory, scalar fields have mass dimension 1/2, hence the Wilson coefficients in Eq. (3.31) are dimensionless. However, we refer to them as dimension-six operators, as they correspond to operators with mass dimension six in 4D.

In the 3D EFT resulting from dimensional reduction at high temperature, temperature is no longer a dynamical variable but enters only through the effective parameters of the theory. After matching, the effective potential can be calculated within the EFT in the usual perturbative manner. At one-loop order, this corresponds to defining the effective potential of Eq. (3.5) in terms of the one-loop integrals of Eq. (3.7), evaluated in three dimensions. At the next order, one takes into account the contributions from the two-loop prototype diagrams (see Eq. (3.8) and Fig. 2).

In the present work, we calculate the effective potential within the dimensionally reduced theory in  $R_\xi$ -gauge up to two-loop order. Compared to the algorithmically generated effective potential in DRalgo [70], which is computed in the Landau gauge, the two-loop potential in  $R_\xi$ -gauge contains additional diagrams, namely ghost–ghost–scalar vacuum prototype graphs (see Fig. 4), and the mass eigenvalues of vectors, Goldstone scalars and ghosts are altered (see Appendix B for details). After incorporating the contributions from these additional diagrams and the  $R_\xi$ -dependent masses, we explicitly checked that the expression for the potential evaluated in  $R_\xi$ -gauge becomes gauge-independent in the  $\hbar$ -expansion at the tree-level minima and that it reproduces the potential in the Landau gauge in the  $\xi \rightarrow 0$  limit. This serves as a highly non-trivial check of the newly introduced contributions to the potential and the inherent intricate gauge cancellations at the two-loop level.

As mentioned previously, the explicit dependence on the EFT renormalization scale  $\mu_{3D}$  appears in the effective potential at the two-loop level. We explore the dependence of thermodynamic observables on  $\mu_{3D}$  in Section 4.1 in order to assess the related theoretical uncertainties in the description of the EW phase transition. We compare the uncertainty

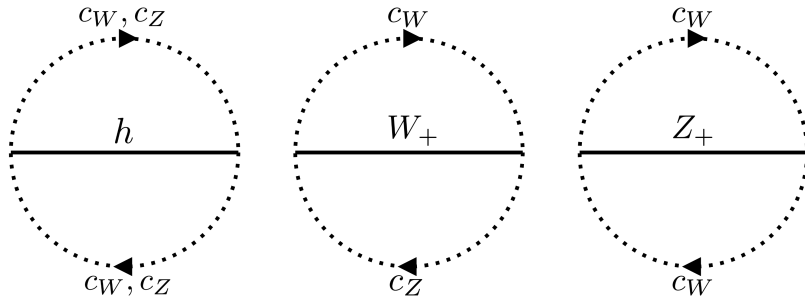


**Figure 4:** Two-loop ghost–ghost–scalar prototype diagrams that appear in the effective potential in  $R_\xi$ -gauge, but are absent in the Landau gauge. See Appendix B for the gauge-dependent mass eigenvalues used in their evaluation.

related to the dependence on the renormalization scale with the one resulting from residual gauge dependence (if the  $\hbar$ -expansion is not applied).

## 4 Thermodynamics of the First Order Phase Transition

In this section, we numerically investigate the effects of thermal corrections on phase transition dynamics in a comparison of various possible approaches to the problem. As discussed in Section 2, we focus on the case of the flip-flop scenario in the cxSM. We study parameter regions where the EW phase transition can be of first order and would potentially be strong enough to produce detectable primordial stochastic GW backgrounds. The thermodynamics of a FOEWPT can be formally split into two parts: equilibrium thermodynamics, which is characterized by the critical temperature and latent heat, and nucleation thermodynamics, which describes the nucleation of the new phase.

### 4.1 Critical temperature and latent heat

In studies of phase transition thermodynamics, one of the central observables is the critical temperature,  $T_c$ . It is defined as the temperature at which the pressures — given by  $p = -V^{4D}$  in each minimum in the  $d = 4$  theory and by  $p = -TV^{3D}$  in the dimensionally reduced theory, see Section 3.4, where  $V^{4D}$  and  $V^{3D}$  are the potential values at the minima — at two coexisting local minima are equal.

To characterize the strength of the phase transition, we compute the latent heat at the critical temperature,  $L_c$ , which quantifies the difference in energy density,  $\rho = T(\partial p/\partial T) - p$ , between two phases:

$$L_c \equiv L(T_c) = \Delta\rho|_{T=T_c} = T_c \left. \frac{d\Delta p}{dT} \right|_{T=T_c} = -T_c \left. \frac{d\Delta V}{dT} \right|_{T=T_c}. \quad (4.1)$$

Here,  $\Delta V = -\Delta p$  is the difference in the effective potential between high and low temperature phases. For a FOEWPT,  $L_c$  represents the discontinuous release of energy as the system moves from a metastable phase to a stable broken symmetry phase. A large latent heat corresponds to a strong FOEWPT, which is essential for scenarios like EW baryogenesis, where a significant departure from thermal equilibrium is necessary to generate and

maintain the baryon asymmetry. Additionally, sufficiently strong FOEWPTs can produce GWs (see Section 5) with peak amplitudes in reach of future space-based GW observatories.

In this section, we will discuss the scale and gauge dependence of  $T_c$  and  $L_c$  for the EW phase transition predicted in the cxSM using the following set of approaches:

- (a) the **4D approach** with the effective potential at one-loop order, including the AE-type daisy resummation of Eq. (3.27) (unless stated otherwise) and two different sets of relations between physical input and Lagrangian parameters at the one-loop level:  $\overline{\text{MS}}$ - and OS-like scheme (denoted  $\widetilde{\text{OS}}$ ), see Appendix A for details. We evaluate the effective potential as

$$V^{4D}(\phi_h, \phi_s, T; \mu, \xi) = V_0(\phi_h, \phi_s) + V_1^{T=0}(\phi_h, \phi_s; \mu, \xi) + V_1^{T \neq 0}(\phi_h, \phi_s, T; \xi) + V_{\text{daisy}}(\phi_h, \phi_s, T; \xi), \quad (4.2)$$

where we construct the one-loop temperature-dependent potential using Eqs. (3.5) and (3.24) and add the contribution from daisy resummed diagrams as in Eq. (3.27). For the latter, we only use the leading-order thermal screening masses. In the  $\overline{\text{MS}}$ -scheme, we use one-loop improved Lagrange parameters (Eq. (A.10)) in each part of the effective potential Eq. (4.2). In the  $\widetilde{\text{OS}}$ -scheme, a UV-finite counterterm piece  $V_{\text{CT}}$  is added to the potential, which shifts the parameters such that the first and second derivatives of the potential  $V^{4D}$  in the tree-level minimum  $(\phi_h, \phi_s) = (v_h, 0)$  are the same as the ones of the tree-level potential  $V_0$ . This ensures that the scalar vevs and masses derived from  $V^{4D}$  remain at their tree-level values within the  $\widetilde{\text{OS}}$  prescription based on the effective potential, which, however, does not account for momentum-dependent radiative corrections (see Eq. (A.16) for details).

- (b) the **3D approach** based on the high-temperature EFT using dimensional reduction (see Section 3.4 for details) and  $\overline{\text{MS}}$ -relations.<sup>12</sup> In this case, we evaluate the effective potential up to two-loop order within the effective theory

$$V^{3D}(\phi_h, \phi_s, \mu_{3D}, \xi) = V_0^{3D}(\phi_h, \phi_s) + V_1^{3D}(\phi_h, \phi_s; \xi) + V_2^{3D}(\phi_h, \phi_s; \mu_{3D}, \xi). \quad (4.3)$$

The temperature dependence of the potential arises implicitly through the effective couplings as shown in Eq. (3.28). The dependence on the *hard* matching scale  $\mu$  (see Fig. 3 for a schematic depiction of the matching procedure) also arises implicitly through the effective couplings of the theory, whereas the dependence on the *ultrasoft* scale  $\mu_{3D}$  is explicit in  $V_2^{3D}$ . Unless specified otherwise, in the 3D approach we apply  $\mathcal{O}(g^4)$  matching and integrate out *hard* and *soft* scales.

---

<sup>12</sup>To apply the  $\widetilde{\text{OS}}$ -scheme in the 4D approach, one makes use of the fact that the effective potential can be separated into a  $T = 0$  part (first line on the right-hand side of Eq. (4.2)) and a part that explicitly depends on the temperature (second line of Eq. (4.2)). The counterterm potential is then defined using only the  $T = 0$  part of the potential. In the 3D EFT approach, the explicit temperature dependence enters into all terms of the potential from the matching conditions of the effective potential parameters, such that one cannot split the potential into a  $T = 0$  part and a part that explicitly depends on  $T$ . We therefore do not apply an  $\widetilde{\text{OS}}$ -scheme in the 3D approach.

In this section, we use a reference parameter point with the singlet mass fixed to  $m_s = 100 \text{ GeV}$  and the singlet self-coupling fixed to  $\lambda_s = 1$ , while varying the remaining free parameter of the cxSM in the range  $\lambda_{hs} \in [1, 1.3]$ . In this parameter range, we find a thermodynamic behavior compatible with strong FOEWPTs. For larger values of the portal coupling  $\lambda_{hs}$  (with the other parameters kept fixed), we find that the low-temperature global minimum is not the EW one, preventing the onset of an EW phase transition during the evolution of the universe. On the contrary, for smaller values of  $\lambda_{hs}$ , there is no strong first-order EW phase transition. We further analyze parameter planes in which  $\lambda_s$  is kept fixed and both  $m_s$  and  $\lambda_{hs}$  are varied in Section 5, including a phenomenological discussion of the resulting GW signals and the experimental prospects for their detection at future experiments. In the remainder of this section, unless specified otherwise (*i.e.* when using the  $\hbar$ -expansion), we directly minimize the real part of the effective potential to determine the relevant thermodynamic quantities. <sup>13</sup>

#### 4.1.1 Scale dependence

We first investigate the scale dependence in the predictions for the critical temperature  $T_c$  and latent heat  $L_c$  using the different approaches discussed above. In the left plot of Fig. 5 we show with the solid lines the predictions for  $T_c$  as a function of  $\lambda_{hs}$  using the  $4D$  approach in the  $\overline{\text{MS}}$ -scheme and the  $\widetilde{\text{OS}}$ -scheme with the orange and red lines, respectively, and using the  $3D$  approach with the blue line. The colored shaded bands around these lines result from a variation of the renormalization and matching scale  $\mu$  by a factor of 2 around the central values  $\mu_0^{\overline{\text{MS}}} = \pi T_c$  and  $\mu_0^{\widetilde{\text{OS}}} = v$  in the  $\overline{\text{MS}}$ - and the  $\widetilde{\text{OS}}$ -scheme, respectively. These results were obtained from the effective potential in the Landau gauge, and the determination of the degenerate minima was carried out by numerically minimizing the loop-improved potential (without applying the  $\hbar$ -expansion).<sup>14</sup> The widths of the bands illustrate the theoretical uncertainties related to the renormalization scale dependence. Across the entire  $\lambda_{hs}$  range, we find that the renormalization scale dependence is significantly reduced in the  $3D$  approach compared to the  $4D$  approaches.

While the orange and the red bands representing the  $4D$  approaches overlap over the whole range of  $\lambda_{hs}$  shown, their slopes slightly differ. The  $\overline{\text{MS}}$ -scheme predicts smaller values of  $T_c$  at the upper end of the  $\lambda_{hs}$ -range, and the  $\widetilde{\text{OS}}$ -scheme predicts smaller values of  $T_c$  at the lower end of the  $\lambda_{hs}$ -range. This difference results from the different origins of the scale dependence. In the  $\overline{\text{MS}}$ -scheme, it is determined by the one-loop RGE running of the couplings, while for the  $\widetilde{\text{OS}}$ -scheme, it results from the scale dependence of the one-loop  $\widetilde{\text{OS}}$  counterterms (which does not necessarily coincide with the RGE running).<sup>15</sup> Additionally, differences between the two schemes arise due to the different choices for the central scales  $\mu_0$ . The  $\overline{\text{MS}}$  approach uses a variable central scale  $\mu_0 = \pi T_c$ , while the  $\widetilde{\text{OS}}$

<sup>13</sup>The imaginary part of the effective potential is related to the decay rate of the homogeneous state [107].

<sup>14</sup>The direct numerical minimization of the two-loop effective potential can give rise to a spurious logarithmic divergence originating from the triple Higgs sunset diagram [72]. This feature is not problematic for the present investigation, since, for the case of a strong first-order phase transition, the divergence does not occur near the local minima in field space.

<sup>15</sup>For the  $4D$ - $\overline{\text{MS}}$  approach, our findings agree with the ones reported in Ref. [47].

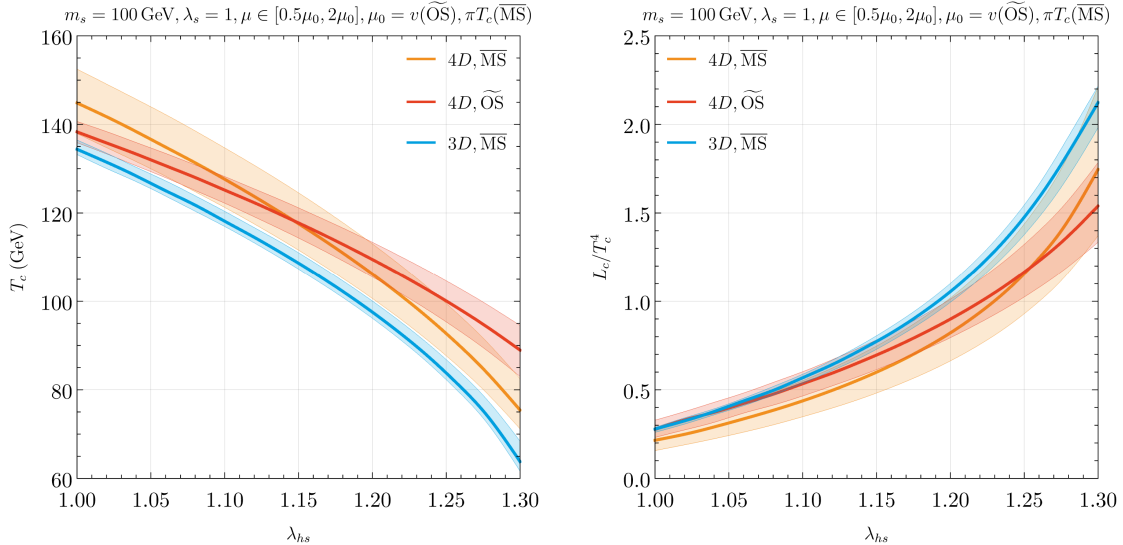


**Figure 5:** Critical temperature (*left*) and latent heat (*right*) for  $m_s = 100 \text{ GeV}$ ,  $\lambda_s = 1$ ,  $\lambda_{hs} \in [1, 1.3]$  determined by direct potential minimization in the Landau gauge. For the 4D approaches, the shaded bands around the solid lines are obtained from a variation of the renormalization scale by a factor of 2, with the central value being fixed at  $\mu = \pi T$  and  $\mu = v$  for  $\overline{\text{MS}}$  and  $\widetilde{\text{OS}}$  renormalization schemes, respectively (see text for details). For the 3D approach, the shaded band results from a variation of the *hard* matching scale by a factor of two around the central value  $\mu = \pi T$ .

one has its central scale fixed at  $\mu_0 = v_{h,0}$ . Therefore, a stronger parametric dependence for the former approach becomes visible, especially in the parameter regions where  $T_c$  changes quickly. Compared to the blue band representing the 3D approach, we observe that it lies below the other two bands, only showing an overlap with the other bands at the smallest values of  $\lambda_{hs}$  shown. This discrepancy between the 3D and the 4D approaches suggests that a scale variation with a factor of two might not be sufficient for a robust estimation of the theory uncertainty related to missing higher-order contributions in the perturbative expansion, and instead a wider scale variation or other ways to estimate the theoretical uncertainties should be considered. In addition, it should be taken into account that the 3D approach suffers from an additional theoretical uncertainty from the truncation of the high- $T$  EFT at dimension four, which is discussed in detail in Section 6.

In the right plot of Fig. 5, we show the predictions for the latent heat  $L_c$  defined in Eq. (4.1) using the three approaches, where the definitions of the solid lines and the colored bands are as in the left plot of Fig. 5. For the latent heat, we find a better agreement between the 4D and the 3D approaches compared to the predictions for the critical temperature  $T_c$ . As for  $T_c$ , the smallest theoretical uncertainty from the scale variation is found using the dimensionally reduced EFT. For the strongest transitions at the upper end of the depicted  $\lambda_{hs}$ -range, the blue band for the 3D approach lies entirely above the red band corresponding to the 4D- $\widetilde{\text{OS}}$ -approach, but it still overlaps with the orange band corresponding to the 4D- $\overline{\text{MS}}$ -approach. This suggests that in particular for the 4D- $\widetilde{\text{OS}}$ -approach the renormalization

scale variation by a factor of 2 does not fully capture the theory uncertainty from missing higher orders.

As discussed in Section 3.2, the renormalization scale dependence in the 4D approach has different origins. The effective potential exhibits both an explicit scale dependence and an implicit scale dependence from the RGE running of the couplings and fields. In order to investigate the main sources of the uncertainty stemming from the scale variation, we show in the left plot Fig. 6 the predictions for  $T_c$  in the 4D- $\overline{\text{MS}}$  approach with the RGE running effects included in different parts of the effective potential. As before, the solid lines show the predictions for the central choice  $\mu = \pi T_c$ , while the shaded bands indicate the uncertainty in  $T_c$  from a variation of  $\mu$  by a factor of 2. When including no RGE running at all (yellow), we find a sizable impact of the scale variation which can be attributed solely to the explicit scale dependencies in  $V_1^{T=0}$ . As expected from Eq. (3.21), including the running only in the tree-level part almost completely cancels out the scale dependencies, which gives rise to the very small black uncertainty band. However, this should not be interpreted as an indication of small theory uncertainty, since the potential size of missing higher-order corrections is largely encoded in the RG-improved one-loop contributions. As such, the apparent insensitivity to the renormalization scale in this setup does not provide a reliable estimate of the theory uncertainty from the two-loop corrections or of the behavior of the perturbative expansion.

Including the running also in the zero-temperature one-loop piece of the effective potential  $V_1^{T=0}$  leads to a slightly larger uncertainty band (brown). Since the one-loop RGE running included in  $V_1^{T=0}$  is formally of two-loop order, this dependence on  $\mu$  can be used as an estimate for missing higher-order corrections in the  $T = 0$  part of the potential. The main scale dependence, however, comes from the inclusion of the parameter running in the thermal part of the effective potential, which dominates for higher temperatures (orange, showing the full result, which is the same as in the left plot of Fig. 5). This is apparent by the scale variation becoming more pronounced in this case, despite the scale dependence of  $V_1^{T=0}$  being cancelled. Moreover, as a consequence of the growing temperature corrections with increasing temperature, the orange band width grows in size for higher temperatures, while the opposite is true for the case where no running effects are included (yellow).

As discussed in Section 3.4, in the 3D approach the theory uncertainty from missing higher orders can be estimated from the dependence on the hard matching scale  $\mu$  (the dependence on the renormalization scale  $\mu_{3D}$  is discussed below). In the right plot of Fig. 6 we show the scale dependence of the predictions for the critical temperature at different matching orders in the dimensionally reduced EFT. As before, the solid lines indicate the predictions for  $T_c$  with the scale set to the central choice  $\mu = \pi T_c$ , and the shaded bands indicate the uncertainty originating from a variation of the matching scale by a factor of 2. For the sake of separating uncertainties originating from various sources, we keep the effective potential at two-loop order for all matching orders. We observe that a matching at the leading  $\mathcal{O}(g^2)$  accuracy (purple) gives rise to a significant scale dependence and a large theory uncertainty which surpasses the uncertainty from the renormalization scale dependence in the 4D approach shown in the left plot of Fig. 6. The scale dependence in the 3D approach is reduced at the lower end of the  $T_c$  values depicted in the plot if a

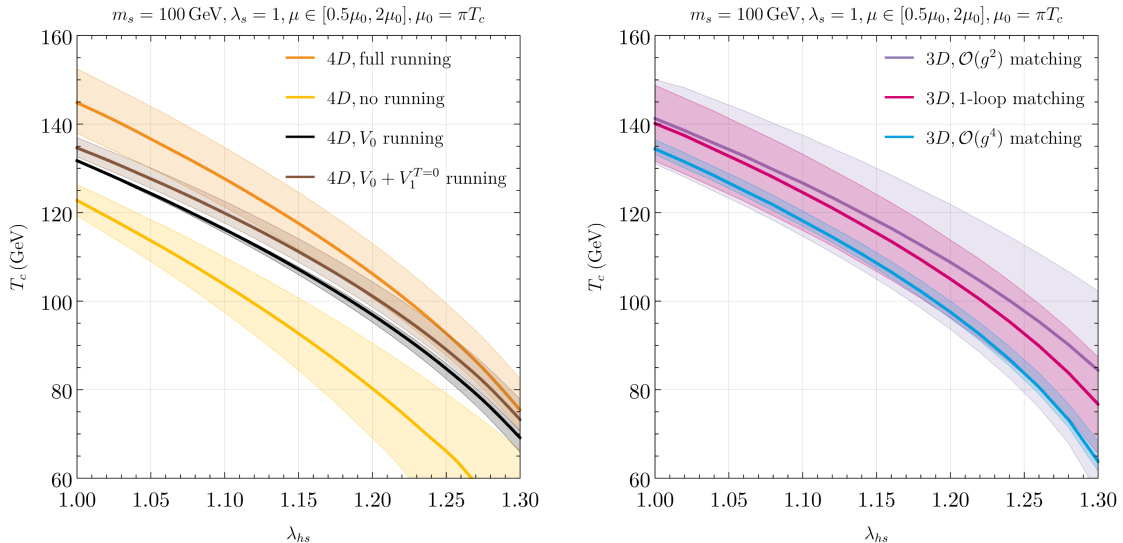


**Figure 6:** Scale-dependence of the critical temperature when using the  $\overline{\text{MS}}$ -input scheme in different settings: including the RGE running of Lagrange parameters in different parts of the effective potential in the 4D approach (*left*) and using different matching orders in the 3D approach (*right*).

matching at the full one-loop level is carried out (magenta), which contains the corrections of  $\mathcal{O}(g^2)$  and partially accounts for corrections of  $\mathcal{O}(g^4)$  (see Eq. (3.28)).<sup>16</sup> However, for the largest values of  $T_c$  shown in the plot, the dependence on the hard matching scale is barely reduced at one-loop matching accuracy. The blue band indicates the results when including two-loop contributions and a matching at full NLO  $\mathcal{O}(g^4)$  is carried out. This is the same result as in the left plot of Fig. 5. We see that the NLO matching reduces the scale dependence over the whole range of  $\lambda_{hs}$  by a factor of about five. Notably, only at  $\mathcal{O}(g^4)$  matching accuracy the scale dependence in the 3D approach is smaller than the renormalization scale dependence in the 4D approach shown in the left plot of Fig. 6. This demonstrates the necessity of working at  $\mathcal{O}(g^4)$  matching accuracy in order to reduce theory uncertainties by applying dimensional reduction and working in the high-temperature EFT.

In addition to the dependence on the hard matching scale  $\mu$ , the effective potential in the 3D EFT shows a dependence on the renormalization scale  $\mu_{3D}$ . As shown in Eq. (4.3), in 3D the explicit dependence on the renormalization scale enters only at the two-loop level, whereas the dependence in the tree-level and one-loop pieces of the effective potential is only implicit via the RGE running of the parameters. Specifically for the cxSM, we can write

$$V^{3D} = V_0^{3D}(\mu_{h/s,3D}^2(\mu_{3D})) + V_1^{3D}(\mu_{h/s,3D}^2(\mu_{3D})) + V_2^{3D}(\mu_{3D}; \mu_{h/s,3D}^2(\mu_{3D})), \quad (4.4)$$

where the explicit  $\mu_{3D}$ -dependence appears in  $V_2^{3D}$ , and the RGE running of the mass parameters  $\mu_{h,3D}^2$  and  $\mu_{s,3D}^2$  gives rise to the  $\mu_{3D}$ -dependence in  $V_0^{3D}$  and  $V_1^{3D}$ .

<sup>16</sup>Our one-loop results within the three-dimensional framework are in agreement with those presented in Ref. [77].

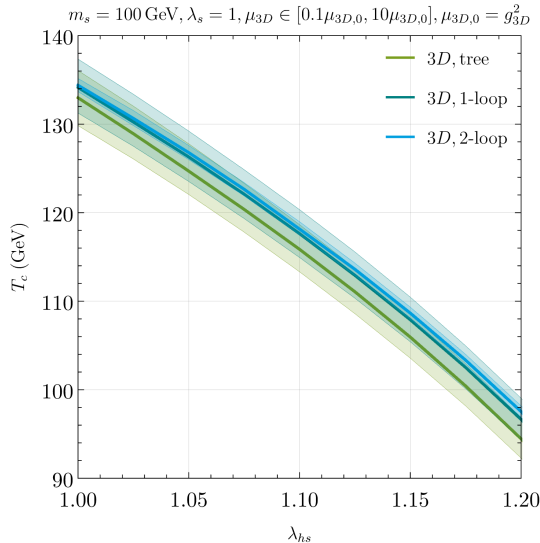


**Figure 7:** Variation of  $T_c$  with the  $3D$  renormalization scale  $\mu_{3D} \in [\mu_0/10, 10\mu_0]$  for different loop orders within the  $3D$  approach.

The dependence of the critical temperature  $T_c$  on the renormalization scale  $\mu_{3D}$  (for fixed  $\mu$ ) within the EFT is shown in Fig. 7 for the tree-level, one-loop and the two-loop effective potential, where we vary the scale around a central value  $\mu_{3D} = g_{3D}^2$ , where  $g_{3D}$  is the SU(2) charge of the effective theory. The dependence on the EFT scale  $\mu_{3D}$  is of far smaller magnitude than the one on the *hard* matching scale  $\mu$  (see the discussion above), even if only the tree-level potential is used. In order for the  $\mu_{3D}$ -variation to be visible at all in Fig. 7, we therefore show a variation around the central value by a factor of ten, in contrast to the factor of two for the  $\mu$ -variation, and we narrow down the shown range for the portal coupling  $\lambda_{hs}$ . The explicit renormalization scale dependence in  $V_2^{3D}$  cancels the implicit scale dependence of the couplings  $\mu_{h,3D}^2$  and  $\mu_{s,3D}^2$  in the tree-level  $V_0^{3D}$ , while the residual uncanceled scale-dependence comes from including the running of couplings in  $V_1^{3D}$  and  $V_2^{3D}$ . In agreement with this expectation, we find that the renormalization scale dependence cancels to a large degree at the two-loop level (blue), while the results merely receive an overall shift but no reduction of the scale dependence when comparing the predictions at tree-level (green) and one-loop level (teal). Moreover, the overlap of the three different bands suggests a good loop convergence within the EFT.

Finally, the effective potential in the  $3D$  EFT depends on a third soft scale  $\mu_{3D}^{\text{soft}}$ , which appears at the intermediate step of integrating out temporal components of the gauge fields. We find that the residual dependence on  $\mu_{3D}^{\text{soft}}$ , which appears as the scale of integrating out temporal vectors (see Fig. 3), is quantitatively insignificant. According to our findings discussed in this section, in the discussion in Section 5 below on the impact of theoretical uncertainties from residual scale dependencies on the GW signals, we include only the uncertainty associated with the hard matching scale  $\mu$ , as it was found to be substantially larger than the uncertainties arising from the renormalization scale  $\mu_{3D}$  and the soft scale  $\mu_{3D}^{\text{soft}}$ . We do, however, include two additional sources of theory uncertainty from the residual

gauge dependence and the breakdown of the 3D high-temperature EFT at low temperatures, which we estimate by studying the impact of higher-dimensional operators in the EFT, as discussed in detail in Section 4.1.2 and Section 6, respectively.

### 4.1.2 Gauge dependence

Next, we compare the different methods in terms of the residual gauge-dependence of the results. For this, we choose the following gauge fixing condition for the cxSM in the basis of mass-eigenstates after electroweak symmetry breaking:

$$\mathcal{L}_{GF} = -\frac{1}{2} (F_\gamma^2 + F_Z^2 + 2F_W^+ F_W^-), \quad (4.5)$$

with

$$F_\gamma = -\frac{1}{(\xi_1^\gamma)^{1/2}} \partial^\mu A_\mu, \quad (4.6)$$

$$F_Z = -\frac{1}{(\xi_1^Z)^{1/2}} \left( \partial^\mu Z_\mu + i\xi_2^Z \frac{\sqrt{g^2 + g'^2} \phi^{GF}}{2} G_0 \right), \quad (4.7)$$

$$F_W^\pm = -\frac{1}{(\xi_1^W)^{1/2}} \left( \partial^\mu W_\mu^\pm \mp i\xi_2^W \frac{g \phi^{GF}}{2} G_\pm \right), \quad (4.8)$$

where  $\xi_1^{Z,W,\gamma}$ ,  $\xi_2^{Z,W}$  and  $\phi_i^{GF}$  are the gauge-fixing parameters. We suppress the superscripts ( $Z, W, \gamma$ ) in the following for better readability. Some commonly used choices for the gauge-fixing parameters, which we study in the presented work, are

1. **Fermi gauge:**  $\xi_1 = \xi$ ,  $\xi_2 = 0$ . In this case, ghosts become massless, but calculations are complicated by the presence of mixing propagators between vector bosons and the corresponding Goldstone bosons. Moreover, infrared (IR) divergences arise, necessitating additional resummation procedures [108].
2.  **$R_\xi$ -gauges:**  $\xi_1 = \xi_2 = \xi$ .<sup>17</sup> These are usually introduced to cancel the aforementioned mixing propagators. Two subclasses can be defined here:
  - (a) In the so-called *background*  $R_\xi$ -gauge, one uses  $\phi^{GF} = \phi_h$ . Thence, the vector-Goldstone mixing is canceled for all values of the background field  $\phi_h$ , and ghosts become massive.
  - (b) In the *standard*  $R_\xi$ -gauge, one uses  $\phi^{GF} = v_h$ . Here, the vector-Goldstone mixing is canceled only at the minimum field configuration  $\phi_{h,\min} = v_h$ , and the ghosts are massive. Note that in this gauge, the effective potential is not symmetric under  $\phi_h \rightarrow -\phi_h$ .
3. **Landau gauge** is a limit of both Fermi and  $R_\xi$ -gauges with  $\xi \rightarrow 0$ .<sup>18</sup> Ghosts are massless and mixing propagators are absent.

<sup>17</sup>Note that in general,  $\xi_1$  and  $\xi_2$  run differently under the RGE flow [89]. However, this only becomes relevant at the two-loop order in the effective potential in 4D, which we do not consider in this work.

<sup>18</sup>This is a fixed point of the RGE.

We list the gauge-dependent mass eigenstates of the cxSM in different gauges explicitly in Appendix B. In our work, we will employ the *background*  $R_\xi$ -gauge and take all  $\xi^{W,Z,\gamma} = \xi$ , except where explicitly mentioned otherwise, which allows us to analyze the numerical impact of residual gauge dependence by continuously varying the gauge-fixing parameter  $\xi$ .

A few comments on the *background* vs. the *standard*  $R_\xi$ -gauge are in order. The former has the advantage that propagator mixing between Goldstone bosons and vector fields is avoided for all field values, which significantly simplifies the form of the effective potential beyond tree-level. Though this comes at a price: the effective potential in this gauge cannot be used as a generating functional for all  $n$ -point correlation functions at zero momentum. More specifically, starting from two-point functions at one-loop order, there is a mismatch between the regular Feynman-diagrammatic calculation (*e.g.* the scalar self-energy at one-loop) and the second field derivative of the effective potential in the *background*  $R_\xi$ -gauge. The mismatch appears because taking derivatives of  $V$  w.r.t.  $\phi_h$  does not commute with setting  $\phi^{GF} \rightarrow \phi_h$ . This is in principle known from Ref. [90] where it was denoted as “*bad gauge*”, but this fact has not been emphasized very much in the literature in this context. Somewhat accidentally, though, there is no mismatch between one-loop tadpole diagrams and the first field derivatives of  $V$  [90]. For the use of the effective potential and the effective action to describe phase transitions, the difference between the two  $R_\xi$ -gauges matters, as the variation of the background scalar field value is the essence of the computations. For the effective potential in the cxSM we have explicitly verified that only the effective potential in the *standard*  $R_\xi$ -gauge reproduces  $n$ -point functions calculated perturbatively at zero external momentum. However, in our analysis below, we also include the results obtained in the *background*  $R_\xi$ -gauge, as it is frequently used in the studies of phase transitions. This is another non-trivial cross-check of our implementation of the effective potential in the  $R_\xi$ -gauge.

Since we are interested in estimating the theory uncertainty of the parameters characterizing a FOEWPT arising from their residual gauge-parameter dependence, we need to define a reasonable variation range for the gauge-fixing parameter. The upper bound can be defined by requiring perturbativity, which schematically gives rise to a limit of  $|\xi| \lesssim 1/g \sim 10$ ,<sup>19</sup> while for higher values of the gauge-fixing parameters the perturbative behavior of the loop expansion begins to fail. We have therefore chosen the range  $\xi \in [-10, 10]$  for the Fermi and *background*  $R_\xi$  gauges and  $\xi \in [0, 10]$  for the *standard*  $R_\xi$  gauge (see the discussion below).

To begin, we show the gauge variation of  $T_c$  for different loop orders of the effective potential in the 3D approach with the  $\mathcal{O}(g^4)$  matching accuracy (see Section 3.4 for details) in Fig. 8. The solid lines indicate the predictions for  $\xi = 0$ , which corresponds to the Landau gauge, and the shaded uncertainty bands show the variation of  $T_c$  when varying  $\xi$  between -10 and 10. The result for the tree-level potential (green) is only visible as a solid line because it does not depend on  $\xi$ . We find that the gauge dependence is reduced by more than a factor of three when considering the two-loop effective potential (blue) in comparison to the

---

<sup>19</sup>It was shown in Ref. [109] that taking larger values of the gauge-fixing parameter can also lead to spurious Landau poles.

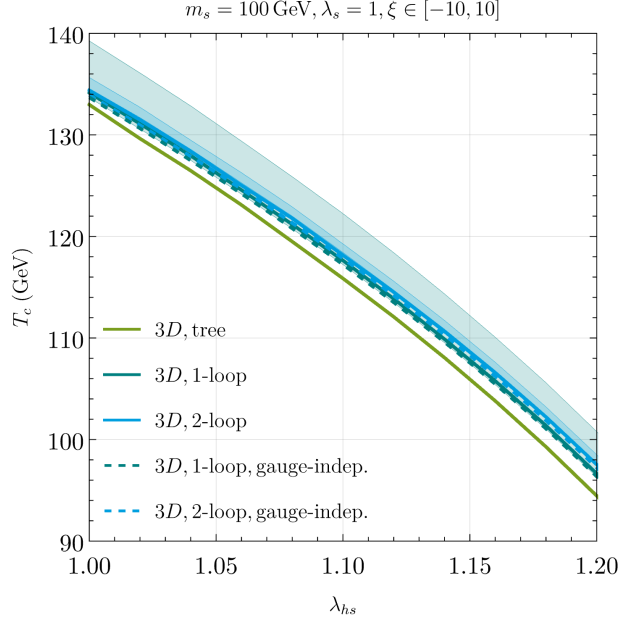


**Figure 8:** Critical temperature  $T_c$  determined for  $m_s = 100$  GeV,  $\lambda_s = 1$ ,  $\lambda_{hs} \in [1, 1.2]$  for different loop orders within the  $3D$  approach. The bands represent variations of the gauge-fixing parameter  $\xi \in [-10, 10]$  in  $R_\xi$ -gauge. Dashed lines represent the gauge-independent determination of  $T_c$  in the  $\hbar$ -expansion.

one-loop potential (teal). The reduction of the theory uncertainty from the residual gauge dependence strongly resembles the reduction of the scale-dependence when including higher loop orders of the effective potential as shown in Fig. 7. One can explain this behavior via the Nielsen identity shown in Eq. (3.10). For the gauge-dependent results shown in Fig. 8, we determine the  $n$ -loop minimum  $v^{(n)} = v_0 + v_1 + \dots + v_n$  of the potential via direct minimization of the  $n$ -loop potential, *i.e.*

$$\frac{\partial}{\partial \phi} (V_0 + V_1 + \dots + V_n)|_{v^{(n)}} = 0. \quad (4.9)$$

Now, we insert this into the Nielsen identity for the all-order potential

$$\xi \frac{\partial}{\partial \xi} (V_0 + V_1 + \dots) \Big|_{v^{(n)}} = C(\phi, \xi) \frac{\partial}{\partial \phi} (V_{n+1} + V_{n+2} + \dots) \Big|_{v^{(n)}}. \quad (4.10)$$

Rearranging terms, we find for the order of the gauge dependence of the  $n$ -loop potential:

$$\xi \frac{\partial}{\partial \xi} (V_0 + V_1 + \dots + V_n) \Big|_{v^{(n)}} = \left( C(\phi, \xi) \frac{\partial}{\partial \phi} - \frac{\partial}{\partial \xi} \right) (V_{n+1} + V_{n+2} + \dots) \Big|_{v^{(n)}} = \mathcal{O}(\hbar^{n+1}). \quad (4.11)$$

Thus, the residual gauge dependence of the effective potential is of the order of  $\hbar^{n+1}$ , *i.e.* the order of the missing higher-order terms in the potential. As a consequence, the predictions for thermodynamic quantities like  $T_c$  have a reduced residual gauge dependence with increasing loop order that is visible for our results shown in Fig. 8.

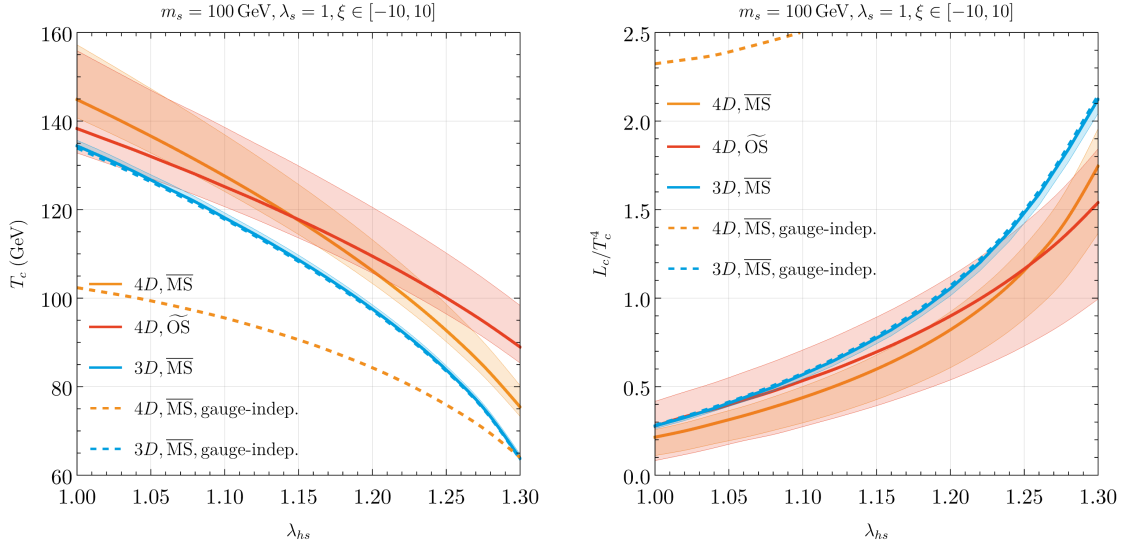


**Figure 9:** Critical temperature (*left*) and latent heat (*right*) determined for  $m_s = 100 \text{ GeV}$ ,  $\lambda_s = 1$ ,  $\lambda_{hs} \in [1, 1.3]$ . The bands represent variations of the gauge-fixing parameter  $\xi \in [-10, 10]$  in  $R_\xi$ -gauge. Dashed lines represent the gauge-independent approach based on the expansion around the tree-level minimum.

We have discussed in Section 3.1 how a gauge-independent prediction for the critical temperature can be achieved by applying the  $\hbar$ -expansion. We indicate the predictions for  $T_c$  using the  $\hbar$ -expansion considering the different loop orders with the dashed lines in Fig. 8. Both at one- and two-loop order, we find that the gauge-independent  $\hbar$ -expansion results lie within the shaded uncertainty bands and are thus captured by the gauge variation in the direct minimization procedure. We also find that the gauge-independent predictions lie close to the Landau-gauge results which are shown with the solid lines.

Next, we compare the different approaches defined at the beginning of this section ( $4D\text{-}\overline{\text{MS}}$ ;  $4D\text{-}\widetilde{\text{OS}}$ ;  $3D\text{-}\overline{\text{MS}}$  at two-loop level with  $\mathcal{O}(g^4)$  matching) in terms of the numerical impact of the residual gauge-dependence on the predictions for the critical temperature  $T_c$  and the latent heat  $L_c$ . This is depicted in Fig. 9 for  $T_c$  (*left* plot) and  $L_c$  (*right* plot), with the solid lines showing the result for  $\xi = 0$ , and the shaded bands indicate the theoretical uncertainty from the  $\xi$ -variation as discussed above. Moreover, the dashed lines show the predictions for the manifestly gauge-independent calculation, as determined using the  $\hbar$ -expansion about the tree-level minima of the effective potential (Eq. (3.19)). As already visible in Fig. 8, we find good agreement between the gauge-independent results and the gauge-dependent results based on the direct potential minimization in the  $3D$  case (blue). On the contrary, there is a significant deviation between the gauge-independent results based on the  $\hbar$ -expansion and the ones from direct numerical minimization of the loop-corrected potential in the  $4D$  approach, irrespective of whether the  $\overline{\text{MS}}$ - or the  $\widetilde{\text{OS}}$ -prescription is used. The gauge-independent predictions for  $T_c$  deviate by more than 50% is applied, and the gauge-independent predictions for  $L_c/T_c^4 \sim 2.5\text{--}4$  deviate by a factor of a few across the parameter space shown on the plot. The main culprit for these huge discrepancies in

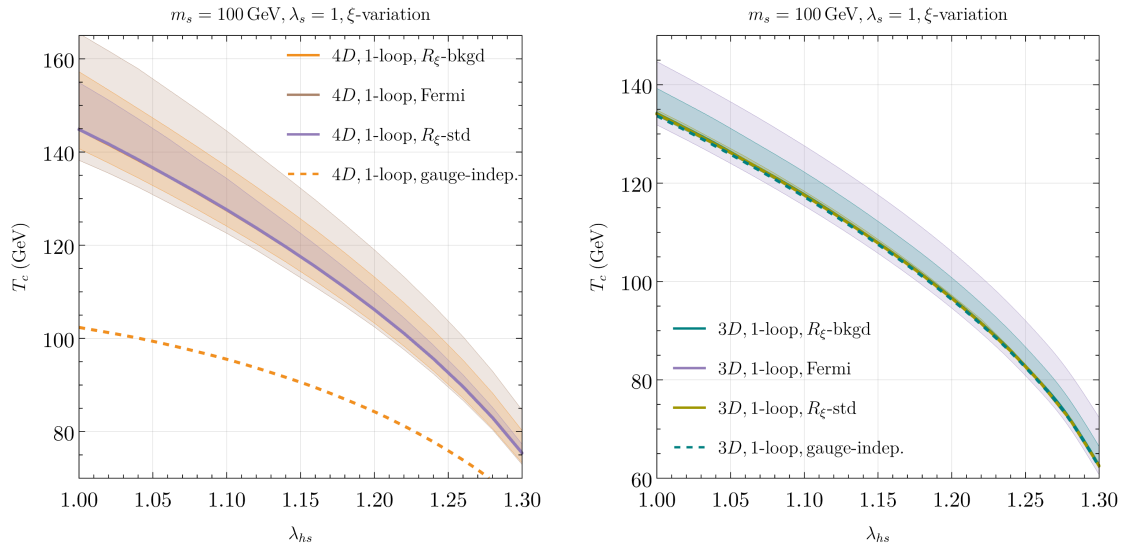


**Figure 10:** Gauge-parameter induced variation of the critical temperature for Fermi, *standard* and *background*  $R_\xi$ -gauges (see Section 3.1 for definitions). The *left* panel shows  $T_c$  determined by minimizing the  $4D$  effective potential with daisy resummations and input parameters determined in the  $\overline{\text{MS}}$ -scheme. The *right* panel shows  $T_c$  in different gauges within the  $3D$ - $\overline{\text{MS}}$  approach at one-loop order. For the *background*  $R_\xi$  and Fermi gauges, the  $\xi \in [-10, 10]$  variation is shown. In the *standard*  $R_\xi$ -gauge,  $\phi^{GF}$  is set to the tree-level minimum  $v_{h,0}$ , and the gauge-fixing parameter is varied within  $\xi \in [0, 10]$ . The solid and dashed lines correspond to results obtained in the Landau gauge and using a gauge-independent approach via the  $\hbar$ -expansion, respectively.

the  $4D$  approaches lies in the fact that the tree-level minimum is significantly shifted by leading thermal loop corrections. Furthermore, in the  $4D$  approach, the method to extract gauge-independent daisy resummation contributions, following Ref. [73], is somewhat *ad hoc*, relying on evaluating different parts of the potential at different minima values. Taking into account the observations from the discussion of the renormalization scale dependence in Section 3.2, our results suggest that the inherent theoretical uncertainties of the  $4D$  approach at the one-loop level are neither captured by a scale variation about a factor of two, nor by the rather large  $\xi$  variation that we have applied here. On the contrary, the proximity of the gauge-independent and the Landau gauge result in the  $3D$  approach once again indicates a good perturbative behavior of the effective potential.

We proceed by exploring differences in the choice of the gauge-fixing condition. A comparison between the critical temperature determined by direct minimization of the effective potential in the Fermi, *background*  $R_\xi$  and *standard*  $R_\xi$  gauges, defined in Section 3.1, is presented in Fig. 10 for the  $4D$ - $\overline{\text{MS}}$  (left plot) and  $3D$ - $\overline{\text{MS}}$  (right plot) approaches. For a better comparison between the  $3D$  and the  $4D$  approaches, we use here the one-loop effective potential in the  $3D$  approach which is at the same loop order as the effective potential in the  $4D$  approach. For the *background*  $R_\xi$  and Fermi gauges, we show uncertainty bands using a  $\xi$ -variation in the range  $\xi \in [-10, 10]$ . In the *standard*  $R_\xi$ -gauge,  $\phi^{GF}$  is

set to the tree-level minimum  $v_{h,0}$ , and the gauge-fixing parameter is varied using only positive values of  $\xi$  within the range  $\xi \in [0, 10]$ , see the discussion below. The variation of the gauge-fixing parameter  $\xi \in [-10, 10]$  in Fermi gauge results in a larger uncertainty in the  $T_c$ -determination in both the  $4D$  and  $3D$  approaches as compared to the *background*  $R_\xi$ -gauge, but the qualitative results are similar. However, we find that positive  $\xi$  values give rise to lower critical temperatures in Fermi gauge, while the opposite is true in the  $R_\xi$ -gauges.

For the *standard*  $R_\xi$ -gauge, we use  $\phi^{GF} = v_{h,0}$  in the gauge-fixing condition, thus assigning the local EW symmetry-breaking minimum with positive value of  $v_{h,0}$  as the physical minimum. This gauge fixing explicitly breaks the  $\phi_h \rightarrow -\phi_h$  symmetry of the effective potential, which is preserved in the other gauges. As a consequence, in the standard  $R_\xi$ -gauge the two EW symmetry breaking minima at  $+v_h$  and at  $-v_h$  are not degenerate anymore, whereas their degeneracy is preserved in the other gauges. For negative  $\xi$ -values, we find that the minimum at  $\phi_s = 0$  and  $\phi_h < 0$  becomes the global minimum at low temperatures. By tracing the different phases of the potential at finite temperature and computing the probabilities for a FOEWPT from the vacuum with  $(v_s \neq 0, v_h = 0)$  into the vacua with  $(v_s = 0, v_h \neq 0)$ , one finds that the transition rates are larger for a transition into the vacuum corresponding to the global minimum with  $v_h < 0$ . However, this contradicts the choice of setting  $\phi^{GF} = v_{h,0} > 0$  in the gauge-fixing conditions, as discussed above. Due to this inconsistency in the standard  $R_\xi$ -gauge, we discard these points with negative  $\xi$ -values as unphysical, and limit the variation of the gauge-fixing parameter in this gauge to positive values  $\xi \in [0, 10]$  where the minimum with  $v_h > 0$  is the global minimum of the potential at  $T = 0$ .<sup>20</sup> We have verified that upon performing an  $\hbar$ -expansion in the *standard*  $R_\xi$ -gauge, we obtain gauge-independent results that agree with the results from other gauges after an  $\hbar$ -expansion.

The results for the gauge-independent determination of  $T_c$  via an  $\hbar$ -expansion are shown by dashed lines in Fig. 10. As a consequence of the  $\hbar$ -expansion, the results are independent of both the gauge-fixing parameter and the gauge-fixing condition. As already discussed above, the application of the  $\hbar$ -expansion in the  $3D$  EFT gives rise to a result that lies within the uncertainty bands from the  $\xi$ -variation using the gauge-dependent numerical minimization of the loop potential. Hence, the  $3D$  approach complemented with the  $\hbar$ -expansion provides a numerically precise and gauge-independent prediction for the critical temperature. On the contrary, in the  $4D$  approach the application of the  $\hbar$ -expansion at one-loop level gives rise to a result that is gauge-independent but shows large deviations from the results using the direct minimization of the loop potential, and only the gauge-dependent results (without  $\hbar$ -expansion) are in agreement with the predictions of the  $3D$  EFT.

Interestingly, we find that the loop corrections in some gauge-fixing setups can qualitatively change the vacuum structure depicted in Fig. 1. For large  $\xi$ -values, the high temperature phase can develop a small non-zero value  $v_h$  of the Higgs condensate at the minimum

---

<sup>20</sup>Since  $\xi = 0$  is the lower limit of the  $\xi$ -variation in the standard  $R_\xi$ -gauge, the solid lines indicating the predictions in the Landau gauge coincide with the lower edge of the uncertainty bands of the standard  $R_\xi$ -gauge.

in addition to a non-vanishing singlet vev  $v_s$ . This is analogous to the EW symmetry non-restoration at high temperature, a phenomenon that recently gained interest [27, 44, 110–114]. For instance, in the *background*  $R_\xi$  gauge, for  $\lambda_{hs} = \lambda_s = 1, m_s = 100 \text{ GeV}$  at  $T = T_c$ , this happens for  $\xi \gtrsim 7$  in the  $4D\text{-}\overline{\text{MS}}$  approach. We find non-vanishing Higgs vevs in the high- $T$  phase, both in  $R_\xi$  and Fermi gauges, while the vacuum structure with  $v_h = 0$  in the high- $T$  phase is preserved in the Landau gauge. In addition, the high-temperature phase does not develop a vev for the Higgs field if the  $\hbar$ -expansion is performed. Hence, we regard the occurrence of non-vanishing Higgs vevs in the high- $T$  phase as an unphysical artifact of the direct minimization of the effective potential that can arise in certain gauges if the vacuum structure of the potential is not analyzed in a strictly gauge-independent way.

## 4.2 Nucleation thermodynamics

As a next step towards predictions for GW signals from cosmological phase transitions we now study the dynamics of the associated bubble nucleation processes that induce the onset of the phase transition. One important quantity in this context is the nucleation rate at non-zero temperatures  $\Gamma(T)$ , which describes the probability per unit time and unit volume that a bubble of a new phase will nucleate. It is the defining quantity for the temperatures at which bubble nucleation and percolation takes place, which for the EW phase transition can be regarded as the temperatures for the on-set and the completion of the phase transition, respectively. The nucleation rate in the semi-classical approximation is given by [5, 115, 116]

$$\Gamma(T) \approx A e^{-S_B/T}, \quad (4.12)$$

where the prefactor  $A = A_{\text{stat}} A_{\text{dyn}}$  contains statistical  $A_{\text{stat}} \approx T^3 (S_B/2\pi T)^{3/2}$  and dynamical components  $A_{\text{dyn}} \approx T$ , which capture equilibrium and non-equilibrium effects, respectively [117]. The bounce action  $S_B$  is the Euclidean action evaluated at the bounce solution  $\phi_i^B$ ,

$$S_B \equiv S[\phi_i^B] = 4\pi \int_0^\infty d\rho \rho^2 \left[ \frac{1}{2} \left( \frac{d\phi_i^B(\rho)}{d\rho} \right)^2 + V_0(\phi_i^B(\rho)) \right], \quad (4.13)$$

where  $\phi_i^B$  are the field profiles that solve the equations of motion subject to specific boundary conditions, corresponding to the  $O(3)$  symmetric profile of the bubble of the *true* vacuum in the space of *false* vacuum configurations,

$$\frac{d^2\phi}{d\rho^2} + \frac{2}{\rho} \frac{d\phi}{d\rho} - \nabla_\phi V_0(\phi) = 0, \quad \text{with } \phi^B(\infty) = \phi_{\text{false}}, \quad \left. \frac{d\phi^B}{d\rho} \right|_{\rho=0} = 0. \quad (4.14)$$

Loop corrections of higher order to Eq. (4.12) arise from fluctuations around the bounce profile of Eq. (4.14). At one-loop level, they would appear as a functional determinant prefactor [116]. They are formally of higher order, but can be compatible in size to the leading order bounce action [99, 118, 119].

A complication arises from the fact that the phase transition is induced by thermal fluctuations, which themselves are loop effects. Hence, the lowest order bounce action, as

defined in Eq. (4.13), often does not exist. A common solution is to calculate the bounce action of Eq. (4.13) by replacing the tree-level potential with the effective potential,  $V_0 \rightarrow V$  [116, 120], which includes radiative corrections by construction.<sup>21</sup> This simple replacement is what is usually carried out in the  $4D$  approach in order to account for radiative corrections. However, it does not correspond to a proper perturbative expansion of the bounce action, as higher-loop corrections to other terms in the derivative expansion (similar to Eq. (3.3)) could be just as important [121–123]. Another drawback is that the effective potential calculation relies on the homogeneity of the background field, which is not the case for the bounce configuration. It also leads to the double-counting of fluctuations, in both the calculation of the effective potential and in the prefactor to the bounce. Moreover, the nucleation rate calculated in this ad hoc approach is gauge-dependent, as a remnant of the gauge dependence of the effective potential at non-stationary points. Nevertheless, in many cases, the dominant contributions to the action arise from the leading thermal corrections already captured by the effective potential, making this approach a reasonable first approximation if more rigorous methods are computationally too expensive. Consequently, despite the issues raised above, this method remains widely used, as it often provides a qualitatively reliable estimate of the phase transition dynamics, and it is often sufficient for identifying parameter regions where a strong FOEWPT occurs (see Section 5).

A theoretically consistent treatment of the bounce action that includes radiative and thermal corrections can be achieved in a high-temperature EFT by integrating out the leading thermal fluctuations, absorbing them into an effective leading-order bounce action [99, 124, 125]. Then, loop corrections to the bounce action within the EFT can be systematically accounted for [119]. The loop-improved nucleation action derived in this way is gauge-independent, as it is defined by the solution of the tree-level bounce equation of motion [90, 92, 126]. As mentioned above, adding a complete set of one-loop corrections to the bounce action would require the computation of the functional determinant of the fluctuations around the bounce configuration, which goes beyond the scope of this work.

The dynamics of bubble nucleation implies that the nucleation temperature  $T_n$  and the percolation temperature  $T_p$  [127] are important quantities in this context. The former is defined as the temperature at which the probability of a single bubble nucleating in a Hubble volume becomes significant,

$$\int_{t(T_c)}^{t(T_n)} dt \frac{\Gamma(t)}{H(t)^3} = \int_{T_n}^{T_c} \frac{dT}{T} \frac{\Gamma(T)}{H(T)^4} \approx 1, \quad (4.15)$$

where  $T_c$  is the critical temperature at which the two minima are degenerate. For the Hubble parameter  $H(T)$ , characterizing the expansion rate of the universe, we can assume that the universe is radiation dominated, such that

$$H(T)^2 = \frac{\rho_{\text{rad}}(T)}{3M_p^2}. \quad (4.16)$$

---

<sup>21</sup>In practice, one only incorporates the real part of the effective potential  $V_0 \rightarrow \text{Re}[V]$ . The presence of a non-vanishing imaginary part again signals the shortcomings of this approach [61, 121].

Here,  $\rho_{\text{rad}}$  is the radiation energy density given by  $\rho_{\text{rad}} = g_* T^4 \pi^2/30$ ,  $M_p = 2.4 \times 10^{18}$  GeV is the reduced Planck mass, and  $g_* = g_*(T)$  is the effective number of relativistic degrees of freedom.

The percolation temperature  $T_p$  is the temperature at which bubbles of the new phase have grown sufficiently to form a connected network that stretches over a significant fraction of the universe [128]. At this point, the phase transition effectively completes, and we expect most of the GW produced during the transition to originate from this moment [129], which occurs when the fraction of the extended volume occupied by the new phase is around 34. The extended volume double counts the overlapping regions of the bubbles, which is removed by exponentiating it [130]. The defining relation for  $T_p$  is

$$\frac{4\pi H(T_p)^3}{3} \int_{T_p}^{T_c} \frac{dT}{T} \frac{\Gamma(T)}{H(T)^4} R(T_p, T)^3 \approx 0.34, \quad (4.17)$$

where  $R(T_p, T) = v_w (1 - T/T_p)/H(T)$  is the radius of a bubble nucleated at  $T$  which expands with the velocity  $v_w$  until  $T_p$  is reached [131]. In our work, we make use of the fact that most of the contributions to the integral shown in Eq. (4.15) come from temperatures near  $T_n$ . This allows one to apply the saddle-point approximation to the integral, and the relevant temperatures  $T_n$  and  $T_p$  can be derived from a simple Taylor expansions of action. Specifically, we use the resulting approximations for  $T_n$  and  $T_p$  as given in Ref. [127], which provides a convenient method for their numerical evaluation. Numerically, we find that the difference between  $T_n$  and  $T_p$  is small within the parameter region of the cxSM under consideration, reaching at most a few GeV.

The duration of the phase transition is characterized by the dimensionless quantity  $\beta/H$ , where  $\beta$  is the time derivative of the nucleation rate at the time when the phase transition becomes significant:

$$\beta = - \left. \frac{d}{dt} \left( \frac{S(t)}{T(t)} \right) \right|_{t=t_p} = H(T) T \left. \frac{d}{dT} \left( \frac{S(T)}{T} \right) \right|_{T=T_p}. \quad (4.18)$$

The ratio  $\beta/H$  measures the rapidity of the phase transition, where large values indicate fast transitions. It is an important parameter for the predictions of the GW signals, entering both the peak frequency and the peak amplitude of the GW spectra, see the discussion in Section 5.1 below.

Another parameter that is relevant for the GW predictions is  $\alpha$ —the ratio of energy density liberated during the phase transition over the radiation energy density of the universe, given by [130]

$$\alpha = \frac{\Delta\theta}{\rho_{\text{rad}}} = \frac{1}{\rho_{\text{rad}}} \left( \Delta V - \frac{1}{4} T \frac{d\Delta V}{dT} \right) \Big|_{T=T_p}. \quad (4.19)$$

As before,  $\Delta$  refers to the difference between high and low temperature phases. Here, we assumed that the energy density released is related to the change of trace anomaly,  $\theta = (\rho - 3p)/4$ , between phases. Conversely, it could be simply taken as the difference of the energy density,  $\rho$ , between two phases. The parameter  $\alpha$  determines the strength of the phase transition, where larger values correspond to stronger transitions.

To calculate the bounce action at the given temperature, we use the public code `CosmoTransitions` [132] to solve the bounce equation shown in Eq. (4.13). The evaluation of the bounce action may suffer from numerical instabilities, which typically arise in the case of relatively weak phase transitions. We find that the determination of  $\beta/H$  is the most sensitive to these numerical instabilities in our calculations, whereas the computation of the characteristic temperatures and of the parameter  $\alpha$  is only marginally affected. Although these numerical instabilities are present in the bounce solution, they are sufficiently small as not to alter our conclusions about the predicted GW spectra discussed below.

The final parameter that is relevant for the prediction of the GW spectra is the bubble wall velocity  $v_w$ , as used already in Eq. (4.17). Its computation requires a real-time simulation of the expanding bubbles in the surrounding plasma. Performing such simulations is a non-trivial and computationally costly task [133] which involves solving coupled equations of motion for scalars and Boltzmann equations for the surrounding plasma [134, 135]. Explicit results have been obtained for the SM [136], singlet extensions of the SM [137–139], and extensions of the SM by a second SU(2) Higgs doublet [134, 139–141]. Nevertheless, there are still large uncertainties [142], and the predictions for  $v_w$  based on different approaches do not always agree. Moreover, higher-loop corrections to  $v_w$  have been accessed recently [143] and were found to decrease the wall velocity in a model with a real scalar singlet field, and contributions from additional friction terms beyond  $1 \rightarrow 1$  particle transmissions have been shown to be missing in the kinetic approach to compute  $v_w$  [144]. Taking these uncertainties into account, for the computation of GW signals in realistic BSM theories the bubble wall velocity is often treated as a free input parameter (for instance, see [28]), or kept fixed at  $v_w = 1$ . We leave a study of uncertainties in the description of the GW signals related to the imprecise knowledge of the bubble wall velocity for future studies and instead focus on the impact of other sources of theory uncertainty related to the perturbative description of the phase transition. Hence, for simplicity, we assume that the expanding bubbles reach a terminal velocity of  $v_w = 1$ . This choice is supported by recent results from real-time lattice simulations, which show a ultra-relativistic detonation solution with  $v_w \approx 1$  for SFOEWPT (with GW signals potentially in reach of LISA) for which prior computations using analytic methods based on a steady-state expansion of the bubble predicted substantially smaller sub-sonic bubble walls [138, 145].

Similarly to Section 4.1, we compare the different approaches for computing the parameters characterizing the thermodynamics of bubble nucleation and the onset of the SFOEWPTs. In particular, we are interested in the renormalization scale dependence and the gauge dependence in the predictions for the parameters  $T_p$ ,  $\beta/H$  and  $\alpha$ , in comparing the  $4D$  approaches and the dimensionally reduced  $3D$  EFT. In the  $4D$  approach, we substitute  $V_0 \rightarrow V^{4D}$  of Eq. (4.2) in the bounce equation, Eqs. (4.13) and (4.14), to compute  $S_B$  in the temperature range in which the false and the true vacua coexist. In the  $3D$  approach, we calculate the nucleation rates (and observables which depend on those) by solving the bounce equation at leading order. In addition, by substituting the loop-improved potential of Eq. (4.3) in the bounce determination,  $V_0 \rightarrow V^{3D}$ , we estimate the impact of higher-order corrections.

In Fig. 11, we illustrate the renormalization scale dependence of the percolation tem-

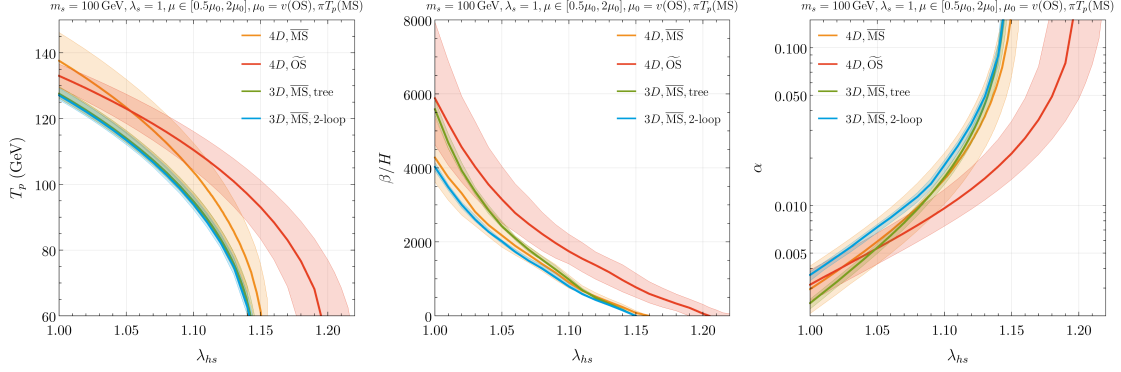


**Figure 11:** Scale-dependence of the percolation temperature  $T_p$  (*left*), phase transition duration  $\beta/H$  (*center*) and strength  $\alpha$  (*right*) determined for  $m_s = 100$  GeV,  $\lambda_s = 1$ ,  $\lambda_{hs} \in [1, 1.2]$  by direct potential minimization in the Landau gauge. The bands represent the renormalization scale variation around the central values at  $\mu = \pi T$  for the  $\overline{\text{MS}}$  and  $\mu = v$  for the  $\widetilde{\text{OS}}$  renormalization schemes, respectively. For the  $3D$  approach, the variance of the matching scale is shown.

perature  $T_p$  (left plot), the inverse of the duration of the phase transition  $\beta/H$  (middle plot) and the strength of the phase transition  $\alpha$  (right plot) calculated within the different approaches. As for the critical temperature, the scale dependence is considerably reduced in the  $3D$  approach (blue) as compared to the  $4D$  ones ( $4D\text{-}\overline{\text{MS}}$  in orange and  $4D\text{-}\widetilde{\text{OS}}$  in red) for all three parameters. We also observe that the  $4D\text{-}\overline{\text{MS}}$  prediction aligns more closely with the  $3D\text{-}\overline{\text{MS}}$  prediction, while the  $4D\text{-}\widetilde{\text{OS}}$  approach predicts larger values of  $T_p$  (and consequently smaller values of  $\alpha$ ) for the largest values of  $\lambda_{hs}$ . Here, one should take into account the different choices for the central values  $\mu_0$  in the  $\overline{\text{MS}}$ - and the  $\widetilde{\text{OS}}$ -schemes, as discussed already in Section 4.1.1. For the  $3D$  approach, we show both results using the tree-level (green) and the loop-improved (blue) potential in the computation of the bounce action. The predictions using the loop-improved potential agree very well with the ones using the tree-level potential. This confirms that the loop corrections do not lead to a significant shift in the predictions for the parameters characterizing the phase transition, even though we note that using the loop-corrected potential in Eq. (4.13) is not a fully consistent loop improvement of the bounce action.

Next, we analyze the gauge dependence of  $T_p$ ,  $\beta/H$  and  $\alpha$ , which is shown in Fig. 12. The results are similar to the ones we observed for the scale dependence, with the  $3D$  EFT result exhibiting a substantially smaller gauge dependence in all three parameters. One can therefore expect that the predictions for the GW signals will be significantly less affected by theoretical uncertainties in the dimensionally reduced EFT compared to the  $4D$  approaches. In particular, the  $4D\text{-}\widetilde{\text{OS}}$  approach exhibits a notably larger dependence on the gauge-fixing parameter compared to the  $4D\text{-}\overline{\text{MS}}$  and the  $3D$  approaches. The larger uncertainty from the gauge dependence using the  $\widetilde{\text{OS}}$ -prescription can be attributed to additional uncanceled gauge dependencies in the finite counterterms added to the potential, which are derived from taking derivatives of the one-loop piece of the potential with respect to the fields (see the

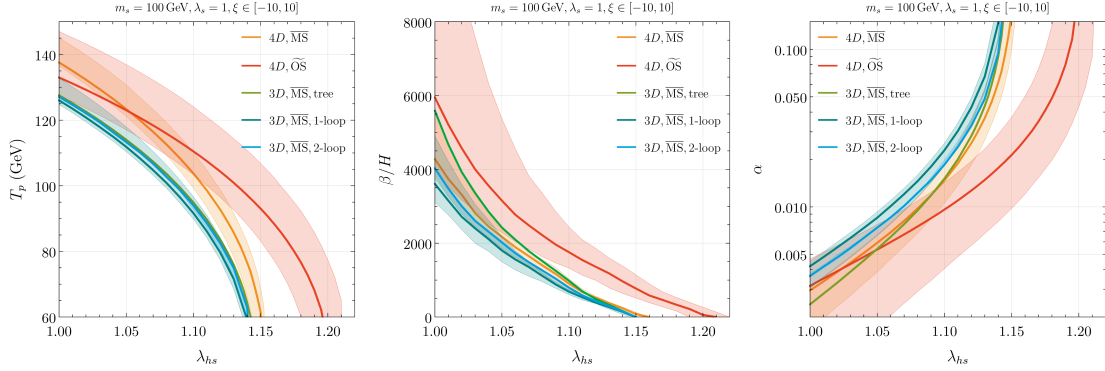


**Figure 12:** Gauge-parameter dependence of the percolation temperature  $T_p$  (*left*), phase transition duration  $\beta/H$  (*center*) and strength  $\alpha$  (*right*) for  $m_s = 100$  GeV,  $\lambda_s = 1$ ,  $\lambda_{hs} \in [1, 1.2]$  in  $R_\xi$ -gauge. The bands indicate the gauge parameter variation of  $\xi \in [-10, 10]$ .

discussion in Section 4.1 and Appendix A). As for the renormalization scale variation, we show (within the 3D EFT approach) results from the tree-level bounce (which are inherently gauge-independent) as well as from the bounce calculation, where the tree-level potential is replaced by the effective potential. This substitution introduces a gauge dependence of the nucleation observables, but we observe that the resulting shifts are of only moderate magnitude. Similar to what we observed in Section 4.1, we observe a gauge dependence reduction when transitioning from the one-loop to the two-loop effective potential.

## 5 Gravitational wave signals

Gravitational waves (GW) produced during a cosmological first-order phase transition might provide a crucial probe of early universe dynamics in the future [146, 147]. Among the primary mechanisms generating these signals, sound waves in the plasma play a dominant role in our model, which does not exhibit strongly supercooled phase transitions, rendering GW production from runaway bubble collisions irrelevant. An additional source of GW production is magnetohydrodynamic turbulence in the plasma. Its contribution to the GW signal in an EW phase transition with weak or intermediate strength of  $\alpha \lesssim 0.1$  (see Fig. 15 below) is subdominant compared to the sound wave contribution [148]. Moreover, the resulting spectral shape of the GW signal caused by the turbulence depends on the fraction of energy converted into turbulent motion in the plasma, which has not yet been determined robustly in numerical simulations and would have to be treated as an additional free parameter [149]. Therefore, we do not include this contribution in our analysis in order to keep the analysis focused on the theory uncertainty resulting from the perturbative description of the SFOEWPT.

## 5.1 Spectral density

The spectral energy density of GWs from sound waves can be approximated as [147, 150, 151]

$$\Omega_{\text{GW}}(f)h^2 \approx \Omega_{\text{GW,peak}}h^2 \left( \frac{f}{f_{\text{peak}}} \right)^3 \left( \frac{7}{4 + 3(f/f_{\text{peak}})^2} \right)^{7/2}, \quad (5.1)$$

where  $f_{\text{peak}}$  is the peak frequency of the GW spectrum today, given by

$$f_{\text{peak}} \approx 26 \mu\text{Hz} \times \left( \frac{1}{H_* R_*} \right) \left( \frac{T_*}{100 \text{ GeV}} \right) \left( \frac{g_*}{100} \right)^{1/6}. \quad (5.2)$$

The peak amplitude of the GW signal today can be approximated by

$$\Omega_{\text{GW,peak}}h^2 \approx 4.1 \times 10^{-7} R_* H_* \left( 1 - \frac{1}{\sqrt{1 + 2\tau_{\text{sw}} H_*}} \right) \times \left( \frac{\kappa_{\text{sw}} \alpha}{1 + \alpha} \right)^2 \left( \frac{100}{g_*} \right)^{1/3}, \quad (5.3)$$

where  $T_*$  is the temperature of the plasma after the phase transition. It is related to the percolation temperature as  $T_* = T_p(1 + \alpha)^{1/4}$  and takes into account reheating effects in the early universe. Given that  $T_* \approx T_p$ , the inverse phase transition duration  $\beta/H$  and strength  $\alpha$  evaluated at the percolation temperature  $T_p$  can be used for computing the GW signals. Moreover,  $\kappa_{\text{sw}}$  is the efficiency factor for the transformation of vacuum energy released during the transition into bulk kinetic energy, which we determine as a function of  $\alpha$  from numerical fits given in Ref. [152]. The mean bubble radius is given by  $R_* H_* \approx (8\pi)^{1/3} (\beta/H)^{-1}$ , assuming  $v_w = 1$  as discussed above, and the sound wave duration is related to the root-mean-square four-velocity of the plasma  $\bar{U}_f$  via  $\tau_{\text{sw}} H_* = R_* H_* / \bar{U}_f$ , with  $\bar{U}_f \approx \sqrt{3\alpha\kappa_{\text{sw}}/4(1 + \alpha)}$  [153].

In the same manner as in the previous sections, we compare different methods for the determination of  $\Omega_{\text{GW}}(f)h^2$  in terms of theory uncertainties from residual scale dependence and gauge dependence. In the left plot of Fig. 13 we show the predicted GW signals using the different approaches introduced in Section 4.1, where the shaded bands indicate the theoretical uncertainty resulting from a variation of the renormalization scale in the  $4D$  approaches and the hard matching scale in the  $3D$  approach. The solid line indicates the prediction for the central scale choices as shown on top of the plots. All results shown are obtained using the Landau gauge, and we show two predictions for the  $3D$ - $\overline{\text{MS}}$  approach using the tree-level effective potential (green) or the two-loop level potential (blue) for the determination of the bounce solution. The differences between these two predictions are found to be within the uncertainty resulting from the scale variation. In line with the observations from Section 4.2, we find that the scale dependence of the predicted GW signals is significantly smaller using the dimensionally reduced EFT compared to the  $4D$  approaches. While the  $4D$ - $\overline{\text{MS}}$  approach predicts a GW signal that within its uncertainties is in agreement with the predictions from the  $3D$  EFT, the  $4D$ - $\widetilde{\text{OS}}$  approach predicts a GW signal with a peak amplitude that is roughly three orders of magnitude smaller, and the peak frequencies differ by roughly an order of magnitude.

The discrepancy between the  $\widetilde{\text{OS}}$  and the  $\overline{\text{MS}}$  results mainly arises from the small parameter shifts between the physical input and Lagrange parameters using  $\widetilde{\text{OS}}$  vs.  $\overline{\text{MS}}$

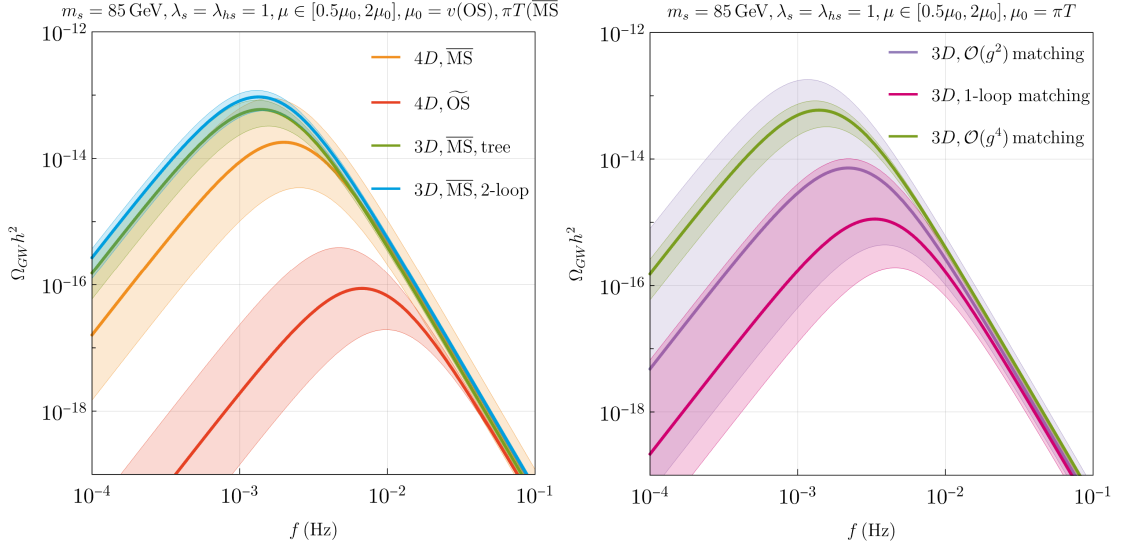


**Figure 13:** Gravitational wave spectrum for  $m_s = 85$  GeV,  $\lambda_s = \lambda_{h_s} = 1$  evaluated in the Landau gauge. The bands indicate the renormalization scale variation around the central value  $\mu = \pi T$  and  $\mu = v$  for the  $\overline{\text{MS}}$  and  $\widetilde{\text{OS}}$  renormalization schemes, respectively. For the  $3D$  approach, the variance of the hard matching scale is shown. In the *left* panel, we compare the  $4D$  and  $3D$  approaches, and the *right* panel shows the predictions for different matching orders in the  $3D$  approach.

relations together with the strong parametric dependence of the gravitational wave spectra (see e.g. Refs. [28, 29]). While this discrepancy between the different renormalization prescriptions appears alarming at the level of individual benchmark points, it is important to note that GW predictions from SFOEWPTs are in many cases extremely sensitive to the underlying model parameters. As a result, when comparing broader regions of parameter space with the goal of identifying regions of parameter space that allow for potentially detectable GW signals, the differences between the approaches are less severe, since the parametric dependence of the GW signal tends to dominate over the scheme-related discrepancies (see Section 5.2 for further discussion).

In the right plot of Fig. 13 we show the relevance of the matching order within the  $3D$  approach. As in the left plot, the shaded uncertainty bands result from a variation of the matching scale, while the solid lines indicate the predictions for the central scale choice, and all results were obtained in the Landau gauge. The purple, magenta and green bands belong to  $\mathcal{O}(g^2)$ , one-loop and  $\mathcal{O}(g^4)$  matching accuracy, respectively. In line with the predictions for  $T_c$  at different matching orders as shown in Fig. 6, we observe a significant reduction of the scale dependence at  $\mathcal{O}(g^4)$  matching accuracy also for the GW signal, whereas a matching at lower accuracy does not improve the theoretical uncertainty from the scale dependence compared to the  $4D$  approach. This once again indicates the importance of the full  $\mathcal{O}(g^4)$  matching in the dimensional reduction approach.

We now turn to the residual gauge dependence in the predictions for the GW signal. Within the  $3D$  approach, the bounce can be determined without the spurious insertion of

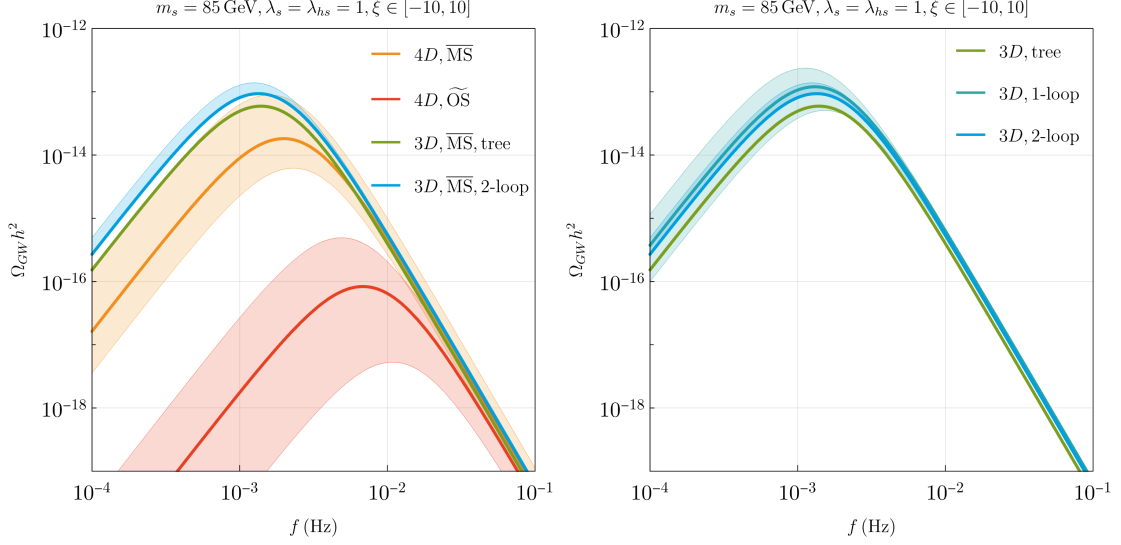


**Figure 14:** Gauge-parameter variation of  $\xi \in [-10, 10]$  in the gravitational wave spectrum for  $m_s = 85$  GeV,  $\lambda_s = \lambda_{h_s} = 1$  in  $R_\xi$ -gauge. In the *left* panel, we compare the  $4D$  and  $3D$  approaches. The *right* panel shows a comparison of including different loop orders of the effective potential in the  $3D$  approach for the bounce calculation.

the loop-improved effective potential by simply using the  $3D$  tree-level potential, which yields inherently gauge-independent results. Nevertheless, we can assess the residual gauge dependence by studying the impact of substituting the loop-improved potential within the dimensionally reduced theory to determine the bounce action and varying the gauge-fixing parameter  $\xi$ . In the left plot of Fig. 14 we show the predictions for the GW signal using the different approaches (the colors are defined as in the left plot of Fig. 13). We here used the background  $R_\xi$ -gauge in all cases, and the shown uncertainty bands arise from a variation of the gauge fixing parameter in the interval  $\xi \in [-10, 10]$ , while the solid lines indicate the predictions in the Landau gauge with  $\xi = 0$ . In a similar fashion to the scale dependence discussed above, also the residual gauge dependence is significantly reduced using the  $3D$  approach compared to the  $4D$  approach. The gauge-dependent  $3D$  result using the two-loop level potential for the computation of the bounce solution is very close to the inherently gauge-independent result using the tree-level potential. The largest theory uncertainty from the residual gauge dependence is again observed for the  $4D$ - $\widetilde{OS}$  approach.

We further scrutinize the residual gauge dependence in the dimensionally reduced EFT by showing in the right plot of Fig. 14 the predicted GW signals using the tree-level (green), one-loop level (teal) and two-loop level (blue) effective potentials for the computation of the bounce solutions. It is interesting to note that only the GW signal predicted using the two-loop level potential shows a very mild gauge dependence, whereas the gauge dependence of the GW signal predicted using the one-loop level potential is substantially more pronounced. Moreover, as already visible in the left plot of Fig. 14, the results using the two-loop level potential are in good agreement with those obtained using the tree-level potential. This comparison demonstrates that the numerical impact of using the two-loop-corrected

potential is small and the induced gauge dependence remains very mild. Therefore, in the following phenomenological discussion in Section 5.2, we use the gauge-independent tree-level potential in the  $3D$  approach, where loop corrections are accounted for in the EFT by integrating out the dominant thermal fluctuations, providing a fully consistent computation of the bounce action.

## 5.2 Peak signal strengths in the $(m_s, \lambda_{hs})$ -plane

In this section, we will identify and analyze more broadly the parameter space regions of the cxSM that can realize a SFOEWPT, and we quantify the theoretical uncertainty of the peak amplitude of the predicted GW signals. As was discussed in Section 2, the cxSM has three independent BSM parameters: the singlet mass  $m_s$ , the singlet self-coupling  $\lambda_s$ , and the portal coupling  $\lambda_{hs}$ . While before we fixed  $m_s$  and  $\lambda_s$  and showed the predictions for the parameters describing the SFOEWPT as a function of  $\lambda_{hs}$ , we now scan parameter planes with varying  $m_s$  and  $\lambda_{hs}$ , while  $\lambda_s = 1$  is kept fixed.

In the left column of Fig. 15, we show the  $(m_s, \lambda_{hs})$  parameter plane for  $\lambda_s = 1$ , and the three different plots correspond to the three different methods employed in the previous sections:  $4D\text{-}\widetilde{\text{OS}}$  (top),  $4D\text{-}\overline{\text{MS}}$  (middle) and  $3D\text{-}\overline{\text{MS}}$  (bottom). The color coding in these plots is as follows: The light-gray region indicates either weak FOEWPTs with  $\Delta v(T_c)/T_c < 0.5$  or no FOEWPT at all. The dark-gray region indicates where the minimum giving rise to the singlet vev is the global minimum through the whole thermal evolution of the universe (down to  $T = 0$ ), such that no EW phase transition can occur. The black region indicates a vacuum trapping [27], where the EW vacuum corresponds to the global minimum at zero temperature, but the conditions for the onset of a FOEWPT are never satisfied during the thermal history, and the universe remains trapped in the false minimum in which only the singlet field has a vev.<sup>22</sup> Finally, the colored region indicates FOEWPTs with  $\Delta v(T_c)/T_c \geq 0.5$ , where the color coding shows the value of the peak amplitude of the GW signal produced during the transition. Comparing the three plots, we find that the overall shape and structure of the regions in parameter space where a FOEWPT is predicted to be very similar for the different approaches. Also, the possible range of the peak amplitudes  $\Omega_{\text{GW,peak}} h^2$  that we find are similar. The fact that the regions of parameter space predicting the strongest FOEWPTs and the corresponding range of peak amplitudes for the GW signal remain very similar across the different approaches, despite the large discrepancies observed at the level of individual parameter points as shown in Fig. 13 and Fig. 14, is as mentioned above a consequence of the strong parametric sensitivity of the GW predictions, which dominates over the scheme-dependent differences if it is projected to parameter space regions of the cxSM.

A common feature across all approaches is that parameter points exhibiting the strongest GW signals lie near the vacuum trapping region (upper left edges of the colored regions). In this region along the diagonal, the peak amplitudes are the largest for lighter singlet masses  $m_s$ , whereas the percolation temperature grows with increasing singlet

<sup>22</sup>Such a region can become viable and feature a FOEWPT once seeded phase transitions from topological defects, such as from domain walls or cosmic strings (e.g. generated when the singlet field obtains a vev [154]) are considered. We do not include this possibility in our discussion.

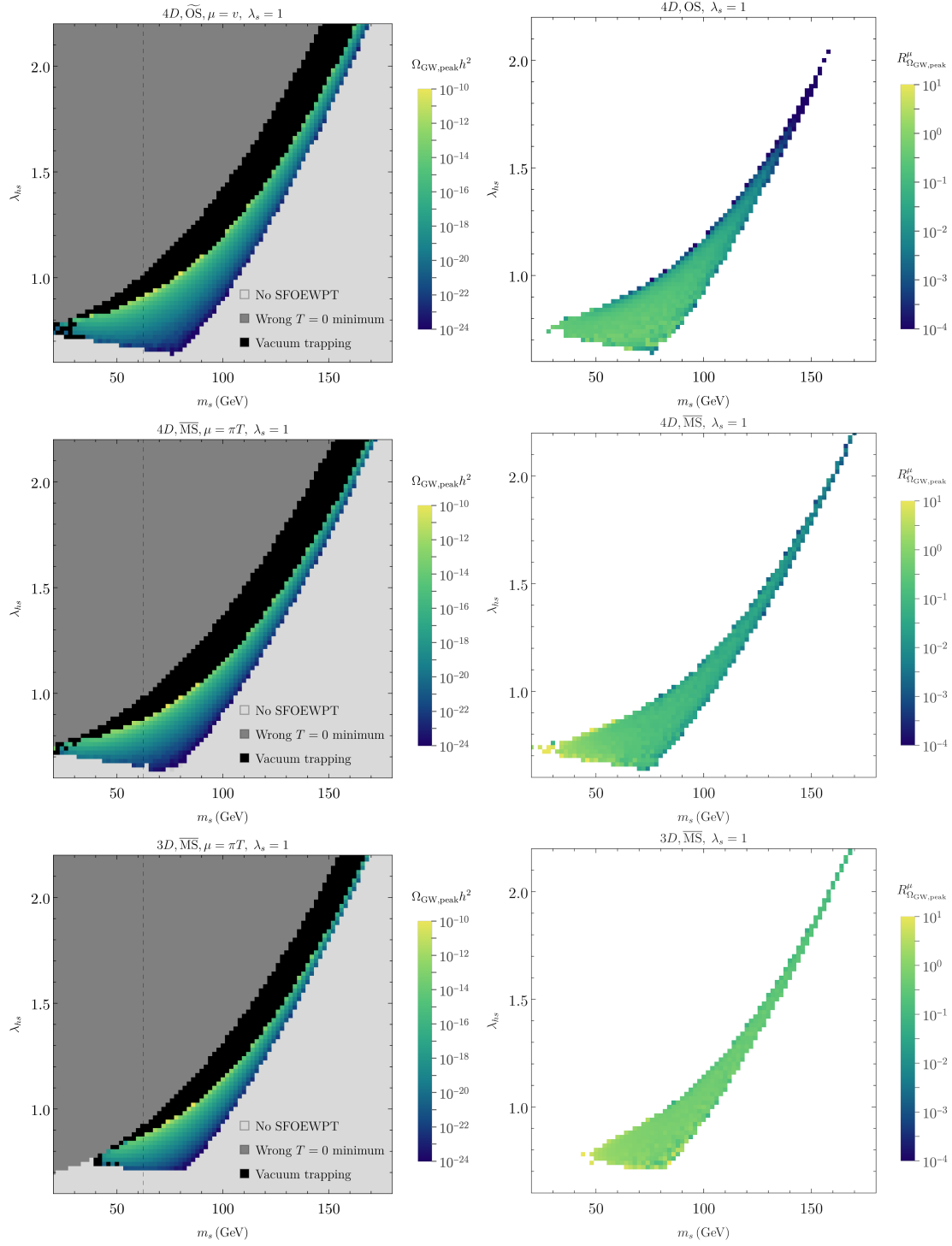


**Figure 15:** Gravitational wave signal peak strength (*left*) and the corresponding scale variation ratio of Eq. (5.4) (*right*) for the  $4D-\overline{\text{MS}}$ ,  $4D-\widetilde{\text{OS}}$  and  $3D-\overline{\text{MS}}$  approaches in the Landau gauge. The dark gray region represents points for which no electroweak phase transition occurs, the light gray region represents points without a *strong* first-order electroweak phase transition (with  $\Delta v(T_c)/T_c < 1/2$ ) and the black region represents points with vacuum trapping. The vertical dashed line at  $m_s = 62.5$  GeV indicates the region where the invisible Higgs decay channel opens.

mass, rendering a weaker signal prediction for larger values of  $m_s$ . This fact can be used to define an upper bound on the singlet mass in the sense that the perturbative description of SFOEWPTs would break down for larger values of  $m_s$ . By requiring that the scalar couplings remain perturbative at the hard scale, we require the four-point vertex contributions to stay below  $4\pi$ . This condition leads to the perturbativity bounds  $\lambda_{hs}(\mu = \pi T) < 8\pi$  and  $\lambda_s(\mu = \pi T) < 8\pi/3$ , which in turn determine the upper limits on the singlet couplings at the input scale  $m_Z$ . Thence, the upper limit on the singlet mass beyond which a SFOEWPT no longer occurs for values of  $\lambda_{hs}$  and  $\lambda_s$  that are sufficiently small is approximately at 500–550 GeV (in agreement with the findings of Ref. [84]).

While for brevity, we show here only parameter planes with  $\lambda_s$  kept fixed, we also investigated the modifications to the parameter regions predicting a SFOEWPT for different values of  $\lambda_s$ . When varying the quartic singlet coupling  $\lambda_s$ , we find qualitatively similar features across all approaches considered. As  $\lambda_s$  increases, with the singlet mass held fixed, the parameter region giving rise to a strong GW signal is shifted toward higher values of  $\lambda_{hs}$ . Conversely, for fixed  $\lambda_{hs}$ , the mass range yielding a strong signal becomes narrower as  $\lambda_s$  decreases. Moreover, we find that the parameter region with a SFOEWPT extends to even larger mass and coupling values beyond the ranges shown in the plots.<sup>23</sup>

We leave a comprehensive phenomenological study of the parameter space regions suitable for GW signals that may be detectable with LISA considering the full three-dimensional parameter space of the cxSM for future work.

After having compared the different approaches for predicting the GW signals against each other, we now want to estimate the theoretical uncertainty of the GW predictions using either of the methods. In order to quantify the scale uncertainties in the predictions for the peak amplitudes of the GW signals, we introduce the ratio

$$R_{\Omega_{\text{GW,peak}}}^\mu = \frac{\Omega_{\text{GW,peak}}(\mu = 2\mu_0)}{\Omega_{\text{GW,peak}}(\mu = \mu_0/2)}, \quad (5.4)$$

where the central value  $\mu_0$  is chosen to be equal to  $v$  for the  $\widetilde{\text{OS}}$ - and to  $\pi T$  for the  $\overline{\text{MS}}$ -scheme. In the right plots of Fig. 15 we show the values of this ratio for the parameter space regions predicting a SFOEWPT (as defined in the left plots) across the different approaches. The regions with colored points do not coincide exactly between the left and the right plot in each row, because the ratio  $R_{\Omega_{\text{GW,peak}}}^\mu$  can only be determined if both scale choices  $\mu = 2\mu_0$  and  $\mu = \mu_0/2$  predict a SFOEWPT. We also note that in the  $3D\text{-}\overline{\text{MS}}$  case, we determine the bounce action using the tree-level potential within the EFT. We have checked that the renormalization scale uncertainty (in this case, due to variation of the matching scale) would remain almost unchanged if the loop improved potential were taken instead. The right plots of Fig. 15 show that, going from top to bottom, *i.e.* from  $4D\text{-}\widetilde{\text{OS}}$  over  $4D\text{-}\overline{\text{MS}}$  to  $3D\text{-}\overline{\text{MS}}$ , the scale dependence of the peak amplitudes of the GW signals are significantly reduced, as already apparent from the previous sections. The scale uncertainties of the  $\Omega_{\text{GW,peak}}$  are most pronounced in the  $4D\text{-}\widetilde{\text{OS}}$  peak regions, especially at the upper left edge

<sup>23</sup>A parameter region with large portal couplings and larger singlet masses was explored in Ref. [72] in a different version of the singlet extension of the SM, where the singlet has a vev at zero temperature and thus mixes with the SM-like Higgs boson.

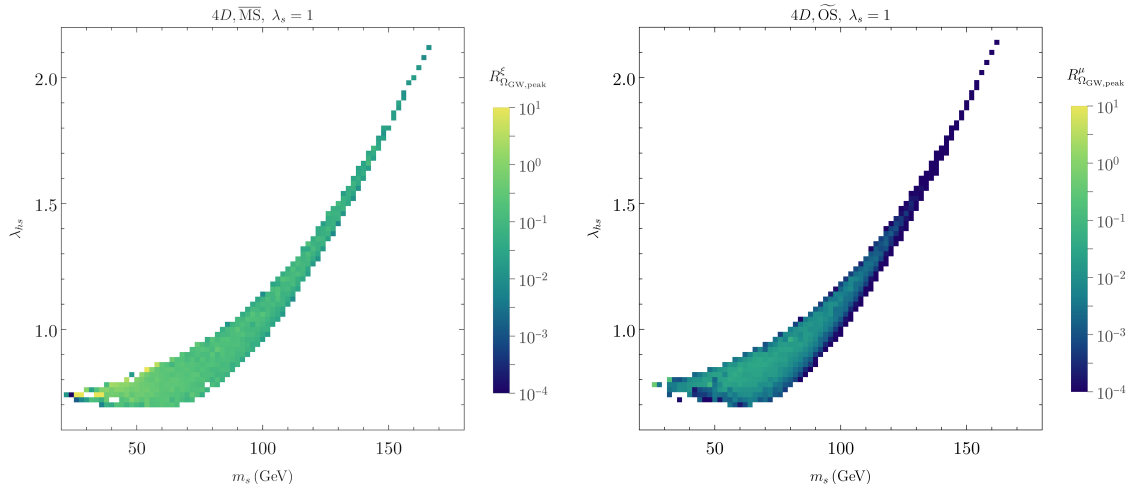


**Figure 16:** Uncertainty in the gravitational wave peak strength due to gauge-fixing parameter variation, quantified by Eq. (5.5), in the  $4D\text{-}\overline{\text{MS}}$  (left) and  $4D\text{-}\widetilde{\text{OS}}$  (right) schemes.

of the region shown where it can be as large as four orders of magnitude. This significant scale dependence in the  $4D\text{-}\widetilde{\text{OS}}$  approach is problematic since it is most severe in parameter space regions where the GW signals could be strong enough for detection by LISA. On the other hand, exploiting the hierarchies between thermal scales and using a dimensional reduction approach leads to a greatly reduced uncertainty in the GW peak amplitude due to the scale variation, which is at most of one order of magnitude as is visible in the bottom right plot of Fig. 15.

Similarly, we assess the shift in the gravitational wave peak signal due to the variation of the gauge-fixing parameter. We do not show the gauge dependence of the  $3D$  approach, because as discussed before, calculating the bounce action using the tree-level potential is the power-counting accurate approach here, and this is inherently gauge-independent. From our checks of individual parameter space points (see *e.g.* Fig. 14), it is clear, though, that the gauge dependence is small in the  $3D$  approach even when including the loop-improved potential. To quantify the impact of residual gauge dependence in the  $4D$  approach, we define for the ratio

$$R_{\Omega_{\text{GW,peak}}}^{\xi} = \frac{\Omega_{\text{GW,peak}}(\xi = 10)}{\Omega_{\text{GW,peak}}(\xi = -10)}. \quad (5.5)$$

In the left plot of Fig. 16 we show with the color coding the values of  $R_{\Omega_{\text{GW,peak}}}^{\xi}$  using the  $4D\text{-}\overline{\text{MS}}$  potential, in the same parameter plane that was already shown in Fig. 15. One can observe that the variation of the gauge-fixing parameter leads to a change in the peak amplitude by approximately one order of magnitude across the entire parameter space giving rise to a SFOEWPT. This can be compared to the results using the  $4D\text{-}\widetilde{\text{OS}}$  approach that is shown in the right plot of Fig. 16. We observe a substantially stronger variation in the  $R_{\Omega_{\text{GW,peak}}}^{\xi}$  values using the  $\widetilde{\text{OS}}$ -scheme, where the variation typically reaches at least two orders of magnitude and can rise to four orders of magnitude in the region predicting the strongest GW signals. As a result, the question of whether a parameter point of the cxSM

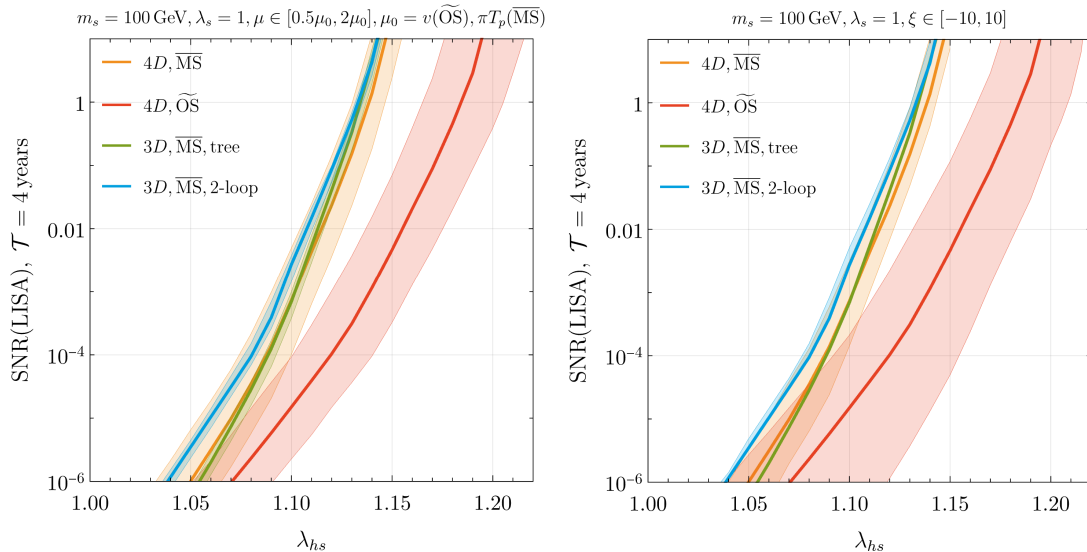


**Figure 17:** Predicted Signal-to-Noise Ratio (SNR) at LISA for  $m_s = 100$  GeV,  $\lambda_s = 1$ ,  $\lambda_{hs} \in [1, 1.2]$  and its renormalization scale (*left*) and gauge (*right*) dependencies.

predicts a GW signal that might be detectable with LISA can be answered less reliably using the  $4D\text{-}\widetilde{\text{OS}}$  approach. In the following, we present a more detailed analysis of the detectability of the GW signals with LISA in terms of the signal-to-noise ratio.

### 5.3 LISA SNR

If the SFOEWPT occurs at temperatures around 100 GeV, the resulting GW signal is expected to fall within the sensitivity range of the LISA interferometer. The detectability of such a signal can be quantified by computing the Signal-to-Noise Ratio (SNR). It can be computed as [147]:

$$\text{SNR} = \sqrt{\mathcal{T} \int_{-\infty}^{\infty} \left( \frac{\Omega_{\text{GW}}(f) h^2}{\Omega_{\text{sens}}(f) h^2} \right)^2 df}, \quad (5.6)$$

where  $\Omega_{\text{sens}}(f) h^2$  is the nominal sensitivity of LISA to GW signals [155], and we assume the duration of the observations to be  $\mathcal{T} = 4$  years. Roughly speaking, if  $\text{SNR} \gtrsim 1$ , the GW signal is classified as detectable.<sup>24</sup>

Figure 17 presents the predicted SNRs at LISA determined using the various approaches discussed in Section 4.1 for the parameter points with  $m_s = 100$  GeV and varying coupling

<sup>24</sup>As mentioned already in Section 1, we do not consider astrophysical foregrounds in our analysis. While we adopt a SNR threshold of 1 to assess detectability, it is worth noting that a threshold of  $\mathcal{O}(10)$  is often used in a Bayesian statistical interpretation of potential signals (see also the discussion in Ref. [155]). The precise choice of the SNR threshold is of minor concern here, as the focus of this work is not on the absolute detectability of a signal, but rather on comparing the SNR predictions obtained from different computational approaches and assessing the associated theoretical uncertainties. As we will show, these uncertainties stemming from the perturbative description of the phase transition reach two orders of magnitude or more, depending on the method used, such that using the condition  $\text{SNR} \gtrsim 10$  instead of 1 would not alter our conclusions.

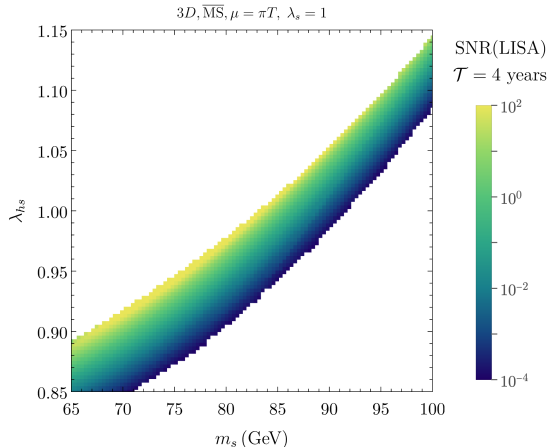


**Figure 18:** The absolute values of the SNR at LISA for  $\lambda_s = 1$  obtained in the  $3D\text{-}\overline{\text{MS}}$  approach. We limit the heatmap scale at  $\text{SNR} = 10^2$  to emphasize variations in lower-SNR regions, and only show points with  $\text{SNR} > 10^{-4}$ .

$\lambda_{hs}$  already discussed in Section 4.2. The colors represent the different approaches as in Fig. 11, and their theory uncertainties from the residual scale dependence (left plot) and gauge dependence (right plot) are indicated with the colored bands (see the discussion in Section 4.2). We observe that the theory uncertainties are greatly reduced using the  $3D\text{-}\overline{\text{MS}}$  approach compared to the  $4D$  approaches. Focusing on the  $4D$ -approaches, we observe that the  $4D\text{-}\widetilde{\text{OS}}$  approach shows a more pronounced uncertainty from both the scale- and the gauge-dependence compared to the  $4D\text{-}\overline{\text{MS}}$  approach. Moreover, we observe an overall shift between the predicted SNRs from the approaches using the  $\overline{\text{MS}}$ -scheme and the  $4D\text{-}\widetilde{\text{OS}}$  approach. The shift between the two results can be attributed to the different choices of central renormalization/matching scales ( $\mu = \pi T$  in the  $\overline{\text{MS}}$ -scheme and  $\mu = v$  in the  $\widetilde{\text{OS}}$ -scheme), differences in the RGE running of the parameters, and missing momentum-dependent contributions in the  $\widetilde{\text{OS}}$ -scheme in the relations to the physical parameters (see Appendix A), as was discussed in more detail in relation to the differences in the prediction for the critical temperature  $T_c$  in Section 4.1.1. This shift is so large that the uncertainty band of the  $4D\text{-}\widetilde{\text{OS}}$  approach does not overlap with the results from the  $4D\text{-}\overline{\text{MS}}$  approach in most parts of the displayed range of the coupling  $\lambda_{hs}$ , potentially indicating a poor behavior of the perturbative expansion at the considered one-loop level.

In Fig. 18 we show the SNR values at LISA for  $\lambda_s = 1$  computed using the  $3D\text{-}\overline{\text{MS}}$  approach in the  $(m_s, \lambda_{hs})$  plane. Compared to Fig. 15 and Fig. 16, the ranges for the singlet mass and the portal coupling in Fig. 17 are reduced to zoom into the region where high SNR values are predicted, and we only show the points predicting a GW signal with  $\text{SNR} > 10^{-4}$ . Despite the sizable theoretical uncertainties in the predicted SNRs across the different approaches, see the discussion above, the regions of the parameter space yielding  $\text{SNR} > 1$  remain similar as a result of the extreme sensitivity of the strength of the GW signals on the model parameters  $m_s$ ,  $\lambda_s$  and  $\lambda_{hs}$ . Consequently, we display in this plot only the results obtained using the  $3D$  approach. As one can expect already from Fig. 15,

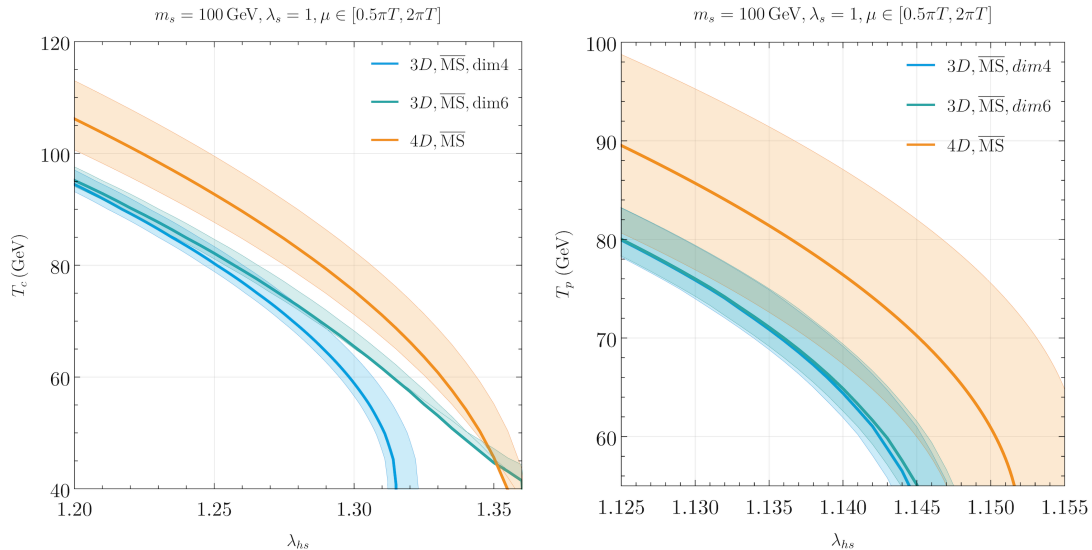


**Figure 19:** Critical (*left*) and percolation (*right*) temperatures determined within the  $4D$  approach in the  $\overline{\text{MS}}$ -scheme as well as in the  $3D$  approach in the  $\overline{\text{MS}}$ -scheme with and without the dimension-6 operators of Eq. (3.30) in the Landau gauge for  $m_s = 100 \text{ GeV}$ ,  $\lambda_s = 1$ . The bands represent the renormalization scale uncertainty, as before. Note that the parameter ranges differ between the two plots.

the parameter region where  $\text{SNR} > 1$  occupies only a rather restricted area in parameter space. Nevertheless, a detection of a GW signal at LISA consistent with a SFOEWPT would not, by itself, allow for a precise reconstruction of the underlying model parameters due to the visible approximate flat direction in the predicted SNRs, where a decrease in the SNR caused by larger singlet masses  $m_s$  can be compensated to a large extent by an increase in the portal coupling  $\lambda_{hs}$ . In particular, this degeneracy implies that the singlet mass cannot be tightly constrained from an experimental observation of a GW signal alone.

## 6 Impact of higher-dimensional operators within the $3D$ approach

An important check for the validity of the dimensional reduction approach is to know to what extent the high-temperature expansion at its core is justified. We investigate this question via the effects of higher-dimensional operators in the EFT Lagrangian (see Section 3.4 for details). Significant effects from these operators on thermodynamic observables and ultimately the GW signal indicate the failure of the truncation of the effective theory, *i.e.* the failure of the high-temperature expansion.

In the left plot of Fig. 19, we show how the inclusion of dimension-six operators in the EFT-Lagrangian (turquoise) changes the predictions for the critical temperature  $T_c$  compared to the ones when truncating the EFT-Lagrangian at dimension four (blue). For comparison, we also show the prediction using the  $4D\text{-}\overline{\text{MS}}$  approach (orange), and in all cases the bands around the solid lines show the theory uncertainty from the scale dependence. The comparison between the turquoise and the blue bands reveals that for higher tempera-

tures adding higher-dimensional operators barely changes the thermodynamic observables, justifying the truncation of the high-temperature EFT Lagrangian in these regions. However, the difference between the turquoise and the blue bands becomes prominent for higher portal couplings, which correspond to lower critical temperatures. This indicates a breakdown of the high-temperature expansion in this regime. Notably, this issue arises precisely where the accuracy of the GW predictions is most critical, since the strength of the signal increases with decreasing transition temperature. We expect the  $4D$  approach at low temperatures to more accurately describe the phase structure, because (apart from the, in this parameter region, small contribution from the AE-type resummation of daisy diagrams) it does not rely on high-temperature expansion. In agreement with this expectation, we observe that adding dimension-six terms to the EFT Lagrangian puts the predicted critical temperature closer to the one obtained within the  $4D$  method for low temperatures.

In the right plot of Fig. 19 we show the predictions for the percolation temperature  $T_p$ , with the definition of the different bands as in the left plot discussed above. In contrast to the critical temperature, the impact of dimension-six operators on the percolation (and nucleation) temperature is significantly less significant, even for the parameter points predicting the lowest values of percolation temperature. A similar behavior was previously observed for phase transitions in the Standard Model Effective Field Theory (SMEFT) [61, 104].

The thermodynamic observable that changes most significantly under the inclusion of the dimension-six operators in the high- $T$  EFT is the phase transition strength  $\alpha$  defined in Eq. (4.19). Figure 20 illustrates the modifications of the phase transition strength (*left* plot) and the peak amplitude of the GW signal (*right* plot), which we respectively quantify in terms of the ratios

$$R_\alpha^{\text{dim6}} = \frac{\alpha[3D, \text{dim6}]}{\alpha[3D, \text{dim4}]} \quad \text{and} \quad R_{\Omega_{\text{GW,peak}}}^{\text{dim6}} = \frac{\Omega_{\text{GW,peak}}[3D, \text{dim6}]}{\Omega_{\text{GW,peak}}[3D, \text{dim4}]} . \quad (6.1)$$

The parameter space region predicting the strongest GW signals corresponds to the region of the lowest percolation temperatures, which in the  $(m_s, \lambda_{hs})$  plane is located at the lower left corner of the banana-shaped band of points predicting a SFOEWPT (see Fig. 15).

The plots of Fig. 20 demonstrate that this is precisely the region where the truncation of the EFT Lagrangian becomes uncertain, as in this region the ratio  $R_\alpha^{\text{dim6}}$  reaches values of about two (yellow points in the left plot). Accordingly, the peak amplitude of the GW signal given in Eq. (5.3), which for  $\alpha \ll 1$  depends approximately quadratically on  $\alpha$ , is also significantly altered. For these points, the inclusion of dimension-six operators give rise to an increase in the peak amplitudes by up to an order of magnitude, as is visible in the right plot of Fig. 20.

We checked that for both the strength  $\alpha$  and the peak amplitude  $\Omega_{\text{GW,peak}}$  the inclusion of dimension-six operators brings the predictions for these observables closer to the ones calculated within the  $4D\text{-}\overline{\text{MS}}$  approach. This observation could be interpreted as a hint that an accurate description of the phase transition just requires the inclusion of higher-dimensional operators beyond the renormalizable ones, instead of an indication of a complete breakdown of the high- $T$  EFT framework. In this view, dimension-six operators act as leading corrections that effectively capture relevant physics missing from the EFT

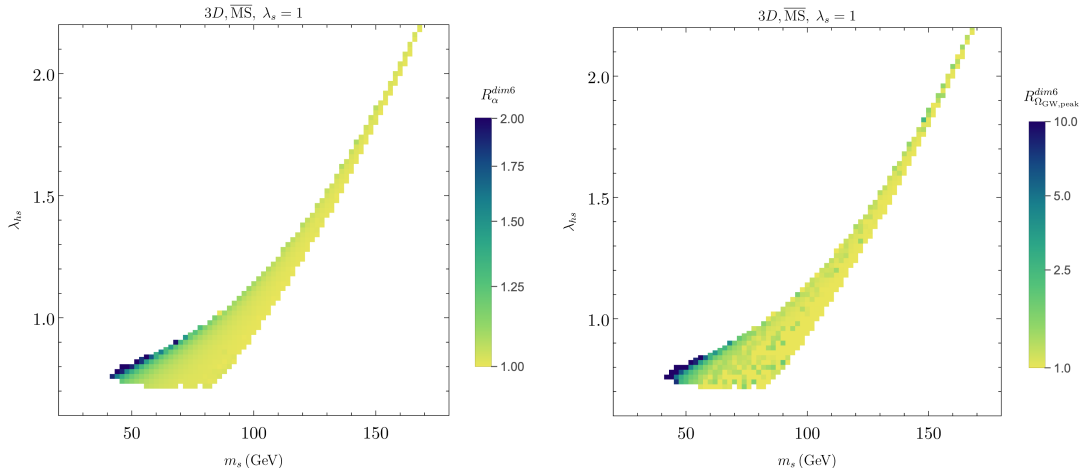


**Figure 20:** Variation ratio of Eq. (6.1) for the phase transition strength  $\alpha(T_p)$  (*left*) and the gravitational wave peak strength  $\Omega_{\text{GW,peak}}$  (*right*) obtained from the inclusion of dimension-6 operators within the  $3D$  approach. Note that the same colors correspond to different ranges in the two plots.

truncated at dimension four. However, without systematically including and assessing the impact of operators of even higher dimension (such as dimension-eight terms), whose effects are expected to be smaller but not necessarily negligible, it is not possible to definitively conclude whether the observed improvement in agreement with the  $4D$ - $\overline{\text{MS}}$  approach genuinely reflects increased predictive power, or instead indicates the onset of the breakdown of the EFT expansion.

## 7 Summary and conclusions

In this work, we have presented a comprehensive study of the dynamics of the EW phase transition and the associated theory uncertainties of the predictions for physical observables characterizing the transitions in the cxSM, the SM extended by a complex gauge singlet scalar field. We focused on a scenario in which SFOEWPTs are realized in such a way that the singlet field has a non-vanishing vev before the transition and a vanishing vev after the transition. This is the simplest realization of a SFOEWPT that, if the singlet mass is larger than twice the Higgs boson mass, is expected to leave no detectable traces at the LHC. In order to investigate the robustness and precision of the perturbative description of the SFOEWPT, we compared a set of commonly used approaches. This set consists of two different input schemes in the  $4D$  approach, the  $\overline{\text{MS}}$ - and the  $\widetilde{\text{OS}}$ -scheme, and of the  $3D$  or high-temperature EFT approach, in which heavy modes are systematically integrated out, leading to an EFT in three spatial dimensions that captures the infrared dynamics of the transition.

We presented an analysis of uncertainty bands arising from both residual scale and gauge dependence, affecting the predictions for thermodynamic observables, such as the critical temperature and latent heat, as well as the predicted GW signals and the corre-

sponding SNRs at LISA. We showed that the uncertainties from the residual scale and gauge dependence are significantly reduced in the  $3D$  approach. Moreover, focusing on the  $4D$  approaches, we found that the gauge-parameter dependence in the  $\widetilde{\text{OS}}$ -scheme is enhanced compared to the one in the  $\overline{\text{MS}}$ -scheme. We showed how with increasing loop order of the effective potential in the  $3D$  approach (up to the full two-loop effective potential in  $R_\xi$  gauge) the gauge dependence and the associated theory uncertainty is reduced order by order, and we discussed in detail how this follows from the gauge-parameter dependence of the effective potential governed by the Nielsen identity.

In both the  $4D$  and the dimensionally reduced  $3D$  frameworks, we obtained gauge-independent results for the quantities characterizing the phase transition and the resulting GW signals by applying the  $\hbar$ -expansion. In the  $4D$  approach, we observed that the gauge-independent results at the considered one-loop level exhibit significant numerical deviations from the gauge-dependent result where one directly minimizes the loop-corrected effective potential, indicating the need for higher-loop corrections to achieve a gauge-independent result with sufficient numerical precision. On the other hand, in the  $3D$  EFT, the gauge-independent results obtained by making use of the  $\hbar$ -expansion are in excellent numerical agreement with those derived from a direct minimization of the loop-corrected potential in a gauge-dependent way. As a result, using the  $\hbar$ -expansion, one-loop  $\overline{\text{MS}}$ -relations between the model parameters, dimensional reduction with NLO matching, integrating out hard and soft scales, and the effective potential at the two-loop level, we achieved a gauge-independent and numerically precise description of SFOEWPTs in the cxSM. As the main remaining theoretical uncertainty in the parameter space regions predicting detectable GW signals at LISA, we identified the impact of higher-dimensional operators in the dimensionally reduced EFT, see the discussion below.

Despite the sizable uncertainties associated to the different approaches used to describe the phase transition dynamics, the parameter regions where SFOEWPTs occur remain similar. This is a result of the large parametric dependence of the transition strengths on the model parameters of the cxSM. While a SFOEWPT can be accommodated over wide parameter regions of the singlet mass and couplings, generating a GW signal that is potentially detectable with LISA, requires a significant amount of fine-tuning among the cxSM parameters  $m_s$ ,  $\lambda_{hs}$  and  $\lambda_s$ . Regarding the occurrence of a SFOEWPT, using the perturbativity limit on scalar couplings, we obtained an upper bound on the singlet mass of  $m_s \lesssim 500\text{--}550$  GeV. For larger masses of the singlet state, the coupling values that would be required to realize a SFOEWPT fall outside of the perturbative regime, such that non-perturbative (lattice) computations would be required to study whether the cxSM allows for a SFOEWPT and an associated GW signal in reach of LISA.

Although the parameter space regions predicting potentially detectable GW signals are largely consistent across the different approaches, within these parameter regions the magnitude of the predicted GW signals can vary by several orders of magnitude, depending on the specific perturbative framework employed. In particular, the  $4D$  approach using the  $\widetilde{\text{OS}}$ -scheme predicts significantly smaller SNRs, typically by about two orders of magnitude, compared to the  $\overline{\text{MS}}$ -scheme. Moreover, the  $4D$ - $\widetilde{\text{OS}}$  approach is subject to considerably larger theoretical uncertainties. A variation of the renormalization scale by a factor of

two can induce changes in the predicted SNRs of up to four orders of magnitude. On the other hand, the  $4D$  approach using the  $\overline{\text{MS}}$ -scheme yields SNRs that are in fairly good agreement with those obtained in the dimensionally reduced  $3D$  approach. The differences between these two approaches are smaller than the intrinsic theoretical uncertainties from the residual scale and gauge dependence associated with the  $4D$ - $\overline{\text{MS}}$  approach, which are at the level of about one order of magnitude. Ultimately, the  $3D$  EFT approach offers the most stable predictions in this regard. When employing NLO matching at  $\mathcal{O}(g^4)$ , the residual scale dependence in the SNRs is reduced by about one order of magnitude. In combination with the fact that the  $3D$  approach can be combined with the  $\hbar$ -expansion to remove residual gauge dependence without discarding numerically important contributions, the application of the high- $T$  EFT is therefore in most parts of the parameter space the most reliable and precise framework to study SFOEWPTs in the cxSM.

However, the  $3D$  EFT approach is subject to an additional intrinsic theory uncertainty from truncating the EFT at finite operator dimension. To assess this uncertainty, we compared results including only renormalizable/dimension-four operators with those also incorporating dimension-six operators. At high temperatures, both types of results agree well, indicating a reliable behavior of the EFT. However, for lower temperatures, particularly below  $T_c \lesssim 80$  GeV, the dimension-six operators noticeably affect the critical temperature and enhance the predicted strength of the phase transition and GW signals. We found that the impact on the critical temperature is more pronounced than on the percolation temperature. Nevertheless, the effects on the GW signals (which are computed at percolation) remain sizable. Specifically, we observed changes in the transition strength  $\alpha$  of up to 100 up to an order of magnitude. Since stronger GW signals correlate with lower transition temperatures, these effects become relevant precisely where the prospects for a GW detection with LISA are best. Interestingly, the inclusion of dimension-six operators brings the predictions of the  $3D$  approach closer to the results obtained using the  $4D$ - $\overline{\text{MS}}$  approach, which may be more reliable in this regime since it relies to a much lesser extent on the high- $T$  expansion. Still, since we included only a subset of all possible dimension-six operators, and since higher-dimensional terms are not considered with which the behavior of the EFT could be further checked, it remains unclear whether this signals a genuine improvement or merely a breakdown of the EFT. We leave a dedicated study in this direction for future work.

In addition to this study of the thermodynamic observables of the cxSM, we also discussed many of the technical details. This includes a demonstration of the cancellation of the scale dependence by including the RGE evolution of the couplings in the  $4D$ - $\overline{\text{MS}}$  approach; the reduction of the scale dependence with increasing matching order in the  $3D$  EFT; a comparison of the results from a direct minimization of the effective potential compared to the gauge-independent results using the  $\hbar$ -expansion, showing good agreement between the two types of results only in the  $3D$  approach; a comparison of different gauge-fixing choices ( $R_\xi$  and Fermi gauges); and the reduction of explicit scale and gauge dependence when including higher loop orders of the effective potential.

## Acknowledgments

We thank Andreas Ekstedt, Guilherme Guedes, Panagiotis Stylianou and Johannes Braaten for useful discussions and comments. A.D., M.L. and G.W. acknowledge the support of the Deutsche Forschungsgemeinschaft (DFG, German Research Association) under Germany’s Excellence Strategy-EXC 2121 “Quantum Universe”-390833306. This work has also been funded by the Deutsche Forschungsgemeinschaft (DFG, German Research Foundation) – 491245950. T.B. acknowledges the support of the Spanish Agencia Estatal de Investigación through the grant “IFT Centro de Excelencia Severo Ochoa CEX2020-001007-S”. The project that gave rise to these results received the support of a fellowship from the “la Caixa” Foundation (ID 100010434). The fellowship code is LCF/BQ/PI24/12040018. A.D. acknowledges the support by Consejería de Universidad, Investigación e Innovación, Gobierno de España and Unión Europea – NextGenerationEU under grant AST2\_6.5.

## A Lagrange parameter input scheme and renormalization

In this section, we provide details about the relations between the physical parameters and those parameters entering the Lagrangian and calculations. Explicit relations are given at the one-loop level. These relations depend on the renormalization scheme used, for which we discuss two options here: the  $\overline{\text{MS}}$ - and  $\widetilde{\text{OS}}$ - prescription.

### A.1 Input parameters

We study the dynamics of electroweak phase transitions using the effective potential, which is defined in terms of the Lagrangian parameters

$$P_{\mathcal{L}} = \{\mu_h^2, \lambda_h, \mu_s^2, g, g', y_t, \lambda_s, \lambda_{hs}\}. \quad (\text{A.1})$$

In order to define a scheme yielding sensible input values for those parameters we use their relation to the following set of input parameters

$$P_{\mathcal{I}} = \{G_F, m_h, m_s, m_Z, m_W, m_t, \lambda_s, \lambda_{hs}\}, \quad (\text{A.2})$$

where  $G_F$  and the physical masses  $m_h, m_s, m_Z, m_W, m_t$  are in principle (i.e., if an appropriate singlet state is detected) directly accessible in measurements. Since for the cxSM there are too few physical masses to determine all parameters of the theory from them, we use the portal coupling  $\lambda_{hs}$  and the quartic coupling  $\lambda_s$  of the singlet as free input parameters.

The tree-level relations for the two parameter sets are

$$g^2 = 4 \frac{m_W^2}{v_h^2}, \quad (\text{A.3a})$$

$$g'^2 = 4 \frac{m_Z^2 - m_W^2}{v_h^2}, \quad (\text{A.3b})$$

$$y_t^2 = 2 \frac{m_t^2}{v_h^2}, \quad (\text{A.3c})$$

$$\mu_h^2 = -\frac{m_h^2}{2}, \quad (\text{A.3d})$$

$$\lambda_h = \frac{m_h^2}{2v_h^2}, \quad (\text{A.3e})$$

$$\mu_s^2 = 2m_s^2 - \frac{v_h^2 \lambda_{hs}}{2}, \quad (\text{A.3f})$$

where

$$v_h^2 = \frac{1}{\sqrt{2}G_F}. \quad (\text{A.4})$$

The numerical input values we use in our analysis are

$$\{m_W, m_Z, m_h, m_t\} = \{80.379, 91.1876, 125, 172.5\} \text{ GeV}, \quad G_F = 1.1663787 \times 10^{-5} \text{ GeV}^{-2}. \quad (\text{A.5})$$

The above relations undergo modifications when working beyond the tree-level approximation and will depend on the renormalization scheme used. We identify the physical input masses as the pole masses of the theory, *i.e.* the propagator poles of the two-point functions of the corresponding particles. According to the renormalization prescription (RP) used to define the counterterms of the theory, the poles will appear at different values of masses  $m_i^{(\text{RP})}$ , *i.e.* from

$$\Delta_i(p^2) = \frac{i}{p^2 - \left(m_i^{(\text{RP})}\right)^2 + \Sigma_i^{(\text{RP})}(p^2)} \quad (\text{A.6})$$

we get

$$\left(m_i^{(\text{RP})}\right)^2 = m_{i,\text{pole}}^2 + \Sigma_i^{(\text{RP})}(p^2 = m_{i,\text{pole}}^2) \quad (\text{A.7})$$

and identify  $m_{i,\text{pole}}$  with the physical input masses  $m_i$ . The self-energies consist of two parts

$$\Sigma_i^{(\text{RP})}(p^2) = \Sigma_{i,\text{proper}}^{(\text{RP})}(p^2) + \Sigma_{i,\text{tad}}^{(\text{RP})}(p^2), \quad (\text{A.8})$$

where  $\Sigma_{i,\text{proper}}^{(\text{RP})}$  are the (real parts of the) “proper” 1PI-irreducible self-energy contributions, and  $\Sigma_{i,\text{tad}}^{(\text{RP})}$  are the tadpole contributions. The (non)-appearance of the latter is dictated by the choice of the tadpole scheme. Now, in order to define the correct values of Lagrangian parameters at a given loop order according to some renormalization prescription RP, we simply replace the masses in (A.3) by the values which follow from (A.7) and adjust the VEV according to the scheme of choice.

We study two different RP-options, namely the  $\overline{\text{MS}}$ -scheme and the “on-shell like”  $\widetilde{\text{OS}}$ -scheme as originally mentioned in [156] and as used *e.g.* in the phase transition tool

BSMPT [157] and further explained in [25]. Other appearances of this scheme are *e.g.* in [62] (called, somewhat confusingly,  $\overline{\text{MS}}$ -scheme there), or in a varied form in [158].

### $\overline{\text{MS}}$ scheme

In the  $\overline{\text{MS}}$ -scheme, we have

$$\left(m_i^{(\overline{\text{MS}})}\right)^2(\mu) = m_i^2 + \Sigma_{i,\text{proper}}^{(\overline{\text{MS}})}(m_i^2, \mu) + \Sigma_{i,\text{tad}}^{(\overline{\text{MS}})}(m_i^2, \mu), \quad (\text{A.9})$$

where  $\mu$  is the renormalization scale. Note that the tadpole contributions are also renormalized in the  $\overline{\text{MS}}$  scheme here, so their finite remainders enter in our calculation. Explicitly, the  $\overline{\text{MS}}$  one-loop relations for (A.3) read

$$g^2 = \frac{4}{v_h^2} \left[ m_W^2 \left( 1 - \frac{\delta v_h^2}{v_h^2} \right) + \Sigma_W^{(\overline{\text{MS}})}(m_W^2) \right], \quad (\text{A.10a})$$

$$g'^2 = \frac{4}{v_h^2} \left[ (m_Z^2 - m_W^2) \left( 1 - \frac{\delta v_h^2}{v_h^2} \right) + \Sigma_Z^{(\overline{\text{MS}})}(m_Z^2) - \Sigma_W^{(\overline{\text{MS}})}(m_W^2) \right], \quad (\text{A.10b})$$

$$y_t^2 = \frac{2m_t}{v_h^2} \left[ m_t \left( 1 - \frac{\delta v_h^2}{v_h^2} \right) + 2\Sigma_t^{(\overline{\text{MS}})}(m_t) \right], \quad (\text{A.10c})$$

$$\mu_h^2 = -\frac{1}{2} \left[ m_h^2 + \Sigma_\phi^{(\overline{\text{MS}})}(m_h^2) \right], \quad (\text{A.10d})$$

$$\lambda_h = \frac{1}{2v_h^2} \left[ m_h^2 \left( 1 - \frac{\delta v_h^2}{v_h^2} \right) + \Sigma_\phi^{(\overline{\text{MS}})}(m_h^2) \right], \quad (\text{A.10e})$$

$$\mu_s^2 = 2 \left( m_s^2 + \Sigma_s^{(\overline{\text{MS}})}(m_s^2) \right) - \frac{v_h^2 \lambda_{hs}}{2} \left( 1 + \frac{\delta v_h^2}{v_h^2} \right), \quad (\text{A.10f})$$

in which  $\Sigma_W$  and  $\Sigma_Z$  are the transverse parts of the vector boson self-energies. For the top self-energy, we use

$$\Sigma_t(m_t) = \Sigma_s(m_t) + \Sigma_v(m_t), \quad (\text{A.11})$$

following the decomposition

$$\Sigma_f(p) = m_f \Sigma_s(p^2) + \not{p} \Sigma_v(p^2) + \not{p} \gamma_5 \Sigma_a(p^2). \quad (\text{A.12})$$

Concerning the VEV, we choose to work in the so-called  $(G_F, m_W, m_Z)$ -scheme. We write the radiative VEV shift as<sup>25</sup>

$$\frac{\delta v^2}{v^2} = \frac{\Sigma_W^{(\overline{\text{MS}})}(m_W^2)}{m_W^2} - \frac{\delta g^2}{g^2}, \quad (\text{A.13})$$

which follows from the relation  $v = 2m_W/g$ . The gauge coupling can, in turn, be expressed as

$$g^2 = \frac{8m_W^2 G_F}{\sqrt{2}} \quad (\text{A.14})$$

---

<sup>25</sup>Inserting this into (A.10) yields the results presented in [101].

and be experimentally accessed by measuring the Fermi coupling  $G_F$  in muon decay. One-loop corrections to muon decay in the  $\overline{\text{MS}}$ -scheme yield

$$\frac{\delta g^2}{g^2} = \frac{\Sigma_W(m_W^2) - \Sigma_W(0)}{m_W^2} - \frac{g^2}{16\pi^2} \left[ 4 \ln \frac{\mu^2}{m_W^2} + \left( \frac{7}{2} \frac{m_Z^2}{m_Z^2 - m_W^2} - 2 \right) \ln \frac{m_W^2}{m_Z^2} + 6 \right]. \quad (\text{A.15})$$

Note that the expressions in Eq. (A.10) are renormalization scale dependent. This dependence is fully governed by the  $\beta$ -functions of the respective couplings, except for Eq. (A.10f). The reason is that we do not make use of a relation of  $\lambda_{hs}$  to a physical observable, as we do for the other parameters. Thence,  $\lambda_{hs}$  is directly used as an input parameter and does not have a one-loop relation to the other parameters of the theory, so its running is not included in Eq. (A.10f). Apart from that, we explicitly checked that the scale dependence in Eq. (A.10) exactly reproduces the running as expected from the known  $\beta$ -functions of the theory. We list those in Section A.2.

### OS-like scheme

In the OS-like scheme (denoted  $\widetilde{\text{OS}}$  in what follows)—after the  $\overline{\text{MS}}$ -renormalization of  $V_1^{T=0}$ —one uses renormalization conditions on the effective potential in order to fix a *finite* counterterm contribution to the potential,  $V_{\text{CT}}$ , such that the minima and scalar masses of the potential do not get shifted away from their tree-level values, *viz.*

$$\left. \frac{\partial}{\partial \phi_i} (V_1^{T=0} + V_{\text{CT}}) \right|_{\phi_i = \langle \phi_i \rangle} = 0, \quad (\text{A.16a})$$

$$\left. \frac{\partial^2}{\partial \phi_i \partial \phi_j} (V_1^{T=0} + V_{\text{CT}}) \right|_{\phi_i = \langle \phi_i \rangle} = 0. \quad (\text{A.16b})$$

This can be useful for simplifying the scanning procedure over large ranges of input values for masses [157]. Note, though, that not all field combinations in (A.16) yield independent or non-trivial equations, so only a subset of fields will contribute here. The relevant ones are the tadpole equation for the field  $\phi$  (because the vev for this component is non-zero) and the mass equations for  $\phi$  and  $s$ . All mixed derivatives of  $\phi$  and  $s$  vanish, and the equations involving derivatives with respect to the Goldstone fields are not independent from the rest, which can be seen by virtue of the corresponding Ward identities, *e.g.* in [159]. Lastly, the tadpole equation for the scalar field  $s$  is fulfilled trivially in the parameter setup we study, where  $v_s = 0$  and does not receive radiative corrections.

As an aside, we note that derivatives of the effective potential in the Landau gauge must be handled with care, as the presence of massless Goldstone boson degrees of freedom can lead to infrared divergences that require proper treatment [160, 161].

The counterterm potential for the cxSM reads

$$V_{\text{CT}} = \delta \mu_h^2 \Phi^\dagger \Phi + \delta \lambda_h (\Phi^\dagger \Phi)^2 + \frac{1}{2} \delta \mu_s^2 |S|^2. \quad (\text{A.17})$$

We only need to adjust the three counterterms in (A.17) in order to keep  $m_h$ ,  $m_S$  and  $v_h$  at their tree-level values. This is why no other counterterms are taken into account explicitly.

From (A.16) we then get

$$\delta\mu_s^2 = -2 \frac{\partial^2 V_1^{T=0}}{\partial\phi_s^2} \Big|_{\phi_h=\phi_s=0}, \quad (\text{A.18a})$$

$$\delta\mu_h^2 = \left( \frac{\partial^2 V_1^{T=0}}{\partial\phi_h^2} - \frac{3}{v} \frac{\partial V_1^{T=0}}{\partial\phi_h} \right) \Big|_{\phi_h=\phi_s=0}, \quad (\text{A.18b})$$

$$\delta\lambda_h = -\frac{2}{v^3} \left( v \frac{\partial^2 V_1^{T=0}}{\partial\phi_h^2} - \frac{\partial V_1^{T=0}}{\partial\phi_h} \right) \Big|_{\phi_h=\phi_s=0}. \quad (\text{A.18c})$$

Knowing that field derivatives of the effective potential correspond to 1PI  $n$ -point functions at zero momentum, we can identify

$$\frac{\partial^2 V_1^{T=0}}{\partial\phi_s^2} \Big|_{\phi_h=v,\phi_s=0} = \Sigma_{\phi_s,\text{proper}}(0), \quad (\text{A.19a})$$

$$\frac{\partial^2 V_1^{T=0}}{\partial\phi_h^2} \Big|_{\phi_h=v,\phi_s=0} = \Sigma_{\phi_h,\text{proper}}(0), \quad (\text{A.19b})$$

$$\frac{\partial V_1^{T=0}}{\partial\phi_h} \Big|_{\phi_h=v,\phi_s=0} = T_{\phi_h}, \quad (\text{A.19c})$$

where  $T_{\phi_h}$  are the tadpole diagrams of  $\phi_h$ . Moreover, the trilinear Higgs coupling in this model times the zero-momentum Higgs propagator is

$$g_{\phi_h^3} \times \Delta_{\phi_h}(p^2=0) = -\frac{3}{v}, \quad (\text{A.20})$$

and we can write

$$-\frac{3}{v} \frac{\partial V_1^{T=0}}{\partial\phi_h} = \Sigma_{\phi_h,\text{tad}}^{(\overline{\text{MS}})}(0). \quad (\text{A.21})$$

Using this, (A.18) can be written as

$$\delta\mu_s^2 = -2\Sigma_S^{(\overline{\text{MS}})}(0), \quad (\text{A.22a})$$

$$\delta\mu_h^2 = \Sigma_{\phi,\text{proper}}^{(\overline{\text{MS}})}(0) + \Sigma_{\phi,\text{tad}}^{(\overline{\text{MS}})}(0), \quad (\text{A.22b})$$

$$\delta\lambda_h = -\frac{2}{v^2} \left( \Sigma_{\phi,\text{proper}}(0) + \frac{1}{3}\Sigma_{\phi,\text{tad}}(0) \right). \quad (\text{A.22c})$$

This might seem counterintuitive because, despite canceling the one-loop tadpoles in (A.16a) via  $V_{\text{CT}}$ , tadpole contributions still appear explicitly in (A.22b).

At this point, we are able to compare the two different renormalization prescriptions, *i.e.* we compare (A.10) with (A.22). For  $\mu_h^2$  we find

$$(\mu_h^2)^{(\overline{\text{MS}})} - (\mu_h^2)^{(\widetilde{\text{OS}})} = \Sigma_{\phi}^{(\overline{\text{MS}})}(m_h^2) - \Sigma_{\phi}^{(\overline{\text{MS}})}(0), \quad (\text{A.23})$$

so the two prescriptions merely differ in the momentum of the self-energies. Notice, though, that the differences for  $\lambda_h$  can not be expressed in such a simple manner. Notably, the

corrections in the  $\widetilde{\text{OS}}$ -scheme are gauge-dependent<sup>26</sup> despite the inclusion of tadpole contributions, because the self-energies can only be gauge-independent at the poles. Another major difference is that in the  $\overline{\text{MS}}$ -scheme also the gauge and Yukawa couplings receive radiative shifts from their relations to the physical input quantities, while in the  $\widetilde{\text{OS}}$ -scheme only  $\mu_s^2$ ,  $\mu_h^2$  and  $\lambda_h$  do. Lastly, both schemes introduce a renormalization scale dependence. However, in the analysis where the  $\widetilde{\text{OS}}$ -scheme is implemented, the renormalization scale is fixed to  $v_{\text{EW}}$  and is not run to the thermal scale.

## A.2 $\beta$ -functions for the cxSM

Here, we list the one-loop  $\beta$ -functions used in our analysis. We used the internal `DRalgo` [70] functions to derive them and to cross-check against our one-loop results. In our analysis, we use  $n_g = 3$  for the number of fermion generations and keep all fermions massless, except for the top-quark. Moreover, we do not include the anomalous dimensions of the fields here.<sup>27</sup> The  $\beta$ -functions read

$$\beta_{g^2} = \frac{1}{16\pi^2} \left[ -\frac{19g^4}{3} \right], \quad (\text{A.24a})$$

$$\beta_{g'^2} = \frac{1}{16\pi^2} \left[ \frac{41g'^4}{3} \right], \quad (\text{A.24b})$$

$$\beta_{y_t^2} = \frac{1}{16\pi^2} \left[ \frac{9y_t^4}{2} - y_t^2 \left( \frac{9g^2}{4} + \frac{17g'^2}{12} + 8g_S^2 \right) \right], \quad (\text{A.24c})$$

$$\beta_{\mu_h^2} = \frac{1}{16\pi^2} \left[ \frac{3}{2}\mu_h^2 (8\lambda_h + 4y_t^2 - 3g^2 - g'^2) + \frac{1}{2}\lambda_{hs}\mu_s^2 \right], \quad (\text{A.24d})$$

$$\beta_{\lambda_h} = \frac{1}{16\pi^2} \left[ \frac{9g^4}{8} + \frac{3g^2g'^2}{4} + \frac{3g'^4}{4} - 6y_t^4 + \lambda_h (12y_t^2 - 9g^2 - 3g'^2) + 24\lambda_h^2 + \frac{\lambda_{hs}^2}{4} \right], \quad (\text{A.24e})$$

$$\beta_{\mu_s^2} = \frac{1}{16\pi^2} [2\lambda_{hs}\mu_h^2 + 4\lambda_s\mu_s^2], \quad (\text{A.24f})$$

$$\beta_{\lambda_s} = \frac{1}{16\pi^2} [5\lambda_s + 2\lambda_{hs}], \quad (\text{A.24g})$$

$$\beta_{\lambda_{hs}} = \frac{1}{16\pi^2} \left[ \lambda_{hs} \left( 2\lambda_s - \frac{9}{2}g^2 - \frac{3}{2}g'^2 + 6y_t^2 + 2\lambda_{hs} + 12\lambda_h \right) \right]. \quad (\text{A.24h})$$

The one-loop beta functions are gauge-independent; however, they become gauge-dependent at two loops. The gauge fixing parameters also run, starting from one loop. For instance, the two-loop  $\beta$ -functions for the SM in a generalized gauge fixing are available in [89], where they have been derived from the effective potential.

<sup>26</sup>The gauge dependence of Lagrange parameters in the  $\widetilde{\text{OS}}$ -scheme propagates to the gauge dependence of the predictions for physical observables, even for the case where the  $\hbar$ -expansion of the effective potential is applied.

<sup>27</sup>The  $\beta$ -functions listed here correspond at one-loop order to  $(-2\varepsilon)$  times the UV-pole, *e.g.* for the bilinear Higgs term, where the renormalization transformation reads  $\mu_h^2\Phi^\dagger\Phi \rightarrow Z_\Phi Z_{\mu^2}\mu_h^2\Phi^\dagger\Phi$ , with  $Z_\Phi$  being the field renormalization constant.

## B Mass eigenstates in $R_\xi$ and Fermi gauges

In this appendix, we list the tree-level mass eigenvalues, depending on the background fields ( $\phi_h$  and  $\phi_s$ ), of the scalars and vectors in the cxSM in various gauges, defined in Section 3.1.

The singlet field is not directly coupled to the gauge sector, hence its mass eigenstates, together with the physical Higgs degree of freedom, are not affected by the gauge-fixing conditions and stay as in Eqs. (2.9) and (2.10). Using Eq. (4.5) as the gauge-fixing condition, we obtain the gauge-dependent mass eigenvalues of vectors, Goldstone bosons, and ghosts. The physical vector degrees of freedom have mass eigenvalues:

$$M_W^2 = \frac{g^2 \phi_h^2}{4}, \quad (\text{B.1})$$

$$M_Z^2 = \frac{(g^2 + g'^2) \phi_h^2}{4}. \quad (\text{B.2})$$

On the other hand, the unphysical degrees of freedom of the vector bosons mix with Goldstone modes and read (for compactness, we introduce the subscript  $V = \{W, Z\}$ ):

$$M_{V,\pm}^2 = \frac{1}{2} \left( M_G^2 + 2M_V^2 \frac{\phi^{GF}}{\phi_h} \sqrt{\xi_1^V \xi_2^V} \pm M_G \sqrt{M_G^2 - 4M_V^2 \left( \xi_1^V - \frac{\phi^{GF}}{\phi_h} \sqrt{\xi_1^V \xi_2^V} \right)} \right), \quad (\text{B.3})$$

$$M_{cV}^2 = M_V^2 \frac{\phi^{GF}}{\phi_h} \sqrt{\xi_1^V \xi_2^V}, \quad (\text{B.4})$$

where  $M_G^2 = \mu_h^2 + \lambda_h \phi_h^2 + \frac{\lambda_{hs} s^2}{4}$ , and  $M_{cV}^2$  is the ghost mass eigenvalue. Then, for the gauge-fixing choices discussed in Section 3.1, we have

1. **Fermi gauge** ( $\xi_1^V = \xi^V$ ,  $\xi_2^V = 0$ ):

$$M_{V,\pm}^2 = \frac{1}{2} \left( M_G^2 \pm M_G \sqrt{M_G^2 - 4M_V^2 \xi_1^V} \right), \quad M_{cV}^2 = 0 \quad (\text{B.5})$$

2. **Background  $R_\xi$ -gauge** ( $\xi_1^V = \xi_2^V = \xi^V$ ,  $\phi^{GF} = \phi_h$ ):

$$M_{V,+}^2 = M_G^2 + \xi^V M_V^2, \quad M_{V,-}^2 = \xi^V M_V^2, \quad M_{cV}^2 = \xi^V M_V^2 \quad (\text{B.6})$$

3. **standard  $R_\xi$ -gauge** ( $\xi_1^V = \xi_2^V = \xi^V$ ,  $\phi^{GF} = v_h$ ):

$$M_{V,\pm}^2 = \left( M_G^2 + 2M_V^2 \xi^V \frac{v_h}{\phi_h} \pm M_G \sqrt{M_G^2 - 4M_V^2 \xi^V \frac{\phi_h - v_h}{\phi_h}} \right), \quad M_{cV}^2 = \xi^V M_V^2 \frac{v_h}{\phi_h} \quad (\text{B.7})$$

4. **Landau gauge** ( $\xi_1^V = \xi_2^V = 0$ ):

$$M_{V,+}^2 = M_G^2, \quad M_{V,-}^2 = 0, \quad M_{cV}^2 = 0. \quad (\text{B.8})$$

In general, the relations between gauge-fixing parameters are not preserved by the RGE evolution, except for the fixed points [94, 109].

## References

- [1] V.A. Kuzmin, V.A. Rubakov and M.E. Shaposhnikov, *On the Anomalous Electroweak Baryon Number Nonconservation in the Early Universe*, *Phys. Lett. B* **155** (1985) 36.
- [2] LIGO SCIENTIFIC, VIRGO collaboration, *Observation of Gravitational Waves from a Binary Black Hole Merger*, *Phys. Rev. Lett.* **116** (2016) 061102 [[1602.03837](#)].
- [3] ET collaboration, *Science Case for the Einstein Telescope*, *JCAP* **03** (2020) 050 [[1912.02622](#)].
- [4] LISA COSMOLOGY WORKING GROUP collaboration, *Cosmology with the Laser Interferometer Space Antenna*, *Living Rev. Rel.* **26** (2023) 5 [[2204.05434](#)].
- [5] I. Affleck, *Quantum Statistical Metastability*, *Phys. Rev. Lett.* **46** (1981) 388.
- [6] Y.B. Zeldovich, I.Y. Kobzarev and L.B. Okun, *Cosmological Consequences of the Spontaneous Breakdown of Discrete Symmetry*, *Zh. Eksp. Teor. Fiz.* **67** (1974) 3.
- [7] T.W.B. Kibble, *Topology of Cosmic Domains and Strings*, *J. Phys. A* **9** (1976) 1387.
- [8] S.W. Hawking, I.G. Moss and J.M. Stewart, *Bubble Collisions in the Very Early Universe*, *Phys. Rev. D* **26** (1982) 2681.
- [9] H. Kodama, M. Sasaki and K. Sato, *Abundance of Primordial Holes Produced by Cosmological First Order Phase Transition*, *Prog. Theor. Phys.* **68** (1982) 1979.
- [10] M. Lewicki and V. Vaskonen, *On bubble collisions in strongly supercooled phase transitions*, *Phys. Dark Univ.* **30** (2020) 100672 [[1912.00997](#)].
- [11] J. Liu, L. Bian, R.-G. Cai, Z.-K. Guo and S.-J. Wang, *Primordial black hole production during first-order phase transitions*, *Phys. Rev. D* **105** (2022) L021303 [[2106.05637](#)].
- [12] I. Baldes and M.O. Olea-Romacho, *Primordial black holes as dark matter: interferometric tests of phase transition origin*, *JHEP* **01** (2024) 133 [[2307.11639](#)].
- [13] T. Vachaspati, *Magnetic fields from cosmological phase transitions*, *Phys. Lett. B* **265** (1991) 258.
- [14] G. Sigl, A.V. Olinto and K. Jedamzik, *Primordial magnetic fields from cosmological first order phase transitions*, *Phys. Rev. D* **55** (1997) 4582 [[astro-ph/9610201](#)].
- [15] M.O. Olea-Romacho, *Primordial magnetogenesis in the two-Higgs-doublet model*, *Phys. Rev. D* **109** (2024) 015023 [[2310.19948](#)].
- [16] A. Azatov, M. Vanvlasselaer and W. Yin, *Dark Matter production from relativistic bubble walls*, *JHEP* **03** (2021) 288 [[2101.05721](#)].
- [17] I. Baldes, M. Dichtl, Y. Gouttenoire and F. Sala, *Ultrahigh-Energy Particle Collisions and Heavy Dark Matter at Phase Transitions*, *Phys. Rev. Lett.* **134** (2025) 061001 [[2306.15555](#)].
- [18] ATLAS collaboration, *Observation of a new particle in the search for the Standard Model Higgs boson with the ATLAS detector at the LHC*, *Phys. Lett. B* **716** (2012) 1 [[1207.7214](#)].
- [19] CMS collaboration, *Observation of a New Boson at a Mass of 125 GeV with the CMS Experiment at the LHC*, *Phys. Lett. B* **716** (2012) 30 [[1207.7235](#)].
- [20] K. Kajantie, M. Laine, K. Rummukainen and M.E. Shaposhnikov, *Is there a hot electroweak phase transition at  $m_H \gtrsim m_W$ ?*, *Phys. Rev. Lett.* **77** (1996) 2887 [[hep-ph/9605288](#)].

- [21] S. Profumo, M.J. Ramsey-Musolf and G. Shaughnessy, *Singlet Higgs phenomenology and the electroweak phase transition*, *JHEP* **08** (2007) 010 [[0705.2425](#)].
- [22] J.R. Espinosa, T. Konstandin and F. Riva, *Strong Electroweak Phase Transitions in the Standard Model with a Singlet*, *Nucl. Phys. B* **854** (2012) 592 [[1107.5441](#)].
- [23] J.M. Cline and K. Kainulainen, *Electroweak baryogenesis and dark matter from a singlet Higgs*, *JCAP* **01** (2013) 012 [[1210.4196](#)].
- [24] G.C. Dorsch, S.J. Huber and J.M. No, *A strong electroweak phase transition in the 2HDM after LHC8*, *JHEP* **10** (2013) 029 [[1305.6610](#)].
- [25] P. Basler, M. Krause, M. Muhlleitner, J. Wittbrodt and A. Wlotzka, *Strong First Order Electroweak Phase Transition in the CP-Conserving 2HDM Revisited*, *JHEP* **02** (2017) 121 [[1612.04086](#)].
- [26] D. Gonçalves, A. Kaladharan and Y. Wu, *Electroweak phase transition in the 2HDM: Collider and gravitational wave complementarity*, *Phys. Rev. D* **105** (2022) 095041 [[2108.05356](#)].
- [27] T. Biekötter, S. Heinemeyer, J.M. No, M.O. Olea and G. Weiglein, *Fate of electroweak symmetry in the early Universe: Non-restoration and trapped vacua in the N2HDM*, *JCAP* **06** (2021) 018 [[2103.12707](#)].
- [28] T. Biekötter, S. Heinemeyer, J.M. No, M.O. Olea-Romacho and G. Weiglein, *The trap in the early Universe: impact on the interplay between gravitational waves and LHC physics in the 2HDM*, *JCAP* **03** (2023) 031 [[2208.14466](#)].
- [29] T. Biekötter, S. Heinemeyer, J.M. No, K. Radchenko, M.O.O. Romacho and G. Weiglein, *First shot of the smoking gun: probing the electroweak phase transition in the 2HDM with novel searches for  $A \rightarrow ZH$  in  $\ell^+\ell^-t\bar{t}$  and  $\nu b\bar{b}$  final states*, *JHEP* **01** (2024) 107 [[2309.17431](#)].
- [30] H.H. Patel and M.J. Ramsey-Musolf, *Stepping Into Electroweak Symmetry Breaking: Phase Transitions and Higgs Phenomenology*, *Phys. Rev. D* **88** (2013) 035013 [[1212.5652](#)].
- [31] L. Niemi, H.H. Patel, M.J. Ramsey-Musolf, T.V.I. Tenkanen and D.J. Weir, *Electroweak phase transition in the real triplet extension of the SM: Dimensional reduction*, *Phys. Rev. D* **100** (2019) 035002 [[1802.10500](#)].
- [32] C. Grojean, G. Servant and J.D. Wells, *First-order electroweak phase transition in the standard model with a low cutoff*, *Phys. Rev. D* **71** (2005) 036001 [[hep-ph/0407019](#)].
- [33] J.E. Camargo-Molina, R. Enberg and J. Löfgren, *A new perspective on the electroweak phase transition in the Standard Model Effective Field Theory*, *JHEP* **10** (2021) 127 [[2103.14022](#)].
- [34] E. Camargo-Molina, R. Enberg and J. Löfgren, *A catalog of first-order electroweak phase transitions in the Standard Model Effective Field Theory*, *JHEP* **08** (2025) 113 [[2410.23210](#)].
- [35] G. Nardini, M. Quiros and A. Wulzer, *A Confining Strong First-Order Electroweak Phase Transition*, *JHEP* **09** (2007) 077 [[0706.3388](#)].
- [36] T. Konstandin and G. Servant, *Cosmological Consequences of Nearly Conformal Dynamics at the TeV scale*, *JCAP* **12** (2011) 009 [[1104.4791](#)].
- [37] P. Creminelli, A. Nicolis and R. Rattazzi, *Holography and the electroweak phase transition*, *JHEP* **03** (2002) 051 [[hep-th/0107141](#)].

- [38] M. Quiros, *Finite temperature field theory and phase transitions*, in *ICTP Summer School in High-Energy Physics and Cosmology*, pp. 187–259, 1, 1999 [[hep-ph/9901312](#)].
- [39] P.B. Arnold and O. Espinosa, *The Effective potential and first order phase transitions: Beyond leading-order*, *Phys. Rev. D* **47** (1993) 3546 [[hep-ph/9212235](#)].
- [40] R.R. Parwani, *Resummation in a hot scalar field theory*, *Phys. Rev. D* **45** (1992) 4695 [[hep-ph/9204216](#)].
- [41] C.G. Boyd, D.E. Brahm and S.D.H. Hsu, *Resummation methods at finite temperature: The Tadpole way*, *Phys. Rev. D* **48** (1993) 4963 [[hep-ph/9304254](#)].
- [42] D. Curtin, P. Meade and H. Ramani, *Thermal Resummation and Phase Transitions*, *Eur. Phys. J. C* **78** (2018) 787 [[1612.00466](#)].
- [43] H. Bahl, M. Carena, A. Ireland and C.E.M. Wagner, *Improved thermal resummation for multi-field potentials*, *JHEP* **09** (2024) 153 [[2404.12439](#)].
- [44] P. Bittar, S. Roy and C.E.M. Wagner, *Self Consistent Thermal Resummation: A Case Study of the Phase Transition in 2HDM*, [2504.02024](#).
- [45] P. Navarrete, R. Paatelainen, K. Seppänen and T.V.I. Tenkanen, *Cosmological phase transitions without high-temperature expansions*, [2507.07014](#).
- [46] L.G. Câmara, M.B. Pinto and R. O. Ramos, *Scale dependence improvement of the quartic scalar field thermal effective potential in the optimized perturbation theory*, [2509.07250](#).
- [47] C.-W. Chiang, M.J. Ramsey-Musolf and E. Senaha, *Standard Model with a Complex Scalar Singlet: Cosmological Implications and Theoretical Considerations*, *Phys. Rev. D* **97** (2018) 015005 [[1707.09960](#)].
- [48] C.-W. Chiang, Y.-T. Li and E. Senaha, *Revisiting electroweak phase transition in the standard model with a real singlet scalar*, *Phys. Lett. B* **789** (2019) 154 [[1808.01098](#)].
- [49] M. Carena, Z. Liu and Y. Wang, *Electroweak phase transition with spontaneous  $Z_2$ -breaking*, *JHEP* **08** (2020) 107 [[1911.10206](#)].
- [50] G.-C. Cho, C. Idegawa and E. Senaha, *Electroweak phase transition in a complex singlet extension of the Standard Model with degenerate scalars*, *Phys. Lett. B* **823** (2021) 136787 [[2105.11830](#)].
- [51] E. Fernández-Martínez, J. López-Pavón, J.M. No, T. Ota and S. Rosauero-Alcaraz,  *$\nu$  Electroweak baryogenesis: the scalar singlet strikes back*, *Eur. Phys. J. C* **83** (2023) 715 [[2210.16279](#)].
- [52] J. Ellis, M. Lewicki, M. Merchand, J.M. No and M. Zych, *The scalar singlet extension of the Standard Model: gravitational waves versus baryogenesis*, *JHEP* **01** (2023) 093 [[2210.16305](#)].
- [53] W. Zhang, Y. Cai, M.J. Ramsey-Musolf and L. Zhang, *Testing complex singlet scalar cosmology at the Large Hadron Collider*, *JHEP* **01** (2024) 051 [[2307.01615](#)].
- [54] J. Braathen, S. Heinemeyer, C.P. Boatella and A. Verduras Schaeidt, *Complementarity of gravitational wave analyses and di-Higgs production in the exploration of the Electroweak Phase Transition dynamics in the  $R\bar{x}SM$* , [2510.12569](#).
- [55] M. Chala, M. Ramos and M. Spannowsky, *Gravitational wave and collider probes of a triplet Higgs sector with a low cutoff*, *Eur. Phys. J. C* **79** (2019) 156 [[1812.01901](#)].

- [56] J.R. Espinosa, *Dominant two loop corrections to the MSSM finite temperature effective potential*, *Nucl. Phys. B* **475** (1996) 273 [[hep-ph/9604320](#)].
- [57] M. Laine and M. Losada, *Two loop dimensional reduction and effective potential without temperature expansions*, *Nucl. Phys. B* **582** (2000) 277 [[hep-ph/0003111](#)].
- [58] K. Funakubo and E. Senaha, *Two-loop effective potential, thermal resummation, and first-order phase transitions: Beyond the high-temperature expansion*, *Phys. Rev. D* **87** (2013) 054003 [[1210.1737](#)].
- [59] A. Ekstedt and J. Löfgren, *A Critical Look at the Electroweak Phase Transition*, *JHEP* **12** (2020) 136 [[2006.12614](#)].
- [60] P. Athron, C. Balazs, A. Fowlie, L. Morris, G. White and Y. Zhang, *How arbitrary are perturbative calculations of the electroweak phase transition?*, *JHEP* **01** (2023) 050 [[2208.01319](#)].
- [61] D. Croon, O. Gould, P. Schicho, T.V.I. Tenkanen and G. White, *Theoretical uncertainties for cosmological first-order phase transitions*, *JHEP* **04** (2021) 055 [[2009.10080](#)].
- [62] M. Lewicki, M. Merchand, L. Sagunski, P. Schicho and D. Schmitt, *Impact of theoretical uncertainties on model parameter reconstruction from GW signals sourced by cosmological phase transitions*, *Phys. Rev. D* **110** (2024) 023538 [[2403.03769](#)].
- [63] O. Gould and P.M. Saffin, *Perturbative gravitational wave predictions for the real-scalar extended Standard Model*, *JHEP* **03** (2025) 105 [[2411.08951](#)].
- [64] P.H. Ginsparg, *First Order and Second Order Phase Transitions in Gauge Theories at Finite Temperature*, *Nucl. Phys. B* **170** (1980) 388.
- [65] T. Appelquist and R.D. Pisarski, *High-Temperature Yang-Mills Theories and Three-Dimensional Quantum Chromodynamics*, *Phys. Rev. D* **23** (1981) 2305.
- [66] L. Niemi, M.J. Ramsey-Musolf, T.V.I. Tenkanen and D.J. Weir, *Thermodynamics of a Two-Step Electroweak Phase Transition*, *Phys. Rev. Lett.* **126** (2021) 171802 [[2005.11332](#)].
- [67] L. Niemi, M.J. Ramsey-Musolf and G. Xia, *Nonperturbative study of the electroweak phase transition in the real scalar singlet extended standard model*, *Phys. Rev. D* **110** (2024) 115016 [[2405.01191](#)].
- [68] M.J. Ramsey-Musolf, T.V.I. Tenkanen and V.Q. Tran, *Refining Gravitational Wave and Collider Physics Dialogue via Singlet Scalar Extension*, [2409.17554](#).
- [69] K. Farakos, K. Kajantie, K. Rummukainen and M.E. Shaposhnikov, *3-D physics and the electroweak phase transition: Perturbation theory*, *Nucl. Phys. B* **425** (1994) 67 [[hep-ph/9404201](#)].
- [70] A. Ekstedt, P. Schicho and T.V.I. Tenkanen, *DRalgo: A package for effective field theory approach for thermal phase transitions*, *Comput. Phys. Commun.* **288** (2023) 108725 [[2205.08815](#)].
- [71] K. Kainulainen, V. Keus, L. Niemi, K. Rummukainen, T.V.I. Tenkanen and V. Vaskonen, *On the validity of perturbative studies of the electroweak phase transition in the Two Higgs Doublet model*, *JHEP* **06** (2019) 075 [[1904.01329](#)].
- [72] L. Niemi and T.V.I. Tenkanen, *Investigating two-loop effects for first-order electroweak phase transitions*, *Phys. Rev. D* **111** (2025) 075034 [[2408.15912](#)].

- [73] H.H. Patel and M.J. Ramsey-Musolf, *Baryon Washout, Electroweak Phase Transition, and Perturbation Theory*, *JHEP* **07** (2011) 029 [[1101.4665](#)].
- [74] A. Ekstedt and J. Löfgren, *On the relationship between gauge dependence and IR divergences in the  $\hbar$ -expansion of the effective potential*, *JHEP* **01** (2019) 226 [[1810.01416](#)].
- [75] A. Ashoorioon and T. Konstandin, *Strong electroweak phase transitions without collider traces*, *JHEP* **07** (2009) 086 [[0904.0353](#)].
- [76] F.F. Freitas, G. Lourenço, A.P. Morais, A. Nunes, J.a. Olívia, R. Pasechnik et al., *Impact of SM parameters and of the vacua of the Higgs potential in gravitational waves detection*, *JCAP* **03** (2022) 046 [[2108.12810](#)].
- [77] P. Schicho, T.V.I. Tenkanen and G. White, *Combining thermal resummation and gauge invariance for electroweak phase transition*, *JHEP* **11** (2022) 047 [[2203.04284](#)].
- [78] A. Denner, *Techniques for calculation of electroweak radiative corrections at the one loop level and results for W physics at LEP-200*, *Fortsch. Phys.* **41** (1993) 307 [[0709.1075](#)].
- [79] V. Barger, P. Langacker, M. McCaskey, M. Ramsey-Musolf and G. Shaughnessy, *Complex Singlet Extension of the Standard Model*, *Phys. Rev. D* **79** (2009) 015018 [[0811.0393](#)].
- [80] T. Biekötter and M. Pierre, *Higgs-boson visible and invisible constraints on hidden sectors*, *Eur. Phys. J. C* **82** (2022) 1026 [[2208.05505](#)].
- [81] G. Arcadi, F. Costa, A. Goudelis and O. Lebedev, *Higgs portal dark matter freeze-in at stronger coupling: observational benchmarks*, *JHEP* **07** (2024) 044 [[2405.03760](#)].
- [82] C. Gross, O. Lebedev and T. Toma, *Cancellation Mechanism for Dark-Matter–Nucleon Interaction*, *Phys. Rev. Lett.* **119** (2017) 191801 [[1708.02253](#)].
- [83] K. Kannike and M. Raidal, *Phase Transitions and Gravitational Wave Tests of Pseudo-Goldstone Dark Matter in the Softly Broken U(1) Scalar Singlet Model*, *Phys. Rev. D* **99** (2019) 115010 [[1901.03333](#)].
- [84] D. Curtin, P. Meade and C.-T. Yu, *Testing Electroweak Baryogenesis with Future Colliders*, *JHEP* **11** (2014) 127 [[1409.0005](#)].
- [85] G. Jona-Lasinio, *Relativistic field theories with symmetry breaking solutions*, *Nuovo Cim.* **34** (1964) 1790.
- [86] S.R. Coleman and E.J. Weinberg, *Radiative Corrections as the Origin of Spontaneous Symmetry Breaking*, *Phys. Rev. D* **7** (1973) 1888.
- [87] R. Jackiw, *Functional evaluation of the effective potential*, *Phys. Rev. D* **9** (1974) 1686.
- [88] S.P. Martin, *Effective potential at three loops*, *Phys. Rev. D* **96** (2017) 096005 [[1709.02397](#)].
- [89] S.P. Martin and H.H. Patel, *Two-loop effective potential for generalized gauge fixing*, *Phys. Rev. D* **98** (2018) 076008 [[1808.07615](#)].
- [90] R. Fukuda and T. Kugo, *Gauge Invariance in the Effective Action and Potential*, *Phys. Rev. D* **13** (1976) 3469.
- [91] N.K. Nielsen, *On the Gauge Dependence of Spontaneous Symmetry Breaking in Gauge Theories*, *Nucl. Phys. B* **101** (1975) 173.
- [92] D. Metaxas and E.J. Weinberg, *Gauge independence of the bubble nucleation rate in theories with radiative symmetry breaking*, *Phys. Rev. D* **53** (1996) 836 [[hep-ph/9507381](#)].

- [93] L.P. Alexander and A. Pilaftsis, *The One-Loop Effective Potential in Non-Linear Gauges*, *J. Phys. G* **36** (2009) 045006 [0809.1580].
- [94] S.P. Martin, *Taming the Goldstone contributions to the effective potential*, *Phys. Rev. D* **90** (2014) 016013 [1406.2355].
- [95] A. Andreassen, W. Frost and M.D. Schwartz, *Consistent Use of Effective Potentials*, *Phys. Rev. D* **91** (2015) 016009 [1408.0287].
- [96] M. Bando, T. Kugo, N. Maekawa and H. Nakano, *Improving the effective potential*, *Phys. Lett. B* **301** (1993) 83 [hep-ph/9210228].
- [97] O. Gould and T.V.I. Tenkanen, *On the perturbative expansion at high temperature and implications for cosmological phase transitions*, *JHEP* **06** (2021) 069 [2104.04399].
- [98] M. Laine, M. Meyer and G. Nardini, *Thermal phase transition with full 2-loop effective potential*, *Nucl. Phys. B* **920** (2017) 565 [1702.07479].
- [99] O. Gould and J. Hirvonen, *Effective field theory approach to thermal bubble nucleation*, *Phys. Rev. D* **104** (2021) 096015 [2108.04377].
- [100] K. Kajantie, M. Laine, K. Rummukainen and M.E. Shaposhnikov, *Generic rules for high temperature dimensional reduction and their application to the standard model*, *Nucl. Phys. B* **458** (1996) 90 [hep-ph/9508379].
- [101] L. Niemi, P. Schicho and T.V.I. Tenkanen, *Singlet-assisted electroweak phase transition at two loops*, *Phys. Rev. D* **103** (2021) 115035 [2103.07467].
- [102] P.M. Schicho, T.V.I. Tenkanen and J. Österman, *Robust approach to thermal resummation: Standard Model meets a singlet*, *JHEP* **06** (2021) 130 [2102.11145].
- [103] O. Gould, *Real scalar phase transitions: a nonperturbative analysis*, *JHEP* **04** (2021) 057 [2101.05528].
- [104] M. Chala and G. Guedes, *The high-temperature limit of the SM(EFT)*, *JHEP* **07** (2025) 085 [2503.20016].
- [105] M. Chala, J.C. Criado, L. Gil and J.L. Miras, *Higher-order-operator corrections to phase-transition parameters in dimensional reduction*, *JHEP* **10** (2024) 025 [2406.02667].
- [106] M. Chala, A. Dashko and G. Guedes, *Running Couplings in High-Temperature Effective Field Theory*, 2510.26878.
- [107] E.J. Weinberg and A.-q. Wu, *Understanding complex perturbative effective potentials*, *Phys. Rev. D* **36** (1987) 2474.
- [108] J.R. Espinosa, M. Garny and T. Konstandin, *Interplay of Infrared Divergences and Gauge-Dependence of the Effective Potential*, *Phys. Rev. D* **94** (2016) 055026 [1607.08432].
- [109] L. Di Luzio and L. Mihaila, *On the gauge dependence of the Standard Model vacuum instability scale*, *JHEP* **06** (2014) 079 [1404.7450].
- [110] P. Meade and H. Ramani, *Unrestored Electroweak Symmetry*, *Phys. Rev. Lett.* **122** (2019) 041802 [1807.07578].
- [111] I. Baldes and G. Servant, *High scale electroweak phase transition: baryogenesis  $\setminus \mathcal{E}$  symmetry non-restoration*, *JHEP* **10** (2018) 053 [1807.08770].
- [112] A. Glioti, R. Rattazzi and L. Vecchi, *Electroweak Baryogenesis above the Electroweak Scale*, *JHEP* **04** (2019) 027 [1811.11740].

- [113] M. Carena, C. Krause, Z. Liu and Y. Wang, *New approach to electroweak symmetry nonrestoration*, *Phys. Rev. D* **104** (2021) 055016 [[2104.00638](#)].
- [114] O. Matsedonskyi, J. Unwin and Q. Wang, *Electroweak symmetry non-restoration from dark matter*, *JHEP* **12** (2021) 167 [[2107.07560](#)].
- [115] S.R. Coleman, *The Fate of the False Vacuum. 1. Semiclassical Theory*, *Phys. Rev. D* **15** (1977) 2929.
- [116] A.D. Linde, *Fate of the False Vacuum at Finite Temperature: Theory and Applications*, *Phys. Lett. B* **100** (1981) 37.
- [117] A. Ekstedt, *Bubble nucleation to all orders*, *JHEP* **08** (2022) 115 [[2201.07331](#)].
- [118] A. Ekstedt, *Higher-order corrections to the bubble-nucleation rate at finite temperature*, *Eur. Phys. J. C* **82** (2022) 173 [[2104.11804](#)].
- [119] A. Ekstedt, O. Gould and J. Hirvonen, *BubbleDet: a Python package to compute functional determinants for bubble nucleation*, *JHEP* **12** (2023) 056 [[2308.15652](#)].
- [120] A.D. Linde, *Decay of the False Vacuum at Finite Temperature*, *Nucl. Phys. B* **216** (1983) 421.
- [121] E.J. Weinberg, *Vacuum decay in theories with symmetry breaking by radiative corrections*, *Phys. Rev. D* **47** (1993) 4614 [[hep-ph/9211314](#)].
- [122] D. Bodeker, W. Buchmuller, Z. Fodor and T. Helbig, *Aspects of the cosmological electroweak phase transition*, *Nucl. Phys. B* **423** (1994) 171 [[hep-ph/9311346](#)].
- [123] A. Surig, *Selfconsistent treatment of bubble nucleation at the electroweak phase transition*, *Phys. Rev. D* **57** (1998) 5049 [[hep-ph/9706259](#)].
- [124] J. Löfgren, M.J. Ramsey-Musolf, P. Schicho and T.V.I. Tenkanen, *Nucleation at Finite Temperature: A Gauge-Invariant Perturbative Framework*, *Phys. Rev. Lett.* **130** (2023) 251801 [[2112.05472](#)].
- [125] J. Hirvonen, J. Löfgren, M.J. Ramsey-Musolf, P. Schicho and T.V.I. Tenkanen, *Computing the gauge-invariant bubble nucleation rate in finite temperature effective field theory*, *JHEP* **07** (2022) 135 [[2112.08912](#)].
- [126] D. Metaxas, *Derivative expansion and gauge independence of the false vacuum decay rate in various gauges*, *Phys. Rev. D* **63** (2001) 085009 [[hep-ph/0011015](#)].
- [127] S.J. Huber and T. Konstandin, *Production of gravitational waves in the nMSSM*, *JCAP* **05** (2008) 017 [[0709.2091](#)].
- [128] A.H. Guth and E.J. Weinberg, *Cosmological Consequences of a First Order Phase Transition in the SU(5) Grand Unified Model*, *Phys. Rev. D* **23** (1981) 876.
- [129] J. Ellis, M. Lewicki and J.M. No, *On the Maximal Strength of a First-Order Electroweak Phase Transition and its Gravitational Wave Signal*, *JCAP* **04** (2019) 003 [[1809.08242](#)].
- [130] P. Athron, C. Balázs, A. Fowlie, L. Morris and L. Wu, *Cosmological phase transitions: From perturbative particle physics to gravitational waves*, *Prog. Part. Nucl. Phys.* **135** (2024) 104094 [[2305.02357](#)].
- [131] G.W. Anderson and L.J. Hall, *The Electroweak phase transition and baryogenesis*, *Phys. Rev. D* **45** (1992) 2685.

- [132] C.L. Wainwright, *CosmoTransitions: Computing Cosmological Phase Transition Temperatures and Bubble Profiles with Multiple Fields*, *Comput. Phys. Commun.* **183** (2012) 2006 [[1109.4189](#)].
- [133] G.D. Moore and T. Prokopec, *How fast can the wall move? A Study of the electroweak phase transition dynamics*, *Phys. Rev. D* **52** (1995) 7182 [[hep-ph/9506475](#)].
- [134] A. Ekstedt, O. Gould, J. Hirvonen, B. Laurent, L. Niemi, P. Schicho et al., *How fast does the WallGo? A package for computing wall velocities in first-order phase transitions*, *JHEP* **04** (2025) 101 [[2411.04970](#)].
- [135] B. Laurent and J.M. Cline, *First principles determination of bubble wall velocity*, *Phys. Rev. D* **106** (2022) 023501 [[2204.13120](#)].
- [136] G.C. Dorsch, S.J. Huber and T. Konstandin, *Bubble wall velocities in the Standard Model and beyond*, *JCAP* **12** (2018) 034 [[1809.04907](#)].
- [137] M. Lewicki, M. Merchand and M. Zych, *Electroweak bubble wall expansion: gravitational waves and baryogenesis in Standard Model-like thermal plasma*, *JHEP* **02** (2022) 017 [[2111.02393](#)].
- [138] T. Krajewski, M. Lewicki and M. Zych, *Bubble-wall velocity in local thermal equilibrium: hydrodynamical simulations vs analytical treatment*, *JHEP* **05** (2024) 011 [[2402.15408](#)].
- [139] C. Branchina, A. Conaci, L. Delle Rose and S. De Curtis, *Electroweak phase transition and bubble wall velocity in local thermal equilibrium*, *Phys. Rev. D* **112** (2025) 095008 [[2504.21213](#)].
- [140] G.C. Dorsch, S.J. Huber, T. Konstandin and J.M. No, *A Second Higgs Doublet in the Early Universe: Baryogenesis and Gravitational Waves*, *JCAP* **05** (2017) 052 [[1611.05874](#)].
- [141] S. Jiang, F.P. Huang and X. Wang, *Bubble wall velocity during electroweak phase transition in the inert doublet model*, *Phys. Rev. D* **107** (2023) 095005 [[2211.13142](#)].
- [142] J. van de Vis, P. Schicho, L. Niemi, B. Laurent, J. Hirvonen and O. Gould, *WallGo investigates: Theoretical uncertainties in the bubble wall velocity*, [2510.27691](#).
- [143] A. Dashko and A. Ekstedt, *Bubble-wall speed with loop corrections*, *JHEP* **03** (2025) 024 [[2411.05075](#)].
- [144] W.-Y. Ai, M. Carosi, B. Garbrecht, C. Tamarit and M. Vanvlasselaer, *Bubble wall dynamics from nonequilibrium quantum field theory*, *JHEP* **08** (2025) 077 [[2504.13725](#)].
- [145] T. Krajewski, M. Lewicki, I. Nałęcz and M. Zych, *Steady-state bubbles beyond local thermal equilibrium*, *JHEP* **06** (2025) 118 [[2411.16580](#)].
- [146] C. Caprini et al., *Science with the space-based interferometer eLISA. II: Gravitational waves from cosmological phase transitions*, *JCAP* **04** (2016) 001 [[1512.06239](#)].
- [147] C. Caprini et al., *Detecting gravitational waves from cosmological phase transitions with LISA: an update*, *JCAP* **03** (2020) 024 [[1910.13125](#)].
- [148] P. Auclair, C. Caprini, D. Cutting, M. Hindmarsh, K. Rummukainen, D.A. Steer et al., *Generation of gravitational waves from freely decaying turbulence*, *JCAP* **09** (2022) 029 [[2205.02588](#)].
- [149] LISA COSMOLOGY WORKING GROUP collaboration, *Gravitational waves from first-order phase transitions in LISA: reconstruction pipeline and physics interpretation*, *JCAP* **10** (2024) 020 [[2403.03723](#)].

- [150] M. Hindmarsh, S.J. Huber, K. Rummukainen and D.J. Weir, *Shape of the acoustic gravitational wave power spectrum from a first order phase transition*, *Phys. Rev. D* **96** (2017) 103520 [[1704.05871](#)].
- [151] H.-K. Guo, K. Sinha, D. Vagie and G. White, *Phase Transitions in an Expanding Universe: Stochastic Gravitational Waves in Standard and Non-Standard Histories*, *JCAP* **01** (2021) 001 [[2007.08537](#)].
- [152] J.R. Espinosa, T. Konstandin, J.M. No and G. Servant, *Energy Budget of Cosmological First-order Phase Transitions*, *JCAP* **06** (2010) 028 [[1004.4187](#)].
- [153] J. Ellis, M. Lewicki and J.M. No, *Gravitational waves from first-order cosmological phase transitions: lifetime of the sound wave source*, *JCAP* **07** (2020) 050 [[2003.07360](#)].
- [154] S. Blasi and A. Mariotti, *Domain Walls Seeding the Electroweak Phase Transition*, *Phys. Rev. Lett.* **129** (2022) 261303 [[2203.16450](#)].
- [155] C. Caprini, D.G. Figueroa, R. Flauger, G. Nardini, M. Peloso, M. Pieroni et al., *Reconstructing the spectral shape of a stochastic gravitational wave background with LISA*, *JCAP* **11** (2019) 017 [[1906.09244](#)].
- [156] E.J. Weinberg, *Radiative corrections as the origin of spontaneous symmetry breaking*, Ph.D. thesis, Harvard U., 1973. [hep-th/0507214](#).
- [157] P. Basler, L. Biermann, M. Mühlleitner, J. Müller, R. Santos and J. Viana, *BSMPT v3 a tool for phase transitions and primordial gravitational waves in extended Higgs sectors*, *Comput. Phys. Commun.* **316** (2025) 109766 [[2404.19037](#)].
- [158] C. Delaunay, C. Grojean and J.D. Wells, *Dynamics of non-renormalizable electroweak symmetry breaking*, *Journal of High Energy Physics* **2008** (2008) 029–029.
- [159] A. Denner, G. Weiglein and S. Dittmaier, *Application of the background field method to the electroweak standard model*, *Nucl. Phys. B* **440** (1995) 95 [[hep-ph/9410338](#)].
- [160] J.M. Cline and P.-A. Lemieux, *Electroweak phase transition in two Higgs doublet models*, *Phys. Rev. D* **55** (1997) 3873 [[hep-ph/9609240](#)].
- [161] J.M. Cline, K. Kainulainen and M. Trott, *Electroweak Baryogenesis in Two Higgs Doublet Models and B meson anomalies*, *JHEP* **11** (2011) 089 [[1107.3559](#)].